Institut für Festkörperelektronik

TECHNISCHE UNIVERSITÄT WIEN

Numerical Aspects of QCL Frequency Comb Modeling

Master's Thesis

submitted by

Roland Strieder, BSc

Matr. Nr. 11778276

as a part of the

Master's program

Microelectronics and Photonics

at the

TU Wien

Institute of Solid State Electronics

under supervision of

Univ.Prof. Dipl.-Ing. Dr.techn. Benedikt Schwarz, BSc

Vienna, May 2024

Statutory Declaration

I declare, that I have authored the present work independently according to the code of conduct, that I have not used other than the declared sources and that I have explicitly marked all material quoted either literally or by content from the used sources. This work was not yet submitted to any examination procedure neither in Austria, nor in any other country.

Erklärung zur Verfassung der Arbeit

Hiermit erkläre ich, dass die vorliegende Arbeit gemäß dem Code of Conduct - Regeln zur Sicherung guter wissenschaftlicher Praxis - ohne unzulässige Hilfe Dritter und ohne Benutzung anderer als der angegebenen Hilfsmittel, angefertigt wurde. Die aus anderen Quellen direkt oder indirekt übernommenen Daten und Konzepte sind unter Angabe der Quelle gekennzeichnet. Die Arbeit wurde bisher weder im In- noch im Ausland in gleicher oder in ähnlicher Form in anderen Prüfungsverfahren vorgelegt.

Wien, 29. 05. 2024 ..... [redacted] ....

Roland Strieder

KURZFASSUNG

Die erste Demonstration eines Quanten Kaskaden Lasers (QCL) efolgte im Jahr 1994 in den „Bell Laboratories“. Seitdem wurden seine außergewöhnlichen Eigenschaften erforscht und zahlreiche Anwendungen entdeckt. Eine der wichtigsten Anwendungsbereiche dieses Halbleiter-Lasers ist die Spektroskopie. Dabei ist es vorteilhaft, dass der Laser eine große Emissions-Bandbreite besitzt damit viele verschiedene Stoffe detektiert werden können. Die Bandbreite eines QCL kann mithilfe zwei verschiedener Methoden vergrößert werden. In der ersten Methode wird das Kaskaden-Design entlang der Wachstumsrichtung verändert. Dies führt zu einer unterschiedlichen Emissionswellenlänge der einzelnen Schichten, was die Bandbreite erhöht. Eine Alternative zu diesem heterogenen QCL bieten nichtlineare Effekte. Um eine merkbare Verbreiterung des Spektrums zu erzielen, sind hohe Intensitäten erforderlich. Diese können durch optische Pulse erreicht werden. Da der QCL im Vergleich zum Interband-Laser eine schnelle „Gain“ Charakteristik besitzt, ist die Erzeugung von Pulsen nicht ohne Weiteres möglich. Eine vielversprechende Methode bieten frequenzmodulierte optische Frequenzkämme, welche mit QCL erzeugt werden können. Der damit einhergehende „Chirp“ kann mit Hilfe eines Kompressors kompensiert werden, was zu sehr kurzen Pulsen führen kann.

Der QCL und die damit erzeugten Frequenz-Kämme wurden bereits von N. Opačak, mithilfe eines numerischen Modells basierend auf den Maxwell-Bloch Gleichungen, untersucht. In dieser Arbeit wird dieses Modell für die Modellierung von heterogenen QCL analysiert und stark erweitert. Um das Verhalten verschiedener Implementierungen bewerten zu können, wurde ein Testmodell bestehend aus einem abstimmbaren Laser und einem Wellenleiter erstellt. Dieser Wellenleiter wurde schrittweise erweitert, damit verschiedene physikalische Effekte, welche in einem QCL auftreten, implementiert und analysiert werden können. Unter anderem wurde die Implementierung der Gruppen-

geschwindigkeits-Dispersion mithilfe einer neu entwickelten Methode stabilisiert. Diese Methode basiert auf der Laplace-transformation der zugrundeliegenden Gleichung und deren Taylor-Annäherung, welche mit Hilfe der Korrespondenzen im Zeitbereich implementiert wurde. Dieses Verfahren kann darüber hinaus für Dispersionseffekte höherer Ordnung und für die gemeinsame Verwendung verschiedener Dispersionseffekte ausgenützt werden. Des Weiteren ist das neu entwickelte Verfahren kompatibel mit der zuvor verwendeten parallelen Berechnungsmethode, welche die Simulationszeit erheblich reduziert. Ein weiteres physikalisches Phänomen sind Verluste im Wellenleiter, welche analytisch mit Hilfe des exponentiellen Integrators implementiert wurden.

Die Verstärkung des Mediums wurde durch die Anwendung der bilinearen Transformation der Polarisationsgleichung in das Programm eingebunden. Diese spiegelt das Verhalten des Mediums im Frequenzbereich genauer wider, als zum Beispiel ein Verfahren erster Ordnung. Die Verstärkungs-Implementierung der „Master Gleichung" für schnelle Verstärkermedien, welche unter anderem von N. Opačak entwickelt wurde, kann hierfür nicht verwendet werden. Diese induziert numerische Verluste in den Bereichen unterhalb und oberhalb der zentralen Frequenz. Dies war unter anderem vorteilhaft im schmalbendigen Modell, da dies das instabile Verhalten der Dispersions-Implementierung kompensiert hat. Die Implementierung der Verstärkung des Mediums kann für die Simulation von heterogenen QCL erweitert werden. Hierfür werden mehrere Polarisationsgleichungen gelöst, welche im Frequenzbereich verschoben sind. Dies spiegelt das unterschiedliche Kaskaden-Design im heterogenen QCL wider.Die unterschiedlichen Lösungen der Polarisationsgleichungen werden anschließend aufsummiert.

Die zweite Methode, welche das Emissions-Spektrum des Devices erhöht, basiert auf nichtlinearen optischen Effekten. Um kurze optische Pulse mithilfe eines QCL und eines Kompressors erzeugen zu können, müssen beide Komponenten aufeinander abgestimmt sein. Um dies zu ermöglichen, wurden verschiedene Parameter analysiert, welche den „Chirp“ des optischen Frequenzkamms beeinflussen. Unter anderem kann der Zustand des Kamms mit Hilfe des Bias, welcher örtlich durch mehrere Sektionen variiert wird, beeinflusst werden. Ein weiterer Parameter bietet das Design der Kavität. Der Einfluss dieser Effekte wurde durch Lösen der „Master Gleichung" für schnelle Verstärkermedien analysiert. Mit diesen beiden Faktoren, zusammen mit der Reflektivität der Facetten, welche das Ausmaß des Einflusses bestimmt, kann der „Chirp" des Frequenzkamms angepasst werden.

ABSTRACT

Quantum cascade lasers (QCLs) are attracting a great deal of interest due to their wide range of applications in science and industry. The QCL represents a compact and integrable source of coherent light in the infrared and the terahertz regime. To expand the bandwidth of the QCL in order to enlarge the number of detectable analytes, the cascade design can be slightly changed along the growth direction, leading to a different emission frequency of the segments. This structure, namely the heterogeneous QCL, has already been shown in various publications. In order to deepen the understanding of these devices and, among other things, to analyze the generation conditions of optical frequency combs with heterogeneous QCLs, the conventional numerical model of a QCL developed by N. Opačak et al. was numerically analyzed and extended in this work.

Starting with the first-order wave-equation, the description was expanded to include losses, group-velocity dispersion effects, and gain. In case of the losses, the exponential integrator was utilized. This method implements the losses analytically, which is in deep contrast to the previously used first-order approximation. The group velocity dispersion (GVD) implementation was stabilized. This is essential since in case of the simulation of heterogeneous QCsL, the polarization elimination, which was utilized in the master equation model developed by N. Opačak et al., can not be applied. If this simplification is used, the gain induces losses above and below the center frequency stabilizing the overall simulation. To overcome the inherent stability problem, a new method was developed which retains the advantage of parallel computing.
This method is based on the Laplace transformation of the governing wave-equation. The implementation becomes stable by conducting a Taylor expansion and including higher-order terms. The presented method can also be used for a stable implementation of higher-order effects, such as third or fourth-order, and enables their stable joint usage.

Instead of using the master equation formalism with its simplified gain implementation, a slightly simplified version of the Maxwell-Bloch equations was implemented. The equation for the upper state population was carried out by a first-order explicit scheme. This scheme cannot be applied to the polarization equation since it induces numerical losses above and below the center frequency. To overcome this numerical problem, the bilinear Z-transformation was applied to the Laplace transformed polarization equation, which eliminates the unwanted losses. The implementation of the gain was expanded towards the simulation of heterogeneous QCL by a multiple usage of the polarization equation. The gain peaks can be readily shifted in the frequency domain to simulate different cascade designs.

Apart from the heterogeneous QCL, the emission-spectrum can be enriched by nonlinear effects. To obtain noticeable broadening effects, pulses with high intensities are required. In case of QCL, the generation of pulses is challenging due to the fast gain properties of the medium. A powerful technique to overcome this limitation is presented by using a QCL emitting a frequency-modulated optical frequency comb and by compensating its chirp by a compressor. To generate short pulses, the compressor must fully compensate for the chirp induced by the QCL. Different shaping methods of the QCL were analyzed to align these two components, and their impact was simulated based on the master equation for fast gain media. Among the parameters, three important shaping mechanisms were found: laser bias, cavity design, and the reflectivity of the facets. The spatially varying laser bias was simulated by using a more section device, and the cavity design was tested by applying a tapered structure to the device. The reflectivity of the facets influences the extend of their influence. All three parameters combined reveal a versatile set of tools to tailor the locking state of the QCL, enabling the generation of ultra-short pulses.

ACKNOWLEDGMENTS

With the completion of my thesis, my time as a master's student comes to an end. During this time, I deepened my knowledge in the field of microelectronics, microsystem technologies, and phonics. I even had the opportunity to spend an Erasmus+ exchange semester in Lund, Sweden, for which I am very grateful. During that time, I discovered some fascinating properties of light which eventually guided me to start my master's thesis in the group of "Optoelectronic Devices". The completion of a thesis requires a lot of effort and commitment. This page is, therefore, devoted to the people who supported me during this period of my life.

First, I would like to thank my supervisor, and head of the research division "Optoelectronic Devices", **Univ.Prof. Dr.techn. Benedikt Schwarz, BSc** for his support and many helpful discussions. I really appreciated his open mind towards students, and his dedication to the field of integrated optics was really inspiring.

I also want to express my gratitude to the **research team of "Optoelectronic Devices"**. The pleasant ambiance and the feeling of being included in the group from the first second have contributed a lot to the value of this period. A special thank is devoted to **Andreas Windischofer**, for many fruitful discussions and for his help with GitHub, and to **Sandro Dal Cin** for the collaboration which led to a submitted manuscript.

Lastly, I would like to thank my **family and friends**, who have always supported me and stood by my side in every situation.

To all the others who have made this time special.
Thank you very much!

CONTENTS

CHAPTER 1

INTRODUCTION

Lasers consisting of semiconductor material are compact, inexpensive, reliable and feature a low power consumption. After the first demonstration of a laser diode on a GaAs platform by R.N. Hall et al. in the 1960s [1], much research has been carried out in this field. Today, the semiconductor laser has established itself as a powerful and useful device that is employed in optical telecommunications [2], material processing applications [3], and in many other fields such as medical applications [4]. The world as we know it would appear entirely different without the invention of the laser diode. First demonstrations of semiconductor lasers were based on conventional p-n diodes, which utilize the radiative recombination of electrons from the conduction-band and holes from the valance band. The required inversion is achieved by driving the diode electrically while the cavity is formed by simply cleaving the device [4]. The diode structure has been revolutionized by the invention of the double heterostructure design, enabling the confinement of light and carriers, leading to more efficient devices [5, p. 826]. For their development in this field, Z. I. Alferov and H. Kroemer were awarded with the Nobel prize in Physics of the year 2000 [6, 7]. The heterostructure device has been further developed by shrinking the size of the heterostructure to the nano-meter scale leading to quantum-confined semiconductor lasers [5, Ch. 18].

With the development of more advanced fabrication techniques, such as molecular beam epitaxy (MBE) [8] or metal-organic vapor phase epitaxy [9], capable of stacking ultra-thin layers of different materials on top of each other, a new type of laser has emerged. First

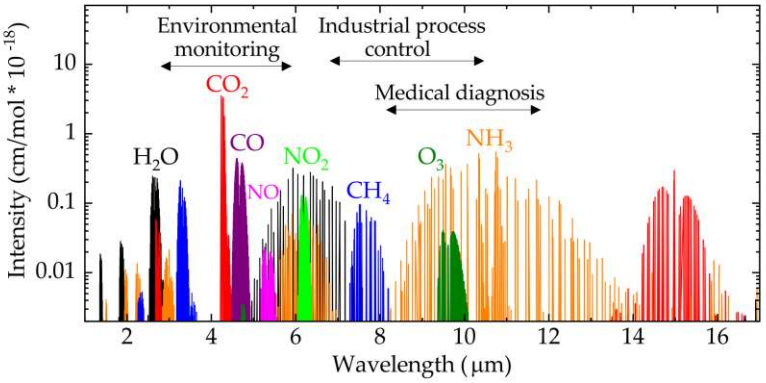

Figure 1.1: *Mid-infrared fingerprint region showing the absorption spectra of carbon dioxide CO_2, water H_2O, carbon monoxide CO, nitric oxide NO, nitrogen dioxide NO_2, methane CH_4, oxygen O_3, and ammonia NH_3. Source: [16, Fig. 1]*

demonstrated in 1994 at Bell Laboratories by J. Faist et al. [10], the *Quantum Cascade Laser (QCL)* was born after its first proposal nearly 20 years back by R.F. Kazarinov and R.A. Suris [11]. In comparison to conventional laser diodes, the QCL is based on transition occurring between states within the conduction-band. The QCL utilizes the impact of the different layer thicknesses on the localization of charges, on their transport, and on their optical processes. A remarkable aspect of this type of laser lies in the possibility of changing the emission wavelength by changing the layer thicknesses. That means, the emission frequency can be tuned over a large bandwidth by engineering the band structure and without changing the material composition. Hence, the device can be fabricated with almost any semiconductor material, whereas the most efficient devices were produced by using a combination of the III-V materials Ga (Gallium), As (Arsenide), In (Indium), Al (Aluminum), Sb (Antimony), and P (Phosphor) with reference to [12]. This epitome of band-structure engineering has become one of the dominant source of coherent light operating in the mid-infrared ($2 \leq \lambda_0 \leq 20\ \mu m$), far-infrared ($20 \leq \lambda_0 \leq 300\ \mu m$), and terahertz range ($100 \leq \lambda_0 \leq 1000\ \mu m$) [5, p. 851 - 854]. This broad spectrum makes the QCL an important tool for many scientific, industrial, and medical applications such as trace gas analysis [13], the sensing of liquids [14], and optical telecommunication [15].

Apart from optical telecommunication, which utilizes spectral transparency windows of the atmosphere, most of the applications of QCLs rely on the presence of absorption lines in the infrared and terahertz range [15]. Figure 1.1 shows these specific lines in the mid-infrared of selected molecules. The detection of these absorption lines resulting from vibrational-rotational transitions is therefore of main interest [5, p. 851 - 854]. One approach to detect these molecular fingerprints with high precision by means of QCL is presented by dual-comb spectroscopy [17]. The basis of this method is the occurrence of optical frequency combs in QCLs. Since their usage in spectroscopy and meteorology is of such high importance, as described in [12], T. Hänsch and J. Hall were awarded with the 2005 Nobel prize in physics [18, 19]. Optical frequency combs generated with QCL

Figure 1.2: *Broadband sources for spectroscopic applications: (a) heterogeneous QCL, (b) short pulses generated by the combination of a QCL emitting an optical frequency comb with an optical compressor, potentially triggering non-linear optical effects to broaden the spectrum. Source for (a): [20]*

present an ideal platform for a fully integrated spectrometer [12].

To analyze the concentration of many different molecules, a broadband source would be of great interest as shown in Figure 1.1. The bandwidth of the QCL can be readily expanded by changing the design of the cascades along the growth direction, leading to a slightly different emission frequency of the layers [20–22]. This concept, namely the heterogeneous QCL, is displayed in Figure 1.2 a. Another technique to broaden the spectrum is presented by the utilization of non-linear optical effects [23]. In order to trigger these non-linear effects, high intensities are required, which are best obtained with pulses. In case of QCL, the generation of pulses is difficult to achieve due to the fast gain dynamics of the medium as described in [24, Ch. 5]. To overcome this fundamental property, J. Hillbrand et al. [25] applied a short modulation section to the QCL, which modulates the intracavity losses. This leads to the formation of pulses. The second method, as shown in Figure 1.2 b, utilizes a QCL emitting an optical frequency comb [24, Ch. 5]. A pulse can be formed by compensating its chirp by an external compressor [26]. Both techniques are capable of forming pulses, however, the theoretical limits of both approaches are different. In the first case, the fundamental limit of storing the energy in the inversion is circumvented by the short modulation section, whereas in the second case, the chirp produced by the QCL can theoretically be fully compensated by the compressor, leading to ultra-short pulses.

Simulation of complex systems has become an indispensable part of research and industry. To deepen the understanding of different parameters influencing the operation of the QCL, much effort has been carried out, especially towards the occurrence of optical frequency combs. An overview of recent modeling and experimental aspects can be found in [24, 27].

The content of this work describes numerical aspects of QCL and optical frequency combs generated with this type of laser. The first chapter sheds light on the working principle of a QCL, introduces its analytical model, and describes the basic principle of the finite difference method utilized for the numerical analysis. Chapter 3 describes the expansion

of an already existing model, developed by N. Opačak [24], towards the simulation of heterogeneous QCLs. This extension comes with many numerical challenges, which are discussed in detail within this part. Finally, chapter 4 is devoted to optical frequency combs. Therein, multiple methods are being discussed and implemented into the narrow-band model to tailor the chirp of the optical frequency comb. This is of utmost importance since the chirp induced by the QCL has to be fully compensated in the second step by the compressor to generate ultra-short pulses. These ultra-short pulses are consequently used to broaden the spectrum by nonlinear optical effects as introduced.

CHAPTER 2

BACKGROUND

Quantum cascade lasers (QCLs) are an important source of coherent light in the infrared and terahertz regime, and they are used in a wide range of applications in science and industry [5, Ch. 18.4]. This chapter comprises a description of the basic principle of this emerging type of laser. The discussion also includes a comparison of the QCLs with conventional semiconductor lasers relying on interband transition. The description of such a complex system is usually based on partial differential equations (PDEs). In most cases, these equations can not be solved analytically. To introduce the mathematical model of a QCL, implemented in chapter 3, the working principle and its analytical description are being described in section 2.1. Finally, section 2.3 describes the basic principle of a versatile method for the numerical solution of differential equations, namely the finite difference method. The basic principle and important properties, including stability, consistency, and convergence, are being discussed in this section.

2.1 Quantum Cascade Lasers

Optical oscillators consist of a region generating gain, and a cavity providing feedback. In case of a conventional semiconductor laser diode, the active region consists of a PN-junction, and the cavity is formed in the simplest case by cleaving the device [28, Ch.7] [4]. The laser diode represents a bipolar device utilizing the radiative recombination of electrons in the conduction-band and holes in the valance-band. This is in deep contrast to the *Quantum cascade lasers* solely utilizing one carrier type [5, Ch. 18.4].

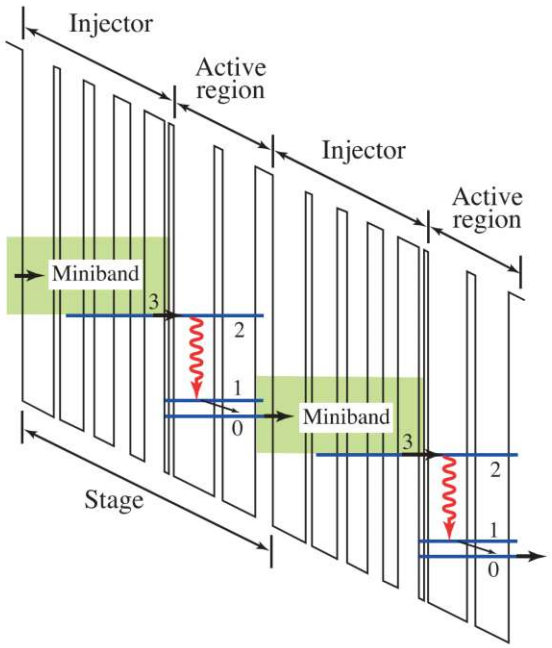

Figure 2.1: *Schematic drawing of a common QCL design utilizing an active region with a quantum-well structure. Source: [5, Fig. 18.8-4 a]*

In general, a cascade of a QCL is composed of two different parts: the injector and the active region as outlined in "Quantum Cascade Lasers, Chapter 7" [29, Ch. 7] and "Fundamentals of Phonics, Chapter 18.4", [5, Ch. 18.4]. The active region consists of at least three states, which can be either quantized or a continuum of states as shown in Figure 2.1a. Electrons are being transferred from the miniband of the injector (state 3) into the second state by resonant tunneling. After this injection process, the electron transfers to state 1 by emitting a photon with the corresponding frequency. After this optical transition, the electron decays by means of scattering to level 0 and is finally flushed into the next injector region again by resonant tunneling. To create an inversion in this system, the first level must be emptied faster than it is filled by the second level. This corresponds to the following relation of the lifetimes

$$\tau_{21} > \tau_1. \tag{2.1}$$

In other words, the lifetime of stage one τ_1 has to be smaller than the transition time of stage two to stage one $\tau_{2,1}$ [29, Ch.7].
While the optical gain is provided by the active region, the injector segment acts as an electron reservoir and consists of a sequence of barriers and quantum-wells: a superlattice. A part of this structure is also doped to prevent the formation of space charge regions. In addition, this section separates the energy of the electrons compared to the band edge which is eventually lost in the active region (Figure 2.1). With a suitable superlattice, it is possible to inject carriers by means of resonant tunneling. In certain active region structures, such as the three quantum-well design, this process is too slow to empty the

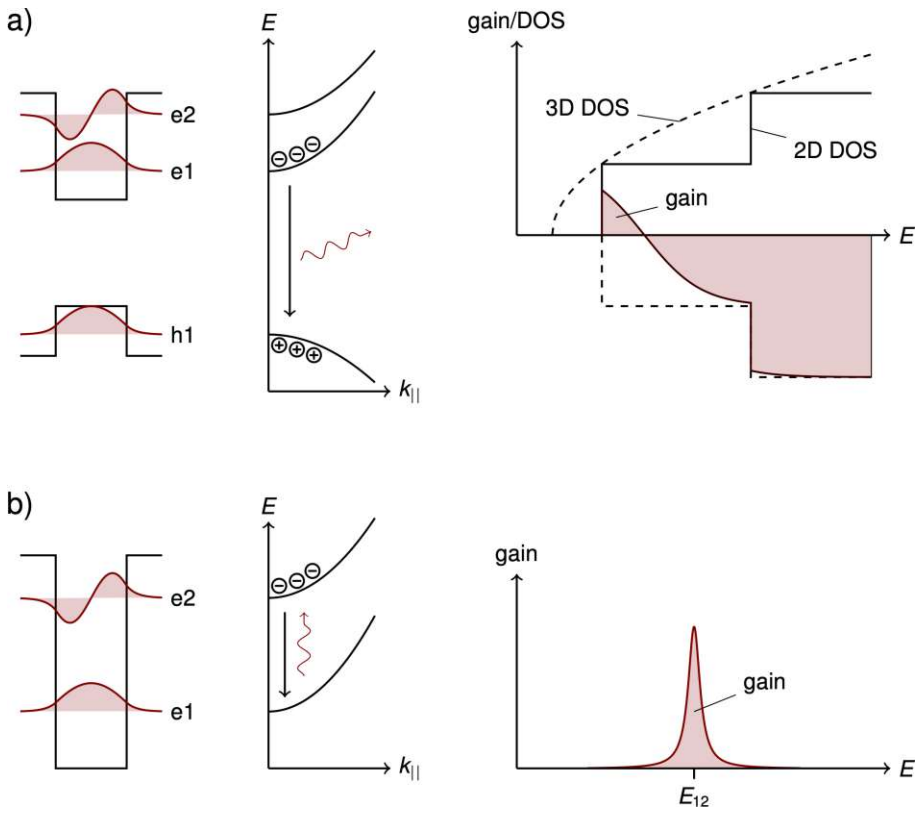

Figure 2.2: *Gain of interband transitions occurring between the conduction and valence-band (a) and intersubband transitions (b) in a quantum-well. Source: adapted from [30, Fig. 3.1].*

lowest level of the active region. This could lead to a back-filling process of the lower lasing level which is unwanted and impacts the performance of the laser. One approach to solve this issue is presented by the two phonon extraction process [29, Ch. 7].

QCLs normally consist of 10 to up to 100 cascaded stages, each consisting of an injector and an active region. This cascading process has two main advantages. First, electrons emit multiple photons depending on the number of periods. Due to this recycling process, the driving current can be reduced to generate the equal amount of photons. Second, the gain area is enlarged which lowers the required driving current density. Despite its advantages, the cascading of stages increases the required bias of operation. Overall, this process decreases the ohmic losses in QCLs [29, Ch. 7]. Further information about this type of laser can be found in [29].

2.1.1 Interband vs. Intersubband lasers

Intersubband and interband lasers are based on different photon generation processes. While interband lasers rely on the radiative recombination of electrons and holes, intersubband systems utilize mini-bands or discretized states in one band as introduced above. This fundamental difference also influences the bandwidth and the emission frequency of

both types. In case of interband lasers, the emission frequency is fundamentally limited by the bandgap of the material. Since the transition in QCLs only occurs in one band, the emission wavelength is not constrained by the bandgap. However, its minimum wavelength is limited by the conduction-band offset [5, Ch. 18.4].

A second differentiation is presented by the joint density of states. In case of intersubband transitions, this distribution is optically similar to the one of atomic systems. As depicted in Figure 2.2, the intersubband transition is transparent below and above the transition energy, while interband transitions absorb always at higher energies. This transparent behavior of intersubband transitions enables the stacking of different active regions utilized in heterogeneous QCLs [20–22]. This property will turn out to be a key aspect in the numerical implementation of the gain discussed in section 3.6. In addition to the different joint density of states, the broadening mechanisms of the gain spectrum further differentiate both types [29, Ch. 1].
Third, the gain is maximized differently in both types of lasers. In interband lasers, this is achieved by minimizing the transparency current by confining the recombination area. This can be achieved, for instance, by using a quantum-well design. The maximum current is restricted either by the heat generated or by the damage to the facets. For intersubband lasers, gain is maximized by the design of the active region and by minimizing other types of losses. The maximum current is defined by the alignment of the band structure and the doping of the device [29, Ch. 7].

Another difference can be found in the dynamics of the gain. A gain medium is considered to be fast if the gain recovery time is lower than the round trip time of the cavity. Due to their fast scattering times, normally in the pico- or even in the subpico-second range, QCLs are considered as fast gain media. Interband semiconductor lasers possess slow gain dynamics with gain recovery times in the nanosecond scale [24, Ch. 3.3]. The fast gain property of QCL has significant benefits in its modulation properties. According to [29, Ch.13], QCLs have a considerable modulation capability reaching up to 100GHz. However, the fast gain dynamics also trigger the effect of spatial hole burning (SHB) since the gain is reduced spatially where the intensity is high. This gain grating is not washed out efficiently by diffusion in fast gain media and triggers multi-mode operation [24, Ch. 5.4]. This effect impacts the spatial intensity distribution computed in chapter 4 and will be a part of the model described in the next section.

2.2 Analytical description

The full analytical model of a laser system is complex and involves many coupled differential equations as shown in [24, Ch. 3]. While first models were based on the rate equation, which does not include the phase information of light, the analysis shown in this work is based on the *Maxwell-Bloch equations*. This set of equations is a model describing the propagation of light (Maxwell's equation) and its interaction with an open two-level system (Bloch-Equations). Maxwell's and Bloch's equations are coupled over the

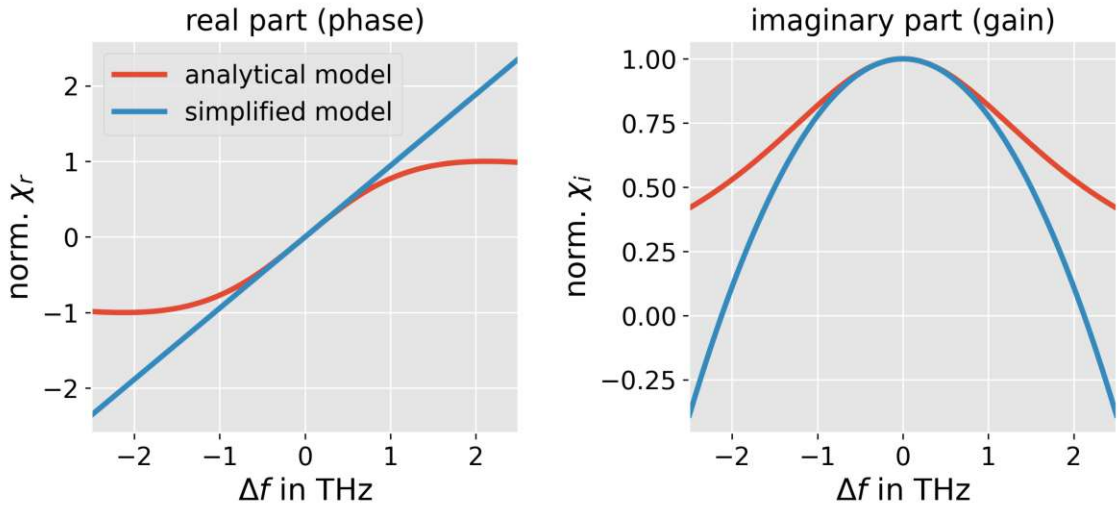

Figure 2.3: *Real and imaginary part of the susceptibility χ. The equations of the analytical model and its simplification were taken from [24, eq. 3.83 and 6.17]. The used parameters can be found in chapter A.*

macroscopic polarization. Since this set of coupled equations does not reveal an intuitive understanding of the underlying physics, the analytical description was simplified.

A key part of this simplification is the elimination of the polarization equation. Its impact is displayed in Figure 2.3. The imaginary part of the susceptibility χ_i influences the phase of the electric field while its real part χ_r impacts the gain of the medium. This relation can be readily derived by assuming that $\chi_r \ll 1$ as shown in [24, Ch. 3]. By analyzing the accuracy of the approximation, one can clearly see that the simplified model describes the susceptibility precisely until the bandwidth overcomes the typical gain bandwidth of a QCL of about 1 THz. By incorporating further simplification for fast gain media, the model can be reduced to a single master equation. This equation has revealed much new information regarding QCLs, especially in the field of optical frequency combs [31–34].

However, for the simulation of broadband QCLs, especially for heterogeneous QCLs, the elimination of the polarization equation can not be conducted since the approximation induces losses above and below the center frequency. This is in contradiction to the expected behavior shown in Figure 2.2 b. The governing equation is coupled with the polarization equation in order to obtain a transparent medium in these spectral ranges. Chapter 3 continuously expands this governing equation based on the one-dimensional wave-equation to include dominant physical effects present in a QCL.

Figure 2.4 displays the main components of the model. All the effects presented result from the physical behavior of the fast gain medium.
This includes:

Figure 2.4: *Schematic drawing of a Fabry-Pérot laser cavity outlining the main components of the analytical description: losses, group velocity dispersion (GVD), third and fourth-order group velocity dispersion (TOD and FOD), gain, spatial hole burning (SHB), and the Kerr-effect.*

1. Waveguide losses due to scattering and absorption of the material between the two facets [5, p. 442].

2. Group velocity dispersion (GVD) and 3. higher-order dispersion (third-order (TOD) or fourth-order (FOD)) effects due to the frequency dependence of the refractive index n. This effect leads to chirping which is best explained by means of pulses. If a transform-limited pulse[1] propagates through a dispersive medium, its instantaneous frequency changes during the length of the pulse, and the overall shape broadens. A more detailed description can be found in [5, Ch. 23] and [28, Ch. 3.2].

4. The gain of the medium as depicted in Figure 2.3.

5. Spatial hole burning (SHB) being present in fast gain media. In a Fabry-Pérot laser system, the counter-propagating electric field waves generate a standing wave pattern where the inversion is depleted. In conventional interband lasers, this effect can be efficiently washed out by diffusion. In fast gain resonators, such as QCLs, this is not possible due to its fast intersubband scattering mechanisms [24, Ch. 5.4].

6. The Kerr-effect describes the impact of the intensity on the refractive index n [5, Ch. 22]. This nonlinear effect can be taken into account by an additional term in the governing equation as shown in [31] which is not used in this model. The Kerr-effect will be taken into account by a non-zero linewidth enhancement factor (LEF) representing its main origin. Based on the Kramers-Kronig relations, coupling real and imaginary part of the susceptibility χ, the LEF takes the extent of the impact of an asymmetric gain profile on the refractive index into account. The LEF has already been analyzed in detail in [24, Ch. 6] and will not be discussed in more detail in this work.

2.3 Finite difference method

Finding an analytical solution of a *partial differential equation (PDE)* is mostly not possible, especially if the grade of complexity is high. Numerical methods, among them the

[1] a pulse with a minimum time-bandwidth product.

finite difference method and the *finite element method*, have become viable tools in solving many different types of PDEs. In this work, the focus is set on the *finite difference method*, which solves the problem in an approximative manner. [35, Ch. 11].

To introduce this method, the Taylor approximation of the function $U(x_0 + \Delta x)$ around x_0, written as

$$U(x_0 + \Delta x) = U(x_0) + \frac{\partial U(x)}{\partial x}\Delta x + \frac{\partial^2 U(x)}{\partial x^2}\frac{1}{2}(\Delta x)^2 + \cdots, \tag{2.2}$$

is considered.
By rearranging this equation, one obtains

$$\frac{\partial U(x)}{\partial x} = \frac{U(x_0 + \Delta x) - U(x_0)}{\Delta x} + O(\Delta x). \tag{2.3}$$

The first derivative can therefore be approximated by the *forward difference quotient*

$$\frac{\partial U(x)}{\partial x} \approx \frac{U(x_0 + \Delta x) - U(x_0)}{\Delta x}. \tag{2.4}$$

In a similar way, one can derive the *backward difference formula* given by

$$\frac{\partial U(x)}{\partial x} \approx \frac{U(x_0) - U(x_0 - \Delta x)}{\Delta x}. \tag{2.5}$$

Another approximation can be derived by combining the Taylor approximations of $U(x + \Delta x)$ and $U(x - \Delta x)$ leading to

$$\frac{\partial U(x)}{\partial x} = \frac{U(x_0 + \Delta x) - U(x_0 - \Delta x)}{2\Delta x} + O((\Delta x)^2), \tag{2.6}$$

which is the basis of the *central difference formula*

$$\frac{\partial U(x)}{\partial x} \approx \frac{U(x + \Delta x) - U(x - \Delta x)}{2\Delta x}. \tag{2.7}$$

In a similar fashion, approximations for second-order derivatives can be calculated as shown in [35, Ch. 11].

To sum up, the principle behind the *finite difference method* to obtain a good approximation of the solution relies on discretizing the variables and their derivatives. However, not every strategy leads to a stable output or approximates the solution sufficiently. It is therefore necessary to evaluate these aspects.

The strongest property is **convergence**, which means that in case of an infinitesimal small grid ($\Delta t \to 0$ and $\Delta z \to 0$), the solution obtained by the numerical mean approaches the real solution [35, Ch.11]. The criteria of convergence may be difficult to prove directly. An alternative to this direct proof is presented by the *Lax Equivalence Theorem*, which

states that a **consistent** and **stable** implementation is also convergent [36, Ch. 2]. Both properties are, therefore, required to obtain a trustworthy solution of the equation.

The one-dimensional wave-equation of first-order, describing the advection problem, should serve as an introductory example since it represents the starting point of the finite difference model described in chapter 3. This equation, written for the electric field E, is given by

$$\frac{\partial E(z,t)}{\partial t} + c\frac{\partial E(z,t)}{\partial z} = 0 \tag{2.8}$$

where c is the propagation velocity. In case the velocity is positive ($c > 0$), the equation can be discretized by using a regular grid and the up-wind scheme (forward in time and backward in space). This leads to

$$E(z_0, t_0 + \Delta t) = c\frac{\Delta t}{\Delta z}\left(E(z_0 - \Delta z, t_0) - E(z_0, t_0)\right) + E(z_0, t_0) \tag{2.9}$$

as shown in [37].
It should be emphasized that the type of PDE should influence the used discretization scheme [35, Ch.11].

2.3.1 Modified equation approach

In order to interpret the result obtained by the numerical implementation, the *modified equation approach* can be used for linear PDEs. This method leads to an analytical equation, which is actually solved by the discretized scheme. The obtained expression can then be compared to its original form. Additionally, this approach can be used to prove stability and consistency. The modified equation is derived in two steps. In the first step, every term in the discrete version of the PDE is replaced by its Taylor-expansion around $E(z_0, t_0)$ [38].

In case of the discrete wave-equation (equation 2.9), this results in

$$\begin{aligned}\frac{\partial E(z,t)}{\partial t} + c \cdot \frac{\partial E(z,t)}{\partial z} = &-\frac{\Delta t}{2}\frac{\partial^2 E(z,t)}{\partial t^2} - \frac{\Delta t^2}{6}\frac{\partial^3 E(z,t)}{\partial t^3} + O(\Delta t^3) \\ &+ c\frac{\Delta z}{2}\frac{\partial^2 E(z,t)}{\partial z^2} - c\frac{\Delta z^2}{6}\frac{\partial^3 E(z,t)}{\partial z^3} + O(\Delta z^3)\end{aligned} \tag{2.10}$$

as shown in [37]. As a consequence of the approximation made by the finite difference approach, terms appear on the right-hand side of the equation. In the second step, the new terms are being converted to a form that one can interpret physically. The temporal derivatives are, therefore, being converted into spatial ones. For instance, to convert the second time derivative of the truncation error, the equation is multiplied by the operator $-\frac{\partial}{\partial t}\frac{\Delta t}{2}$ and is added to the equation 2.10. This raises, however, another mixed term in the result that has to be eliminated in the next step. Here, it should be emphasized that equation 2.10 has to be used for this process and not the original PDE [38].

By continuing this process, the modified equation

$$\begin{aligned} E_t(z,t) + c \cdot E_z(z,t) = & \frac{c\Delta z}{2}\left(1-\nu\right) E_{zz}(z,t) \\ & - \frac{c(\Delta z)^2}{6}\left(2\nu^2 - 3\nu + 1\right) E_{zzz}(z,t) \\ & + O(\Delta z, \Delta t)^3 \end{aligned} \tag{2.11}$$

is obtained as shown in [39], with $\nu = c \cdot \frac{\Delta t}{\Delta z}$.
By comparing the modified equation with the original equation, it can be seen that the scheme imposes numerical dispersion and diffusion with parameters depending on the spatial and temporal grid spacing (Δz and Δt). Hence, the *advection-diffusion-dispersion equation* is actually solved by the scheme [37].

2.3.2 Consistency and order of accuracy

The modified equation contains the original PDE and a truncation error originating from the used finite difference formulas. The scheme is consistent with the original equation if the modified equation approaches the original PDE in case the time and space steps tend to zero. The *order of accuracy* represents the lowest order of Δt and Δz appearing in the modified equation [38]. Hence, equation 2.11 is consistent and features first-order accuracy.
In other words, the higher the order of accuracy the better the approximation made by the modified equation. It is important to note that a higher-order scheme does not directly lead to a more accurate result. The connection between the order of consistency, describing the accuracy of the modified equation, and the order of convergence, outlining the precision of the obtained solution, is given by the Lax-Theorem [36, Ch. 2]. If this theorem is fulfilled, a higher-order of consistency always improves the obtained solution.

2.3.3 Stability

Since the grid spacing cannot approach zero, an additional property is required to ensure that the solution evolves as expected. This additional requirement arises from the stability property [40, Ch. 1.5]. A common approach to investigate stability is represented by the *von Neumann analysis* [40, Ch. 2.2]. Before discussing this feature in detail, the general idea behind this criterion is introduced. A numerical scheme is called stable if slight deviations in the input of the system to solve only lead to restricted changes in the result [35, p. 314]. The general concept of the von Neumann analysis is outlined in this section for a two-level scheme (two time steps are involved) and is illustrated by the discrete one-dimensional wave-equation (equation 2.9). In addition, this part sheds light on the relation between this concept of stability and the modified equation approach.

The *von Neumann analysis* is based on the Fourier transformation. By applying this transformation spatially to the discrete wave-equation, one yields

$$E(k, t_0 + \Delta t) = \underbrace{\left[1 - c\frac{\Delta t}{\Delta z}(1 - e^{-jk\Delta z})\right]}_{g(k)} E(k, t_0). \tag{2.12}$$

Here, $g(k)$ is the *amplification factor* as defined in [40, Ch. 2.2]. Since Δt and Δz are constant, the scheme is stable if

$$|g(k)| \leq 1 \tag{2.13}$$

as shown in [40, p. 50]. By inserting the amplification factor of the discrete wave-equation into the stability condition shown above, one obtains

$$\left|c\frac{\Delta t}{\Delta z}\right| \leq 1. \tag{2.14}$$

Therefore, the implementation shown in equation 2.9 is convergent[2] if this stability criterion is fulfilled.

With the *von Neumann analysis*, a powerful method is provided to prove the stability of finite difference schemes. However, the modified equation also provides evidence of stability as shown in [38]. The basis of the relationship between the von Neumann analysis and the modified equation is laid down by assuming that

$$E(z, t) = e^{\alpha t} e^{jkz} \tag{2.15}$$

represents a general solution of equation 2.11. Thereby k is the wave number and $\alpha = a + jb$. By observing the temporal development of this solution, one can, similar to the von Neumann approach, define an amplification factor. Therefore, for one time step, this factor is given by

$$g_m(k) = e^{(a+jb)\Delta t}. \tag{2.16}$$

Since both representations describe the solution of the discretized PDE, both amplification factors are equal. Furthermore, by investigating the relationship between the terms of the modified equation and the coefficients a and b, the following expressions can be derived

$$a = \sum_{i=1}^{\infty} (-1)^i k^{2i} \mu(2i) \tag{2.17}$$

$$b = \sum_{i=0}^{\infty} (-1)^i k^{2i+1} \mu(2i+1) \tag{2.18}$$

Here, $\mu(2i)$ are the even, and $\mu(2i+1)$ are the odd order coefficients of the spatial derivatives of the modified equation. To clarify the terms required, the first three terms of

[2] It was assumed that the Lax Equivalence Theorem is valid for the problem.

equation 2.11 are given by

$$E_t(z,t) = \underbrace{-c}_{\mu(1)} \cdot E_z(z,t) \underbrace{+\frac{c\Delta z}{2}(1-\nu)}_{\mu(2)} E_{zz}(z,t) \underbrace{-\frac{c(\Delta z)^2}{6}\left(2\nu^2 - 3\nu + 1\right)}_{\mu(3)} E_{zzz}(z,t) + O(\Delta z, \Delta t)^3. \tag{2.19}$$

In this context, it becomes more comprehensible why stability demands $|g_m| \leq 1$. $a \leq 0$ means that the amplitude of the solution decays or remains equal but does not increase according to equation 2.15. For small wave-numbers ($k \to 0$), the lowest even order term $\frac{c\Delta z}{2}(1-\nu)$ (equation 2.19) defines the stability condition[3] which leads to

$$c\frac{\Delta t}{\Delta z} \leq 1. \tag{2.20}$$

Since c, Δt, and Δz are assumed to be positive, the condition above corresponds to the von Neumann stability condition (equation 2.14).

Normally, the small wave number assumption only leads to a necessary condition for stability. However, in this specific case it is also sufficient [38].

2.3.4 Explicit and implicit schemes

In general, the implementation of a differential equation by means of the finite difference method can be subdivided into *explicit* and *implicit* schemes. The difference between these two schemes lies in how the solution for the next time step is calculated. In case of an explicit technique, the solution for the next time step can be written explicitly[4]. This is in contrast to implicit schemes, where a system of equations has to be solved. This significant drawback is often counterbalanced by a, on average, better behaving solution (for instance higher accuracy) [35, Ch.11]. The difference between these two schemes will play an important role in the development of the finite difference model described in chapter 3.

2.3.5 Higher-order schemes

The accuracy of finite difference approaches can be improved by a finer or different grid and by increasing the order of the scheme. In the first case, terms approaching on the right-hand side of the modified equation are getting smaller. In the second case, lower-order terms are being eliminated. Both variants change the truncation error [36, Ch. 1].

[3] In comparison to the analysis shown in [38], the investigation was not restricted to damped solutions.
[4] For instance equation 2.9

The derivation of higher-order finite difference formulas is similar to the derivation shown at the beginning of this section. The principle of this method is outlined by calculating a higher-order finite difference formula of $\frac{\partial^2(E(z)}{\partial z^2}$.
First, the used approximation of the derivation is written down by

$$\frac{\partial^2(E(z)}{\partial z^2} \approx c_1 E_{i-2} + c_2 E_{i-1} + c_3 E_i + c_4 E_{i+1} + c_5 E_{i+2}. \tag{2.21}$$

Here, $E_i = E(z_0 + i\Delta z)$ and c_1, c_2, c_3, c_4, c_5 are the coefficients to determine. Second, all points used in the discretization are being Taylor expanded around $E(z_0)$. This leads to

$$\begin{aligned}\frac{\partial^2 E(z)}{\partial z^2} \approx & c_1 \left[E_i + (E_z)_i(-2\Delta z) + \frac{(-2\Delta z)^2}{2}(E_{zz})_i \dots \right] \\ & + c_2 \left[E_i + (E_z)_i(-\Delta z) + \frac{(-\Delta z)^2}{2}(E_{zz})_i \dots \right] \\ & + c_3 \cdot E_i \\ & + c_4 \left[E_i + (E_z)_i(\Delta z) + \frac{(\Delta z)^2}{2}(E_{zz})_i \dots \right] \\ & + c_5 \left[E_i + (E_z)_i(2\Delta z) + \frac{(2\Delta z)^2}{2}(E_{zz})_i \dots \right].\end{aligned} \tag{2.22}$$

In order to obtain a solvable system of equations, two preparation steps are required. In the first step, the approximation is sorted by the derivations of E. Since five undetermined coefficients are used, the approximation is cut off after the fourth-order of Δz. Finally, the right-hand side of the equation is determined by taking into account that the second-order derivation is being approximated by the higher-order scheme. This yields the following equation

$$\begin{bmatrix} 1 & 1 & 1 & 1 & 1 \\ -2 & -1 & 0 & 1 & 2 \\ (-2)^2/2 & (-1)^2/2 & 0 & 1/2 & 2^2/2 \\ (-2)^3/3! & (-1)^3/3! & 0 & 1/3! & 2^3/3! \\ (-2)^4/4! & (-1)^4/4! & 0 & 1/4! & 2^4/4! \end{bmatrix} \cdot \begin{bmatrix} c_1 \cdot 1 \\ c_2 \cdot \Delta z \\ c_3 \cdot (\Delta z)^2 \\ c_4 \cdot (\Delta z)^3 \\ c_5 \cdot (\Delta z)^4 \end{bmatrix} = \begin{bmatrix} 0 \\ 0 \\ 1 \\ 0 \\ 0 \end{bmatrix}. \tag{2.23}$$

By solving the system above, one obtains

$$\frac{\partial^2(E(z)}{\partial z^2} \approx \frac{-E_{i-2} + 16E_{i-1} - 30E_i + 16E_{i+1} - E_{i+2}}{12(\Delta z)^2}. \tag{2.24}$$

The Taylor expansion (equation 2.22) was cut off after the fourth-order term, which would lead to a fifth-order scheme. Since c_1 is divided by Δz^2, the minimum achievable order would be three. Fortunately, in this case also the next higher-order term

$$\frac{(-2)^5}{5!}(-1) + \frac{(-1)^5}{5!}16 + \frac{1^5}{5!}16 + \frac{2^5}{5!}(-1) = 0 \tag{2.25}$$

which increases the accuracy to the fourth-order. [36, Ch. 1].
An online tool for the calculation of higher-order finite difference can be found in [41]

The previously described method to obtain a higher-order scheme is a powerful tool to increase the accuracy if needed. However, raising the number of points may pose a difficulty on the boundary of the simulation area. Here, only a few points are normally known depending on the problem. Therefore, *numerical boundary conditions* have to be defined to overcome this issue [36, Ch. 1].
These boundary conditions are, in general, treated by either using one-sided difference formulas or by utilizing extrapolating techniques [42]. A similar issue is addressed in [43, Ch. 10], which proposes a startup procedure as treatment. It is noteworthy to take into consideration that the kind of procedure used for the numerical boundary condition may also impact the accuracy and the stability of the scheme [44].

CHAPTER 3

FINITE DIFFERENCE MODEL

The analytical description of quantum cascade lasers is complex and involves many different effects as introduced. This part describes the numerical implementation of a QCL model based on the first-order wave-equation. The first section explains the derivation and the implementation of the wave-equation and examines the impact of the relation between the time and the space discretization step size. Section 3.2 describes the testing model used to analyze the impact of different schemes. After this introduction, the first-order wave-equation is extended to include wave-guiding losses, group velocity dispersion effects, and gain. The spectral accuracy of the different implementations is analyzed in detail along with the required stability criterion.

The developed model is based on a narrow-band QCL model developed by N. Opačak [24] as introduced. This narrow-band model described by the master equation for fast gain media is based on the elimination of the polarization equation. The model cannot be used for the simulation of heterogeneous QCL for two main reasons. First, the implementation of the group velocity dispersion is unstable. This unstable behavior is compensated by the additional losses induced by the polarization elimination (Figure 2.3). As a result, the model becomes unstable in case the polarization equation is taken into account. Second, the already existing implementation of the polarization equation induces numerical losses above and below the center frequency. Therefore, the implementation has to be improved to obtain a transparent medium at these spectral areas.

This chapter expands and refines the previously used implementation to a large extent to enable the simulation of a heterogeneous QCL. The analysis is focused on the accuracy and the stability property. In case of the losses and the group velocity dispersion, the term "previously used" refers to the implementation used by N. Opačak. The description in this chapter requires knowledge about Laplace, Fourier, and the time discrete Fourier transformation. For further information about these transformations, please refer to [45, 46].

3.1 Wave-equation

The propagation of light is described by Maxwell's equations, which lead in one dimension to the wave-equation

$$\frac{\partial^2 E(z,t)}{\partial z^2} - \frac{n^2}{c_0^2}\frac{\partial^2 E(z,t)}{\partial t^2} = 0 \tag{3.1}$$

for a current and charge-free area [28, Ch. 1]. Here, E is the electric field, n is the refractive index, and c_0 is the speed of light in vacuum. In a Fabry-Pérot resonator, light propagates back and forth between the two mirrors. This means the electric field consists of two counter-propagating waves

$$E = \frac{1}{2}\left(E_+(z,t)\cdot e^{j(\omega_0 t - k_0 z)} + E_-(z,t)\cdot e^{j(\omega_0 t + k_0 z)} + c.c.\right) \tag{3.2}$$

where E_+ and E_- are the envelopes of the to the right and to the left traveling wave of the electric field, $k_0 = n(\omega_0)\frac{\omega_0}{c_0}$, and $\omega_0 = 2\pi f_0$ with f_0 representing the center frequency of operation. *c.c.* denotes the complex conjugate form. By substituting equation 3.2 into 3.1 and applying the *slowly varying envelope approximation (SVEA)*, the wave-equation for the right (E_+) and left (E_-) traveling envelopes yield to

$$\frac{n}{c_0}\frac{\partial E_\pm(z,t)}{\partial t} \pm \frac{\partial E_\pm(z,t)}{\partial z} = 0 \tag{3.3}$$

as shown in [24, Ch. 3].

The solution to these equations is given by

$$E_+(z,t) = f(n/c_0 \cdot z - t) \qquad E_-(z,t) = g(n/c_0 \cdot z + t). \tag{3.4}$$

where g and f are arbitrary functions. Since g and f only require one argument, the solutions are constant if $t - \frac{n}{c_0}z = \text{const.}$ and $t + \frac{n}{c_0}z = \text{const.}$ for E_+ and E_- respectively. These lines in space and time, known as characteristic lines, will be of use in the next section [47, Ch. 1.2].

3.1.1 Discretization of the wave-equation

The one-dimensional wave-equation can be discretized by using a first-order approach as shown in section 2.3. In this part, a similar numerical implementation is derived by means

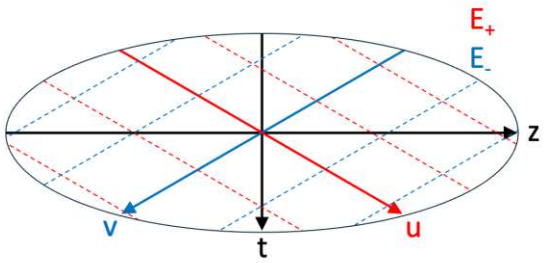

Figure 3.1: *Original (z,t) and new (u,v) coordinate system aligned with the characteristic lines (dashed curves) of the solutions.*

of a coordinate transformation along the characteristic lines as shown in Figure 3.1. This transformation is carried out since it delivers a more comprehensive model, which will be used in the following sections. The basis of the new coordinate system is laid out by the following relations

$$u = \frac{1}{2} \cdot \left(\frac{c_0}{n} t + z \right) \qquad v = \frac{1}{2} \cdot \left(\frac{c_0}{n} t - z \right) \tag{3.5}$$

or vice versa by

$$z = u - v \qquad t = \frac{n}{c_0} u + \frac{n}{c_0} v. \tag{3.6}$$

Similar to the approach shown in [47, p. 7], the spatial and temporal derivatives are being converted into the new coordinate system by

$$\frac{\partial E(u(z,t), v(z,t))}{\partial z} = \frac{\partial E}{\partial u} \underbrace{\frac{\partial u}{\partial z}}_{\frac{1}{2}} + \frac{\partial E}{\partial v} \underbrace{\frac{\partial v}{\partial z}}_{-\frac{1}{2}} \tag{3.7}$$

$$\frac{\partial E(u(z,t), v(z,t))}{\partial t} = \frac{\partial E}{\partial u} \underbrace{\frac{\partial u}{\partial t}}_{\frac{1}{2}\frac{c_0}{n}} + \frac{\partial E}{\partial v} \underbrace{\frac{\partial v}{\partial t}}_{\frac{1}{2}\frac{c_0}{n}}. \tag{3.8}$$

which leads to

$$\frac{n}{c_0} \frac{\partial E_+}{\partial t} + \frac{\partial E_+}{\partial z} = \frac{\partial E_+}{\partial u} = 0 \tag{3.9}$$

$$\frac{n}{c_0} \frac{\partial E_-}{\partial t} - \frac{\partial E_-}{\partial z} = \frac{\partial E_-}{\partial v} = 0. \tag{3.10}$$

The coordinate transformation has clearly simplified the equation of E_+ and E_- by reducing the number of derivatives. Their discretization can be carried out, for instance, by the forward difference formula (equation 2.4), which results in

$$E_+(z_0, t_0 + \Delta t) = E_+(z_0 - \Delta z, t_0) \tag{3.11}$$

$$E_-(z_0, t_0 + \Delta t) = E_-(z + \Delta z_0, t_0). \tag{3.12}$$

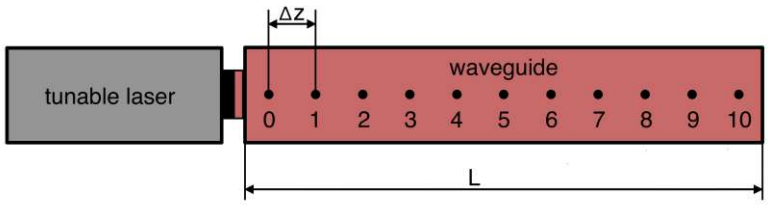

Figure 3.2: *Testing model consisting of a tunable single-mode laser and a wave-guiding structure.*

By comparing the above equations to 2.9 or by analyzing the relations given in 3.6, it becomes clear that the coordinate transformation imposes the following space-time relation

$$\Delta t = \frac{n}{c_0}\Delta z. \tag{3.13}$$

It is worth noting that this scheme is also stable since the expression above represents the upper boundary of the stability criterion derived in the previous chapter (equation 2.14). The same discrete version of the PDE can be derived by inserting the time-space relation (equation 3.13) into equation 2.9 for E_+.
In addition to the convergence property, this approach has a major advantage that becomes evident by inserting $\Delta t = \frac{n}{c_0}\Delta z$ into the modified equation (equation 2.11). The space-time relation sets $\nu = 1$, which implies that the truncation error vanishes. This seems also reasonable since 3.12 implies that the discrete points in the (z,t) coordinate system are transferred to the next point on the u or v axis without modification. Hence, the space-time relation, given in equation 3.13, was used for the implementation of the model. In order to present the following content in a concise and comprehensive manner, only the equation for $E_+ = E$ was described in detail. E_- can be implemented in a very similar way.

3.2 Testing model

In order to evaluate the results obtained by different numerical implementations, a test structure is required. As shown in Figure 3.2, the used model consists of a tunable single-mode laser and a waveguide. In addition, the reflectivity of the facets can be changed to transform the waveguide into a resonator. However, the reflectivity of both facets was set to zero for the development of the model. In the following, the wave-equation is constantly extended to implement further physical phenomena like *gain, losses, or the group velocity dispersion.*

Similar to the model described in [24, Ch. 3], the reflections (for instance on the facets of the laser) take place between the discretized points. The tunable laser features an additional point outside the cavity and transmits, without reflection, into the waveguide. The output of the system is represented by the last point within the cavity (point 10 in Figure 3.2).

As shown previously, the solutions of the wave-equation is given by $E(z,t) = f(n/c_0 \cdot z - t)$. However, by adding the laser to the structure the function f gets defined. Similar to [37], f is determined by the temporal function of the electric field of the laser.

By assuming that the laser produces a monochromatic oscillating field, the following ansatz can be made

$$E(z,t) = \hat{E} \cdot e^{-j(k_0 z - \omega_0 t)} \tag{3.14}$$

where E_0 is the amplitude, k_0 is the wave number, and $\omega_0 = 2\pi f_0$. By inserting 3.14 into the wave-equation, one obtains

$$k_0 = n\frac{\omega_0}{c_0} \tag{3.15}$$

similar to [28, Ch. 1.2].
To analyze the impact of different extensions of the wave-equation on the wave-guiding structure, the phase and the amplitude of the electric field are being detected at the output of the waveguide. The intensity of the tunable laser and the output intensity of the waveguide lead to the the gain coefficient

$$\gamma(f) = \frac{1}{L} ln\left(\frac{I(L)}{I(0)}\right) \tag{3.16}$$

as a function of frequency [5, p. 623]. Here $I(z)$ is the intensity of the laser beam depending on the position z. By means of the phase difference of in- and output, given by

$$\Delta\phi = \phi(0,t) - \phi(L,t) = k \cdot L, \tag{3.17}$$

the wave-number k and the refractive index n can be calculated ($k = n \cdot k_0$). Here, the phase is given by $\phi(z,t) = \omega t - kz$.
By rearranging the upper equation, one obtains

$$k = \frac{\Delta\phi}{L} \tag{3.18}$$

and the refractive index

$$n(f) = \frac{\Delta\phi}{k_0 L} \tag{3.19}$$

Both variables, especially k and its spectral derivatives, will be used in the following sections to evaluate the accuracy of different implementations.
In general, the simulations are being computed for a total time interval of one round trip[1]. To obtain the values for $\Delta\Phi(f)$ and $\gamma(f)$, the results are being averaged over the last quarter of the simulation time to improve the accuracy. Figure 3.3 depicts an example of a simulation result including losses and the group velocity dispersion (GVD). Since the discrete implementation of the $GVD(\Delta f) = \frac{\partial^2 k}{\partial \omega^2}$ by means of finite difference formulas is very noisy, the phase $\Phi(f)$ was approximated by a polynomial of order 7. To assess the correctness of the implementations, the label of the refractive index subplot $n(f)$ and

[1] The time required to propagate twice through the waveguide.

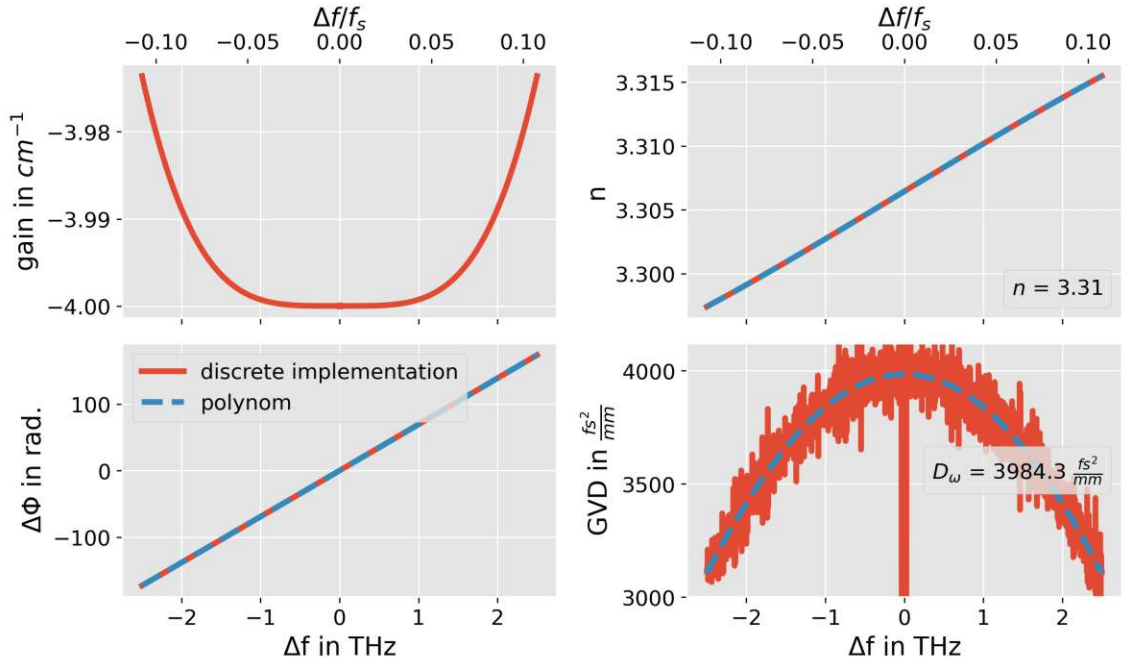

Figure 3.3: *Characteristic simulation showing the polynomial approximation of $\Delta\phi$ (blue dotted graph) to improve the noisy plot of the GVD by calculating the derivative by means of finite difference formulas (red graph). Here, $\Delta\Phi$ is the phase difference of the laser (input) and the output of the waveguide, f_s is the sampling frequency, n is the refractive index and GVD is the group velocity dispersion.*

the GVD(f) subplot show their value at $\Delta f = 0$ THz. In the following, the discrete implementation will be omitted for the dispersion plots (GVD and higher-order). In the case of n, the discrete implementation is plotted as a dashed line under the approximated polynomial to evaluate the correctness of the fitting process.

In order to simplify the discretized equation, the indexing of space and time is not being used directly. Similar to the coordinate transformation described previously, the propagation axis (u-axis) and the time will be used. Both different indexing techniques are displayed in Figure 3.4. In addition, to highlight the relation between Δz and Δt, Δu will be used for the discretization step size of the u-axis ($\Delta u = \Delta z = c_0/n \cdot \Delta t$).

Finally, since the equation for the envelope is being solved, the frequency has been shifted to the center wavelength ($\lambda = 8\mu m$). Unless otherwise specified, the simulation parameters are listed in chapter A.

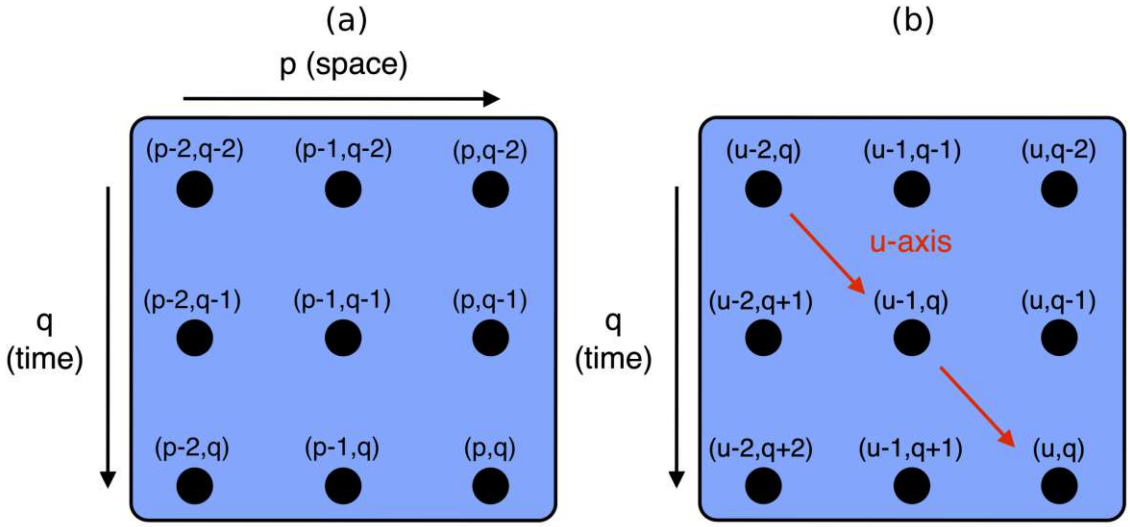

Figure 3.4: *Different indexing techniques: a) over space-time, and b) over the propagation direction (u-axis) and time.*

3.3 Waveguide losses

The wave-equation can be simply extended to include wave-guiding losses leading to

$$\frac{n}{c_0}\frac{\partial E(z,t)}{\partial t} + \frac{\partial E(z,t)}{\partial z} = -\frac{\alpha}{2}E(z,t) \quad \Leftrightarrow \quad \frac{\partial E}{\partial u} = \frac{\alpha}{2}E. \tag{3.20}$$

Here, α represents the power loss coefficient as shown in [24, Ch. 3.2].
This equation can be, analogous to the previous section, discretized by using forward, backward, or central differential formula (equation 2.4 - 2.7). This yields

$$\frac{E^{u,q} - E^{u-1,q}}{\Delta u} = -\frac{\alpha}{2}\begin{cases} E^{u-1,q} & \text{, (a) forward} \\ E^{u,q} & \text{, (b) backward} \\ \frac{1}{2}(E^{u,q} + E^{u-1,q}) & \text{, (c) central} \end{cases} \tag{3.21}$$

with the notation $E^{u,q} = E(u_0 + u \cdot \Delta z, t_0 + (q+u) \cdot \Delta t)$. The schemes are illustrated in Figure 3.5. In case of the central difference formula (version c), the point $E^{u+1/2,j}$ was constructed by taking the average of the the adjacent points on the u axis.
By rearranging 3.21, one obtains

$$E_+^{u,q} = E_+^{u-1,q} \cdot \begin{cases} (1 - \frac{\alpha}{2}\Delta u) & \text{, Version a (previously used)} \\ \frac{1}{1+\frac{\alpha}{2}\Delta u} & \text{, Version b} \\ \frac{2-\frac{\alpha}{2}\Delta u}{2+\frac{\alpha}{2}\Delta u} & \text{, Version c.} \end{cases} \tag{3.22}$$

Before the results of the different versions are being analyzed, another version based on

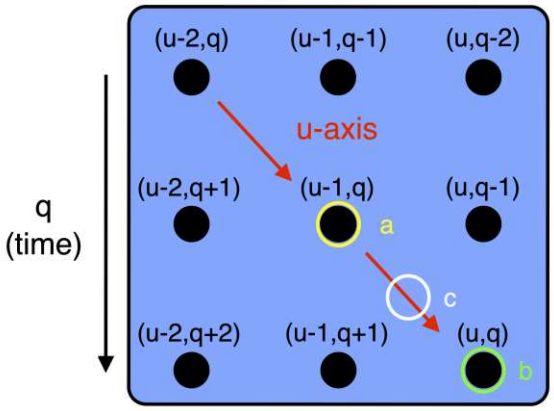

Figure 3.5: *Space and time discretization of the wave-equation including losses. The marked points represent the development points of the different versions.*

the *predictor corrector method* is introduced. For this purpose, version c is rearranged to

$$E^{u,q} - E^{u-1,q} = -\frac{\alpha}{2}\Delta u \frac{(E^{u,q} + E^{u-1,q})}{2}. \tag{3.23}$$

The predictor-corrector method is a two-step technique. In the predictor step, an approximation for $E^{u,q}$ is calculated whereas in the corrector step, the predicted expression is used to improve the solution. In this example, version a is used as a predicted value which is, in the second step, inserted into the right-hand side of equation 3.23. This procedure leads, after one iteration step, to Version d.

$$E^{u,q} = E_{+}^{u-1,q} \cdot \begin{cases} (1 - \frac{\alpha}{2}\Delta z) & \text{, Version a} \\ \frac{1}{1+\frac{\alpha}{2}\Delta z} & \text{, Version b} \\ \frac{2-\frac{\alpha}{2}\Delta z}{2+\frac{\alpha}{2}\Delta z} & \text{, Version c} \\ (1 - \frac{\alpha}{2}\Delta z + \frac{1}{2}(\frac{\alpha}{2}\Delta z)^2) & \text{, Version d} \end{cases} \tag{3.24}$$

One could also iterate a few times by using the result from the corrector step as a predictor for the next iteration. However, this iteration does not drastically improve the accuracy of the method and one should be advised to use a smaller grid step size instead [48, Ch. 17.6].

The four versions can be categorized into implicit and explicit implementations: Version a and d are explicit, and version b and c are implicit implementations. It is possible to rearrange all versions to $E^{u,q}$ since the equation features such a simple structure with only one derivative.

By analyzing the stability and consistency property by means of the methods introduced in section 2.3, one obtains that all versions are consistent with the original PDE (equation 3.20). The stability criterion and the order of accuracy are listed in Table 3.1.

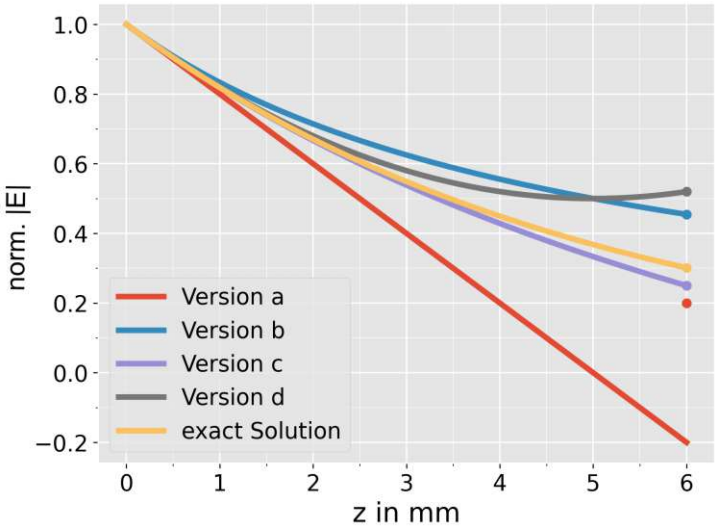

Figure 3.6: *Simulation results of the different loss implementations for $\Delta z = 6mm$. The results at $L = 6mm$ (dots) were computed by means of the simulation and the solid lines were calculated by equation 3.24. In addition, the exact solution is displayed to compare the accuracy of the versions.*

Version	Order of accuracy	Stability
a	1	$\Delta z \leq \frac{2}{\alpha}$
b	1	always
c	2	always
d	2	$\Delta z \leq \frac{2}{\alpha}$

Table 3.1: *Order of accuracy and stability criterion for the four loss implementations.*

By implementing the four versions, one obtains the simulation result shown in Figure 3.6 for a two-point discretization. One can clearly see that version a and d become unstable if Δz exceeds 5 mm. In particular, Version a becomes negative, and version d rises, which matches with the calculation results in Table 3.1. Another important point to mention is the accuracy of the versions. As shown in Figure 3.6, version c (central difference formula) and d (predictor-corrector method) represent the best approximations of the analytical exponentially decaying solution. The calculated order of accuracy also matches with the expectation in case of version c, since the central difference formula features a higher order than the one-sided ones as introduced (section 2.3).

Apart from stability and convergence, the different implementations can also be used to evaluate the convergence property. This is accomplished by conducting a Taylor-expansion around $\frac{\alpha}{2}\Delta z = 0$ of the exact solution and the amplification factor[2] of version b and c.

[2] The term which is being multiplied by $E^{u-1,q}$

This yields

$$\begin{aligned}
&\textbf{Exact solution:} && e^{-x} \approx 1 - x + \frac{x^2}{2} - \frac{x^3}{3!} + O(x^4) \\
&\textbf{Version a:} && 1 - x \\
&\textbf{Version b:} && \frac{1}{1+x} \approx 1 - x + x^2 - 6\frac{1}{3!}x^3 + O(x^4) \\
&\textbf{Version c:} && \frac{2-x}{2+x} \approx 1 - x + \frac{1}{2}x^2 - \frac{24}{16}\frac{1}{3!}x^3 + O(x^4) \\
&\textbf{Version d:} && 1 - x + \frac{1}{2}x^2
\end{aligned}$$

where $x = \frac{\alpha}{2}\Delta z$. The gray-marked expressions match with the Taylor approximation of the analytical solution. The number of marked terms can be interpreted as a sort of *order of convergence*[3] as defined in [36, p.45]. Since the order of convergence matches with the order of accuracy, the *Lax theorem* is fulfilled.

This theorem validates this situation for a two-level implementation of a linear initial value problem [36, p. 79]. The problem to be solved can be reformulated into an initial value problem, where the initial values propagate along the waveguide and are detected after a certain propagation time.

Before the final implementation of the losses is being discussed, the group velocity dispersion is included in the wave-equation.

3.4 Group velocity dispersion

In the previous section, the refractive index n was regarded as a constant. By including group velocity dispersion (GVD) effects, the refractive index becomes frequency dependent. In this section, the wave-equation is extended once more. The content is focused on the expansion of the wave-equation to include GVD effects. After this derivation, the numerical implementation is described in detail.

3.4.1 Integration of the GVD into the wave-equation

To incorporate this phenomenon into the wave-equation, the Fourier-transformation is applied to the wave-equation, yielding to

$$j\Delta\omega\frac{n}{c_0}E(z,\Delta\omega) + \frac{\partial E(z,\Delta\omega)}{\partial z} = -\frac{\alpha}{2}E(z,\Delta\omega). \tag{3.25}$$

[3] In [36, p.45], the order of convergence is defined with a norm. The specification of this norm was omitted in this case.

This differential equation can be solved analytically leading to the following expression for one spatial step

$$E(z_0 + \Delta z, \Delta\omega) = E(z_0, \Delta\omega) \cdot e^{-\frac{\alpha}{2}\cdot\Delta z} e^{-j\frac{n}{c_0}\Delta\omega\cdot\Delta z}. \tag{3.26}$$

Similar to the derivation shown in [28, Ch. 3.2], a Taylor approximation of the dispersion relation about ω_0 is conducted and truncated after the second-order term. This yields

$$k(\omega) - k(\omega_0) \approx \frac{\partial k}{\partial \omega}\Delta\omega + \frac{1}{2}D_\omega \Delta\omega^2 \tag{3.27}$$

where

$$D_\omega = \frac{\partial^2 k}{\partial \omega^2}, \tag{3.28}$$

and

$$\frac{\partial k}{\partial \omega} = \frac{1}{v_g} = \frac{n(\omega_0)}{c_0} + \frac{\partial n}{\partial \omega}\frac{\omega_0}{c_0} = \frac{N}{c_0}. \tag{3.29}$$

Here, v_g is the group velocity, N is the group index, and D_ω is the dispersion coefficient[4]. The second part of equation 3.29, $(\frac{\partial n}{\partial \omega}\frac{\omega_0}{c_0})$, causes the group velocity to deviate from the phase velocity, which leads to a different speed of propagation of the envelope and the carrier [28, Ch. 3.2].

Equation 3.26 represents the solution of the envelope in the frequency domain. By changing the description from the overall electric field to the envelope, the wave number has been shifted to $k(\omega_0)$ by equation 3.2. Therefore, the Taylor approximation of the dispersion relation ($\Delta k = k(\omega) - k(\omega_0)$) can be inserted into equation 3.26 and one obtains

$$E(z_0 + \Delta z, \Delta\omega) = E(z_0, \Delta\omega) \cdot e^{-\frac{\alpha}{2}\cdot\Delta z} e^{-j\frac{N}{c_0}\Delta\omega\Delta z} \cdot e^{-j\left[\frac{1}{2}D_\omega(\Delta\omega)^2\right]\Delta z}. \tag{3.30}$$

The latter equation reveals an important detail regarding the description of chirp. Apart from the influence of $n(\omega)$ on the speed of propagation, chirping can be interpreted as a phase filter in the frequency domain. This important detail becomes clear by analyzing the last term in equation 3.30, namely $e^{-j\left[\frac{1}{2}D_\omega(\Delta\omega)^2\right]\Delta z}$. The process of chirping does not influence the intensity spectrum [5, Ch. 23].

In the frequency domain, a complex $n(\omega)$ relation changes the speed of propagation and influences the phase of the envelope of the electric field. In order to derive a differential equation in the time domain, the previously shown process except the Taylor-expansion is reverted yielding to following differential equation

$$\frac{N}{c_0}\frac{\partial E}{\partial t} + \frac{\partial E}{\partial z} = -\frac{\alpha}{2}E + j\frac{1}{2}D_\omega\frac{\partial^2 E}{\partial t^2} \tag{3.31}$$

with reference to [28, Ch. 3.2].
A similar derivation of the additional GVD-term can be found in [24, Ch. 3.2].

[4] The definition of the group index N and the dispersion coefficient D_ω can be found in [5, p. 201], [28, Ch. 3.2] and [28, Ch. 1].

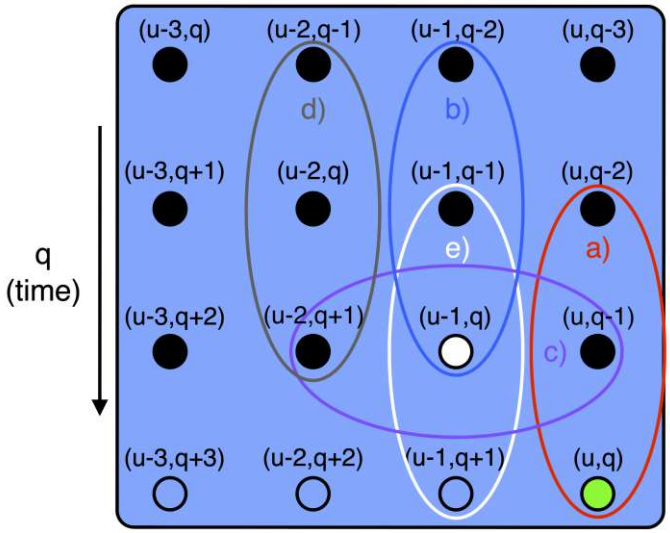

Figure 3.7: *GVD implementations by using different three point schemes. a) implicit version (marked in red) using a one-sided difference formula developed about $E^{u,q}$ (marked in green). Explicit versions about $E^{u-1,q}$ (marked in white) by b) using a one-sided difference formula (marked in blue), c) by converting the temporal derivative into a spatial derivative (marked in purple), d) shifting the derivative towards the minus u axis (marked in gray). The uncolored points cannot be used for the implementation due to parallel computing.*

3.4.2 Numerical implementation

The frequency dependence of the refractive index $n(f)$ changes the phase and the speed of propagation of the envelope as discussed previously. Since the difference in speed of propagation only imposes a temporal offset at the end of the waveguide, the group refractive index N is approximated by the refractive index n in the implementation. Furthermore, since the computation is based on GPU programming, which calculates every spatial point in parallel, only points in the past and the newly calculated point can be used for the implementation. In any other case, the discrete equations would be coupled, which would hinder an efficient parallel implementation and cause a drastic reduction in performance. Therefore, a central differential formula for the GVD-term cannot be used by taking $E^{u-1,q}$ as the development point as indicated in Figure 3.7 (version e). In case version e is implemented, the calculated point (u, q) depends on the new value of its left neighbor $(u-1, q+1)$. This dependency couples the discrete equations.

In general, three solutions can be found to circumvent this restriction. The different versions are displayed in Figure 3.7 by using three discrete points for the implementation of the GVD-term (equation 3.31). First, the most simple alternatives are one-sided difference formulas (version a and b). Second, temporal derivatives can be converted into spatial ones (version c). This imposes, however, a slight computation error due to the transformation. Third, central difference formulas can be shifted backward toward the minus u direction to implement the derivative centrally (version d). This back shifting process imposes as well an error into the simulation. As described previously, version e cannot be used since

the point (u-1,q+1) would couple the discrete equations. The points in space and time leading to such coupling are not colored in Figure 3.7.

The implementation of version a-d are given by

$$E^{u,q} = \begin{cases} \left[j2F\left(E^{u,q-1} - \frac{1}{2}E^{u,q-2}\right) - E^{u-1,q} \right] \cdot \frac{1}{jF-(1+\frac{\alpha}{2}\Delta z)} & \text{, Version a} \\ E^{u-1,q} \cdot (1 - \frac{\alpha}{2}\Delta z) + jF \cdot \left[E^{u-1,q} - 2E^{u-1,q-1} + E^{u-1,q-2} \right] & \text{, Version b} \\ E^{u-1,q} \cdot (1 - \frac{\alpha}{2}\Delta z) + jF \cdot \left[E^{u-2,q+1} - 2E^{u-1,q} + E^{u,q-1} \right] & \text{, Version c} \\ E^{u-1,q} \cdot (1 - \frac{\alpha}{2}\Delta z) + jF \cdot \left[E^{u-2,q+1} - 2E^{u-2,q} + E^{u-2,q-1} \right] & \text{, Version d,} \end{cases} \tag{3.32}$$

where $F = \frac{D_\omega}{2}\frac{c^2}{n^2\Delta z}$. Version c was used previously by N. Opačak.
Version a and b can be implemented as described above without further modification. In case of version c and d, the boundary conditions for the calculation of the first spatial step are required. As introduced, these numerical boundary conditions are also needed for higher-order schemes. Similarly to that, a startup procedure will be implemented. This means, for the first spatial step, the GVD-coefficient D_ω is set to zero. One can also interpret this as the unknown points were extrapolated in a way that the discretized derivative is zero. To compare the results of version a-d, the first spatial step of all versions only includes losses.

By implementing the versions with a dispersion coefficient of $D_\omega = 4000\ fs^2/mm$ and a loss coefficient of $\alpha = 4\ cm^{-1}$, the simulation results depicted in Figure 3.8 are obtained. One would expect a spectrally constant GVD and loss profile. As shown in 3.8 a, all versions implement the given specification precisely at the center frequency. However, the difference in their order of accuracy can be clearly seen by comparing the one-sided versions (a and b) with the central implementations (c and d). Consequently, the central implementations approximate the specifications more accurately. Figure 3.8 b depicts a similar behavior for version c and d.

To analyze the mismatch between the central implementations in more detail, the time discrete Fourier-transformation and the Z-transformation are used. By applying both transformations to the GVD-term of version d, one obtains

$$GVD_d = jF\cdot(z-2+z^{-1}) \quad \Leftrightarrow \quad jF\cdot\left[e^{j2\pi f\Delta t}-2+e^{-j2\pi f\Delta t}\right] = jF\cdot\left[2\cos(2\pi\Delta t)-2\right] \tag{3.33}$$

with reference to [45].
In case of version d, the implementation leads to a cosine function in the frequency domain. In case of version c, the coefficients of z and z^{-1} do not match due to the approximation made. This causes the gain profile of version c (Figure 3.8 b) to deviate more from the expected behavior. Apart from the gain profile, both central versions show a similar behavior. Since version d best meets expectations, this version is used for further analysis.

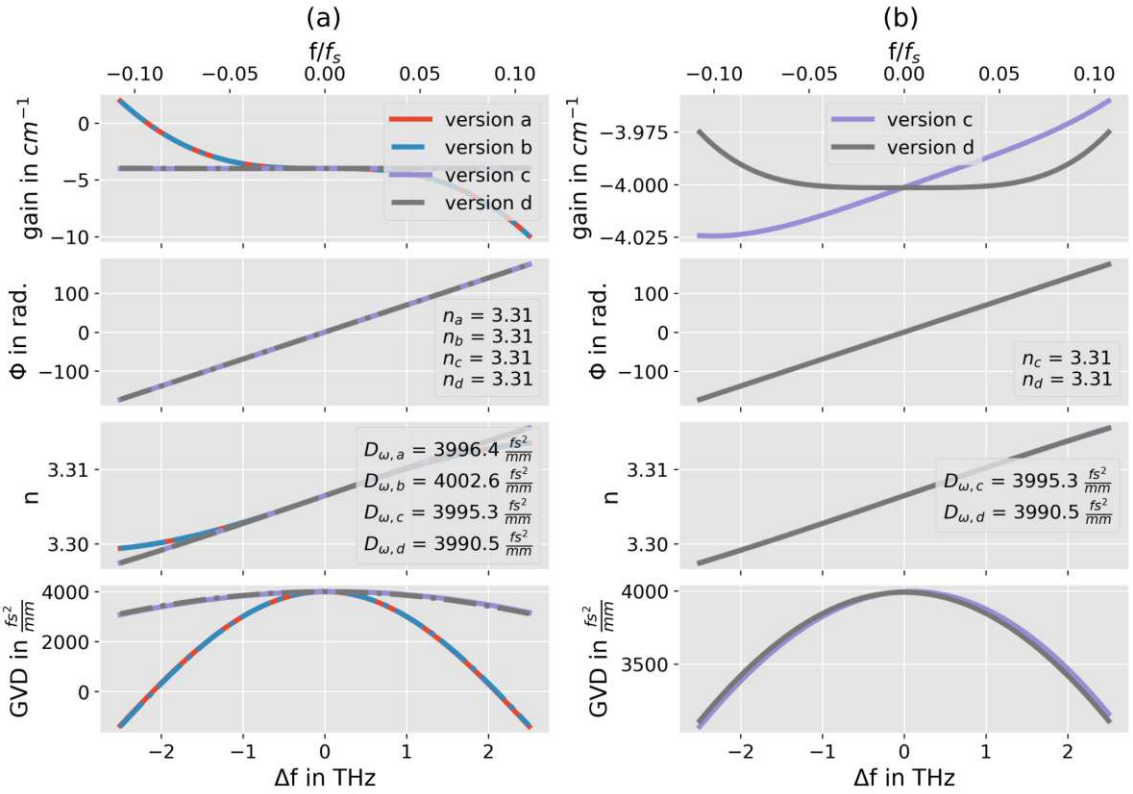

Figure 3.8: *GVD simulation results of the different three point versions shown in Figure 3.7: (a) one-sided (version a, b) and central (version c, d) finite difference implementations. Fig. (b) depicts the different impact of back-shifting the finite difference formula along the minus u-axis (version d) and its conversion to the spatial domain (version c). The first calculation step only includes losses due to the numerical boundary conditions. Simulation parameters:* $L = 1mm$, $N = 257$, $\alpha = 4cm^{-1}$ *and* $D_\omega = 4000fs^2/mm$.

In addition, since the phase profile does not show any significant difference between the versions, its presentation will be omitted in the following content.

Exponential Integrator

In the previous part, different GVD-implementations were discussed, leading to the following conclusion: temporal derivatives are best implemented centrally by shifting the finite difference formula along the minus u-axis until parallel computation is possible. In case of losses, version b-d in equation 3.7 were using the loss-implementation of version a (equation 3.24). As shown at the end of section 3.3, this loss implementation is the first-order approximation of the analytical solution. Is it possible to use the analytical solution instead of the approximation to increase the overall accuracy of the implementation?

This question can be answered by means of the exponential integrator shown in [49]. The differential equation to be solved can be condensed down to

$$\frac{\partial E}{\partial u} = -\frac{\alpha}{2} + R(u) \tag{3.34}$$

where $R(u)$ represents the additional terms of the equation (GVD, FOD, TOD, and gain). By applying the *variation of constants* formula to the upper equation, one obtains

$$E(u_0 + \Delta u) = E(u_0) \cdot e^{-\frac{\alpha}{2} \cdot \Delta u} + \int_0^{\Delta u} e^{\left[-(\Delta u - s)\frac{\alpha}{2}\right]} \cdot R(E(u_0 + s))\partial s. \tag{3.35}$$

Here, $u_0 = (z_0, t_0)$.
The above equation implements the losses in the most accurate way. However, some approximations are required to implement the other terms appearing within the integral on the right-hand side. By approximating $R(E(u + s))$ with $R(E(u))$, one yields

$$E(u_0 + \Delta u) = E(u_0) \cdot e^{-\frac{\alpha}{2} \cdot \Delta u} + \Delta u \frac{e^{-\frac{\alpha}{2}\Delta u} - 1}{-\frac{\alpha}{2}\Delta u} \cdot R(u_0). \tag{3.36}$$

By a first-order Taylor approximation of the exponential function in the gray-marked term, the following expression is derived:

$$E(u_0 + \Delta u) = E(u_0) \cdot e^{-\frac{\alpha}{2} \cdot \Delta u} + \Delta u \cdot R(u_0) \tag{3.37}$$

The upper expression shows that it is possible to implement the losses analytically by retaining a finite difference implementation of the other terms. This becomes apparent by comparing the above expression to the GVD-versions b-d in equation 3.32.

Impact of higher-order schemes and the back-shifting process

The accuracy of the numerical implementation can be increased by its order and by reducing the spacing of the grid as introduced. Since central difference formulas approximate the derivative more precisely, one-sided formulas are not examined further. Higher-order central difference coefficients can be readily calculated by the method described in section 2.3.5 yielding to following different implementations

$$\begin{aligned} E^{u,q} &= e^{-\frac{\alpha}{2}\Delta z} \cdot E^{u-1,q} \\ &+ jF \cdot \begin{cases} E^{u-4,q+1} - 2E^{u-4,q} + E^{u-4,q-1} & \text{, 3 points implementation} \\ \Big[-E^{u-4,q+2} + 16E^{u-4,q+1} & \\ -30E^{u-4,q} + 16E^{u-4,q-1} - E^{u-4,q-2}\Big]/12 & \text{, 5 points implementation} \\ \Big[2E^{u-4,q+3} - 27E^{u-4,q+2} + 270E^{u-4,q+1} & \\ -490E^{u-4,q} + 270E^{u-4,q-1} - 27E^{u-4,q-2} & \\ +2E^{u-4,q-3}\Big]/180 & \text{, 7 points implementation.} \end{cases} \end{aligned} \tag{3.38}$$

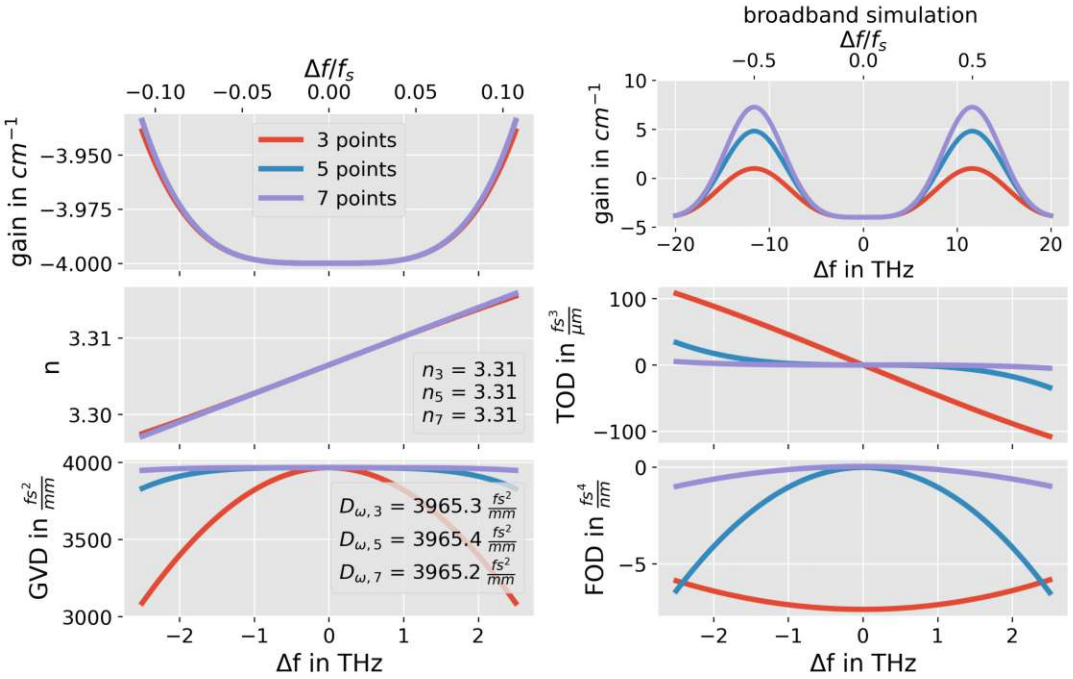

Figure 3.9: *Different GVD-simulations using three, five, and seven points for the central finite difference formula. The implementation is displayed in Figure 3.10. Simulation parameters:* $L = 1mm$, $N = 257$, $\alpha = 4cm^{-1}$ *and* $D_\omega = 4000fs^2/mm$

The different GVD-implementations are displayed in Figure 3.10. As shown in Figure 3.9, the degree of accuracy is enhanced drastically by increasing the total number of points used for the central implementation. While the version with three points deviates significantly from the expected constant spectral profile of the GVD, five and seven points approach the required profile more accurately. In addition, a higher-order scheme also has a beneficial impact on numerically generated higher-order dispersion terms such as third and fourth-order dispersion (TOD and FOD). Their impact decreases by increasing the order of the scheme. However, increasing the number of points features also a drawback. As depicted in the broadband simulation shown in Figure 3.9, higher-order implementations have an elevated impact on the spectral gain profile.

In a similar way, the back-shifting process was analyzed. As shown in Figure 3.11, the shifting process features a negligible influence on the spectral shape of the GVD as expected. In addition, the dispersion value at the center frequency changes in a negligible amount by comparing the three displayed versions. However, similar to the order influence, their contribution to the gain profile is different. The further backward the difference formula, the higher the impact. The depicted gain peaks at $|\Delta f| = f_s/2$, where f_s is the sampling frequency, which could possibly lead to a stability problem. In case the polarization elimination is applied (Figure 2.3), the gain profile induces losses aside from the area around the center frequency. Hence, the gain peaks would possibly not lead to an

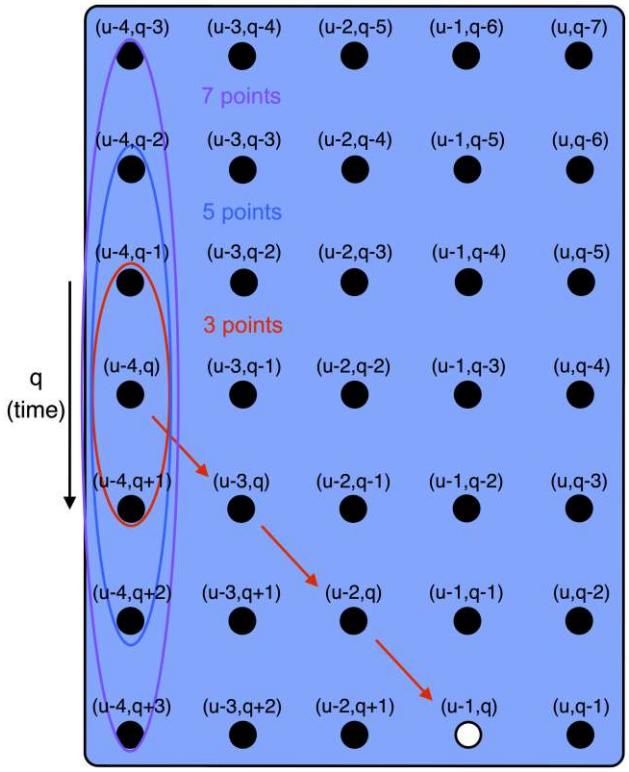

Figure 3.10: *Different GVD-implementations using three, five, and seven points for the central finite difference formula. The coefficients were shifted towards the minus u-axis until parallel computing was possible. In addition, for the first three spatial points, the GVD-term was set to zero. The white marked point indicates the development point.*

overall unstable behavior. In case the polarization elimination is not applied, this unstable behavior would cause lasing operation at $\Delta f = f_s/2$ since the medium is transparent at these spectral regions.

Stability analysis

In chapter 1, the stability criterion was introduced by the von Neumann analysis for two-level implementations. By changing the coordinate system from space and time (z,t) to the propagation axis and time (u,t), a similar analysis can be conducted. To obtain a two-level implementation, the losses are shifted towards the minus u-axis to the same extent as the GVD implementation. This facilitates the stability analysis drastically. By implementing the losses on a different discretization point than on the central point of the GVD-term, the stability analysis of multi-level implementations would have to be carried out. This analysis, as discussed in [36, Ch. 6], would go beyond the scope of this work. In this section, a two-level stability analysis is applied to extract a general statement for the experimental study of stability.

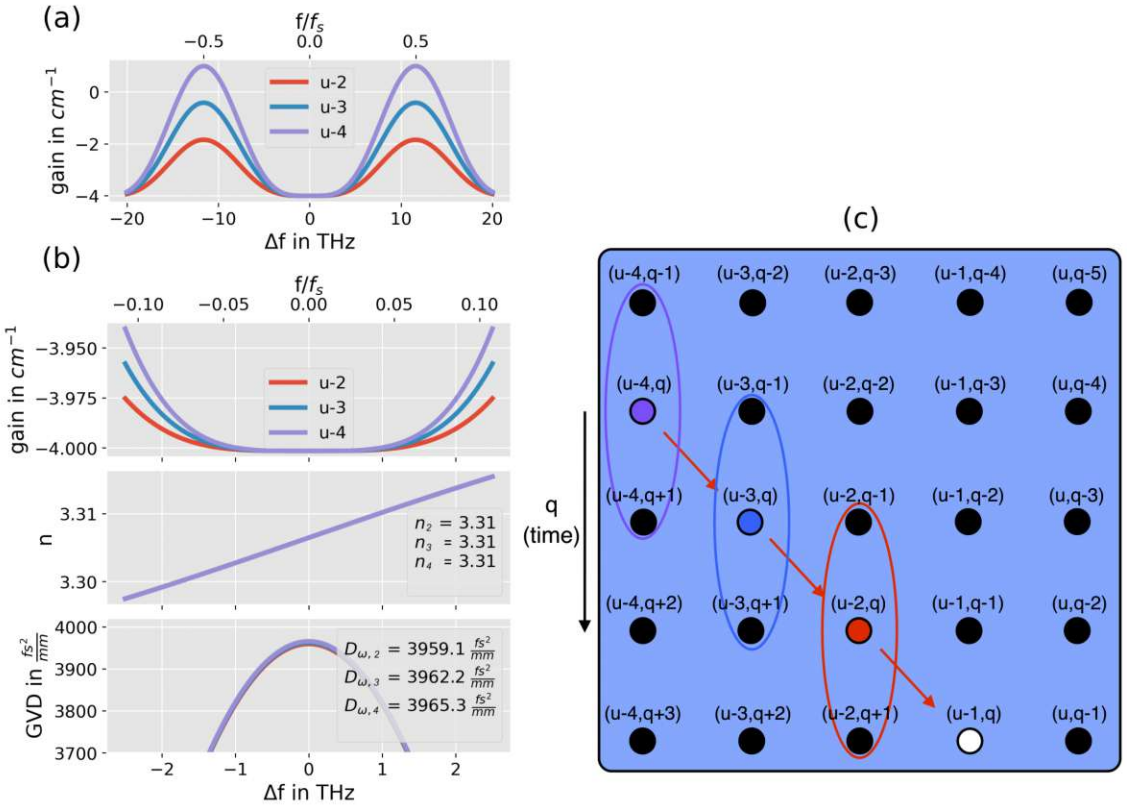

Figure 3.11: *Different central GVD-implementations by shifting the coefficients towards the minus u-axis. a) depicts a broadband simulation, b) a narrow-band simulation, and c) displays the different implementations. For the first three spatial points, the GVD-term was set to zero. The white marked point indicates the development point. Simulation parameters:* $L = 1mm$, $N = 257$, $\alpha = 4cm^{-1}$ *and* $D_\omega = 4000fs^2/mm$.

By considering the implementation utilizing two u-levels[5],

$$E^{u,q} = \underbrace{e^{-\alpha\Delta z} \cdot E^{u-2,q}}_{losses} + \underbrace{j2F\Big(E^{u-2,q+1} - 2E^{u-2,q} + E^{u-2,q-1}\Big)}_{GVD}, \tag{3.39}$$

and by applying the temporal Fourier-transformation, one obtains

$$\frac{E(\Delta f)^u}{E(\Delta f)^{u-2}} = e^{-\alpha\Delta u} \cdot + j2F\Big(e^{j2\pi\Delta f\Delta t} - 2 + e^{-j2\pi\Delta f\Delta t}\Big). \tag{3.40}$$

The stability criterion is given by

$$\left|\frac{E(\Delta f)^u}{E(\Delta f)^{u-2}}\right| \leq 1 \tag{3.41}$$

[5] The contributions of the losses and the GVD have to be doubled since (u,q) is calculated by (u-2,q) instead of (u-1,q).

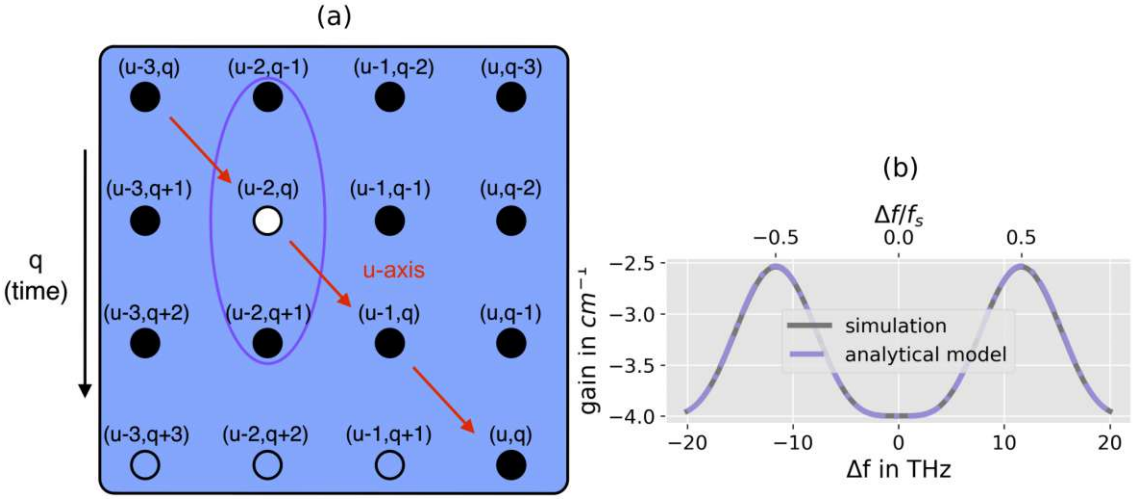

Figure 3.12: *Stability analysis demonstrated by the implementation of a two level system in the u-t coordinate system depicted in a). Fig. b) compares the simulation with the analytical approach (equation 3.43). For the first spatial point, the GVD-term was set to zero, and a one-level implementation was applied for the implementation of the losses. The white marked point indicates the development point. Simulation parameters:* $L = 1mm$, $N = 257$, $\alpha = 4cm^{-1}$ *and* $D_\omega = 4000fs^2/mm$.

which states, that the GVD-term should not induce gain.
In case of the discussed two-level system, the amplification factor is given by

$$|g(\Delta f)| = \sqrt{\underbrace{e^{-2\alpha\Delta z}}_{\approx 1} + \underbrace{\left[4F \cdot \left(cos(2\pi\Delta f\Delta t) - 1\right)\right]^2}_{>0}}. \tag{3.42}$$

Hence, the implementation is unstable if the losses are small.
By taking the quadratic amplification term, the two peaks in the gain profile can be justified. This yields

$$\frac{I(\Delta f)^u}{I(\Delta f)^{u-2}} = \underbrace{e^{-\frac{9}{4}\alpha\Delta u}}_{\text{constant}} + \underbrace{16F^2 \cdot \left[cos(2\pi\Delta f\Delta t)^2 - 2cos(2\pi\Delta f\Delta t) + 1)\right]^2}_{\text{frequency dependent}} \tag{3.43}$$

and is depicted in Figure 3.12 together with the corresponding simulation. As shown, the simulation coincides well with the derived expression.

To summarize the results, the finite difference implementation of the GVD is inherently unstable leading to gain peaks at $|\Delta f| = f_s/2$. Higher-order methods increase the accuracy of the solution but elevate the undesired gain peaks. The back-shifting process required to implement central difference coefficients aggravates the stability problem further. The next section discusses possible solutions to overcome this problem to obtain a stable implementation. This step is essential for the simulation of broadband lasers where the polarization elimination of the gain profile is not applied. In this case, the gain implementation does not stabilize the GVD implementation with its artificial losses.

Stable implementation

As shown previously, the unstable behavior of the finite difference implementation of the wave-equation, including losses and GVD, is directly connected to equation 3.31 being implemented. In order to obtain a stable scheme, the equation has to be modified. This means the mathematical description has to be adapted while retaining the underlying physics. First, equation 3.31 can be split up into a phase Φ and amplitude A by using the relation $E = A \cdot e^{j\Phi}$. This leads to

$$\frac{n}{c_0}\frac{\partial A}{\partial t} + \frac{\partial A}{\partial z} = -\frac{\alpha}{2}A - \frac{D_\omega}{2}\Big[A\frac{\partial^2 \Phi}{\partial^2 t} + 2\frac{\partial A}{\partial t}\frac{\partial \Phi}{\partial t}\Big] \tag{3.44}$$

$$\frac{n}{c_0}\frac{\partial \Phi}{\partial t} + \frac{\partial \Phi}{\partial z} = \frac{D_\omega}{2}\Big[\frac{1}{A}\frac{\partial^2 A}{\partial^2 t} - \Big(\frac{\partial \Phi}{\partial t}\Big)^2\Big] \tag{3.45}$$

as shown in [24, p. 53]. As explained previously, the GVD acts as a phase filter in the frequency domain. Hence, one would expect that the GVD does not impact the Fourier-transformation of the amplitude equation. The above expression may potentially solve the stability issue. However, in comparison to equation 3.31, the problem has increased significantly in complexity. The problem is described by two coupled PDE. In addition, the phase equation is of nonlinear type, which further complicates the numerical treatment.

An alternative to this complex rewriting process is given by the Fourier-transformation of equation 3.31. First, the coordinate system is changed from space and time (z,t) to propagation axis and time (u,t). By conducting a Laplace-transformation, one obtains[6]

$$E(u_0, s) = E(u_0 - \Delta u, s) \cdot e^{-\frac{\alpha}{2}\cdot\Delta u} \cdot e^{j\frac{1}{2}D_\omega \Delta u \cdot s^2}. \tag{3.47}$$

In the frequency domain, the inclusion of losses and group velocity dispersion, representing the linear part of the equation, is straightforward. However, the equation does not only include linear terms. The *split step Fourier* method represents an ingenious technique to implement such equations numerically [50]. This is done by splitting the calculation into two steps. In the first step, the linear part is implemented by utilizing the Fourier-Transformation and by setting the nonlinear contribution to zero. In the second step, the linear part is neglected, and the nonlinear contribution is considered. That means, in the first step, the equation is brought into the frequency domain and the linear part is being implemented. In the second step, the inverse Fourier-Transformation is applied, and the contribution of the nonlinear part is considered. Since group velocity dispersion is taken into account in the frequency domain, stability should not cause any difficulties. The split-step method may implement the equation in a very accurate way. However, the

[6] The obtained equation is equal to 3.30 by omitting $e^{-j\frac{N}{c_0}\Delta\omega\Delta z}$, which is taken into consideration by the different coordinate system and the approximation of $N \approx n$.
By conducting a first-order Taylor-expansion of 3.47 and the inverse Fourier-Transformation, one obtains

$$\frac{E(u_0 + \Delta u, t_0) - E(u_0, t_0)}{\Delta u} = -\frac{\alpha}{2} \cdot E(u_0, t_0) + j\frac{1}{2}D_\omega \frac{\partial^2 E(u_0, t_0)}{t^2}. \tag{3.46}$$

which is an approximation of 3.31.

necessary transformations may cause very long calculation times, which is an unwanted property. For this reason, the split-step method cannot be used to realize the equation numerically.

The implementation of the losses was improved by including higher-order terms in the implementation. The GVD-implementation will be enhanced in a similar way. By starting with equation 3.47 and conducting a Taylor-expansion of the GVD-term, one obtains

$$E(u_0,s) = \underbrace{E(u_0-\Delta u,s)a}_{\text{losses}} + \underbrace{a\Big[s^2b+\frac{1}{2}(s^2b)^2+\dots\Big]E(u_0-\Delta u,s)}_{\text{GVD}} \tag{3.48}$$

by splitting the losses and the GVD-part of the equation. Here, $a = e^{-\frac{\alpha}{2}\cdot\Delta u}$, $b = j\frac{D_\omega}{2}\Delta u$, and $s = j\Delta\omega$.
The GVD part can be readily shifted towards the minus u-axis by a substitution of the upper equation shifted to $u_0 - \Delta u$ into $E(u_0 - \Delta u, s)$ of the GVD-part. This yields

$$E(u_0,s) = E(u_0-\Delta u,s)\cdot a + a^2\Big[bs^2+\frac{3}{2}(bs^2)^2\dots\Big]E(u_0-2\cdot\Delta u,s). \tag{3.49}$$

Before the procedure is continued, the order of the GVD-implementation should be discussed. As outlined previously, higher-order finite difference coefficients increase the accuracy of the implementation. However, higher-order central schemes have to be shifted further towards the minus u-axis which complicates the implementation and the error made. The advantages and disadvantages of the higher-order schemes are well-balanced in case of the five-point central version. The discussion will therefore be limited to the five-point GVD-implementation.

In order to implement the central five-point scheme, introduced in section 3.4.2, the GVD-part has to be shifted once more and one obtains

$$E(u_0,s) = \underbrace{E(u_0-\Delta u,s)a}_{\text{losses}} + \underbrace{a^3bs^2E(u_0-3\Delta u,s)}_{\text{first-order GVD-term}} + \underbrace{a^3\Big[\frac{5}{2}(bs^2)^2+\dots\Big]E(u_0-3\Delta u,s)}_{\text{higher-order GVD terms}}. \tag{3.50}$$

By continuing this procedure for the higher-order terms, one obtains

$$\begin{aligned} E(u_0,s) = &\underbrace{E(u_0-\Delta u,s)\cdot a}_{\text{losses}} + \underbrace{a^3\cdot bs^2\cdot E(u_0-3\cdot\Delta u,s)}_{\text{first-order term}} \\ &+ \underbrace{a^5\Big[\frac{5}{2}(bs^2)^2\Big]E(u_0-5\cdot\Delta u,s)}_{\text{second-order term}} + \underbrace{a^7\Big[\frac{49}{6}(bs^2)^3\Big]E(u_0-7\cdot\Delta u,s)}_{\text{third-order term}} + \dots. \end{aligned} \tag{3.51}$$

The upper equation can be numerically implemented by applying the inverse Laplace-transformation and discretizing the obtained derivatives. However, this procedure does not stabilize the implementation since the schemes required for the fourth and sixth derivatives are not defined. This step is essential in obtaining a stabilizing effect since the

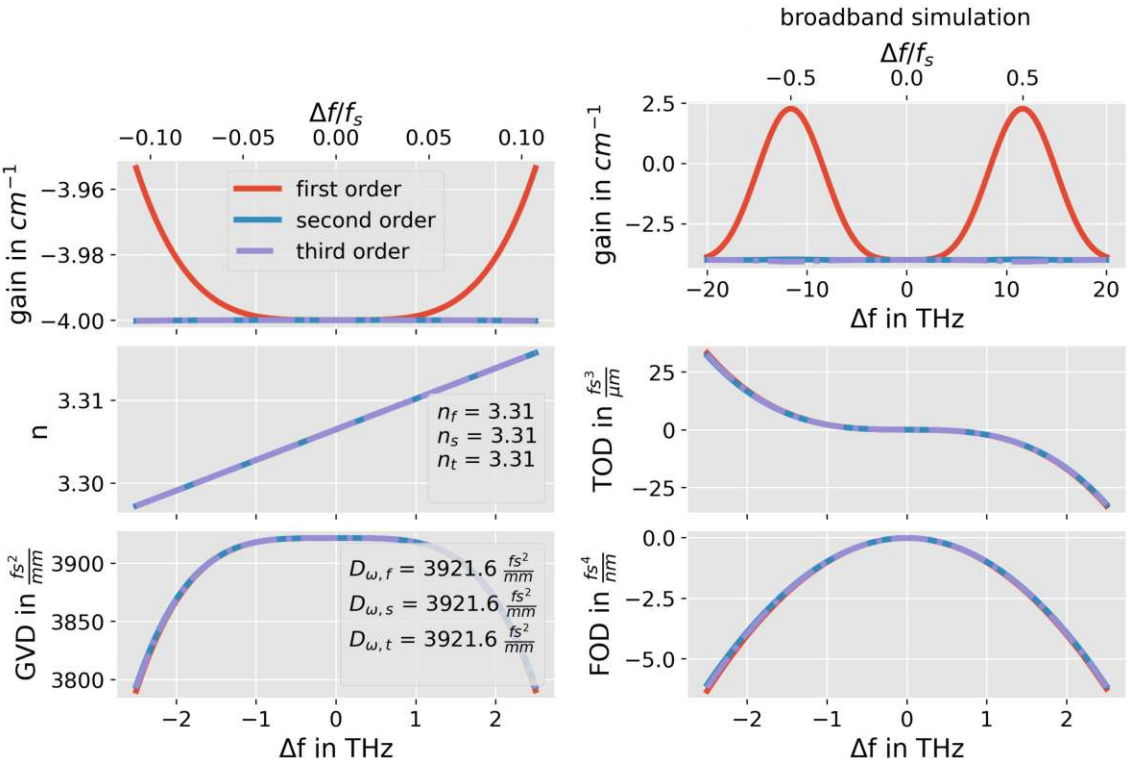

Figure 3.13: *GVD implementation by truncating the Taylor-expansion of the GVD-term after the first, second, and third-order. Simulation parameters:* $L = 1mm$, $N = 257$, $\alpha = 4cm^{-1}$ *and* $D_\omega = 4000\frac{fs^2}{mm}$.

used discretization schemes impact the gain profile. By applying the inverse Fourier-transformation ($s = j\omega$) and by replacing the derivative with the five-point central difference formula (equation 3.38) and applying the Z-transformation, one obtains

$$s^2 E \Leftrightarrow \frac{\partial^2 E}{\partial t^2} \Leftrightarrow \frac{-z^2 + 16z - 30 + 16z^{-1} - z^{-2}}{12\Delta t^2} \cdot E(z). \tag{3.52}$$

In order to implement the n-th powers of (s^2), the gray-marked term is taken to the power of n.

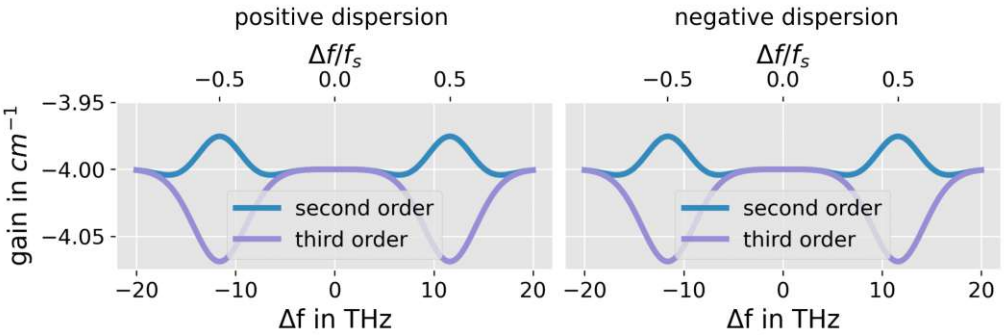

Figure 3.14: *Broadband gain simulation of the tested GVD versions which compensate the gain peaks at $\Delta f = f_s/2$ for positive and negative dispersion. Simulation parameters: $L = 1mm$, $N = 257$, and $D_\omega = \pm 4000 \frac{fs^2}{mm}$.*

In case of the implemented version, this yields

$$E(u_0, z) = \underbrace{a \cdot E(u_0 - \Delta u, z)}_{\text{losses}} + \underbrace{jFa^3 \cdot \frac{z^2 + 16z - 30 + 16z^{-1} - z^{-1}}{12} \cdot E(u_0 - 3\Delta u, z)}_{\text{first-order GVD term}} + \underbrace{a^5 \left[jF \frac{z^2 + 16z - 30 + 16z^{-1} - z^{-1}}{12} \right]^2 \cdot E(u_0 - 5\Delta u, z)}_{\text{second-order GVD term}} + \underbrace{a^7 \left[jF \frac{z^2 + 16z - 30 + 16z^{-1} - z^{-1}}{12} \right]^3 E(u_0 - 7\Delta u, z)}_{\text{third-order GVD term}} . \tag{3.53}$$

The above equation can be implemented by conducting the inverse Z-transformation. This leads to the simulation results shown in Figure 3.13. By comparing the three depicted versions, one can see that the inclusion of the second-order term reduces the gain peaks at $\Delta f = f_s/2$ almost completely. In addition, all results show a nearly identical phase profile which defines $n(\Delta f)$ and $GVD(\Delta f)$. Figure 3.14 shows the gain profile of the simulation obtained by truncating the implementation after the second and third-order terms. By comparing both Figures with different signs of dispersion, one can see that the sign has no impact on the compensated gain-peaks. Both second-order implementations show a small gain peak at $\Delta f = f_s/2$. However, its size is negligible in comparison to the losses. The third-order implementation exhibits a loss peak at $\Delta f = f_s/2$, and the graph does not exceed the losses set. That means the third-order dispersion is stable even if the losses are negligible. The implementation is, therefore, truncated after the third-order. In case a higher spectral precision is needed, the overall accuracy can be further increased by decreasing the grid step size (Δz and Δt). Figure 3.15 shows a simulation with twice the number of points. As depicted, the error made at the the boundaries of the shown spectrum is drastically reduced leading to a good approximation of the expected profiles.

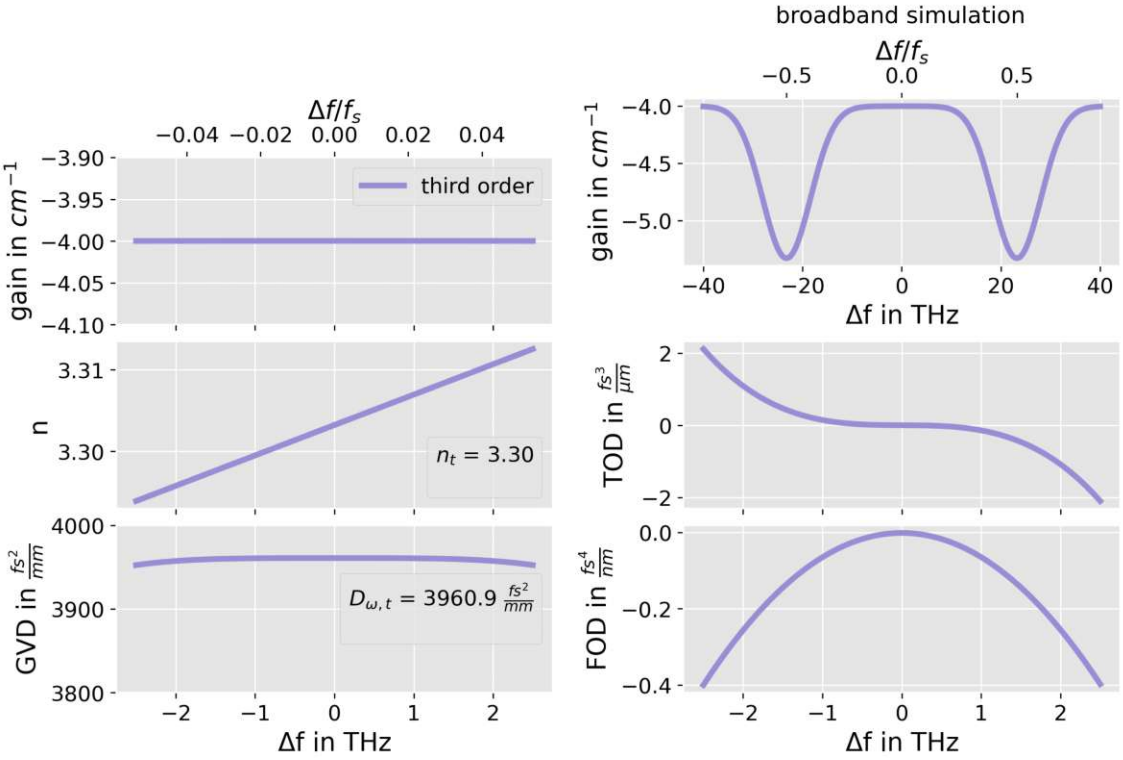

Figure 3.15: *Final GVD-implementation by truncating the development after the third-order. By increasing the number of grid points to* 513*, the error made at the boundary of the bandwidth can be reduced leading to nearly perfect results. Simulation parameters:* $L = 1mm$*,* $\alpha = 4cm^{-1}$ *and* $D_\omega = 4000\frac{fs^2}{mm}$*.*

The value of the GVD is slightly below the input value of $4000fs^2/mm$ since the first six points do not only include the GVD due to the used startup procedure.

Stabilization: working principle

In the previous section, a method was described stabilizing the GVD-implementation. It was shown that the gain peaks appearing at a frequency of one-half of the sampling frequency can be drastically minimized by conducting a Taylor-expansion of the implementation in the frequency domain and by including higher-order terms in the implementation. This section should shed light on this compensation mechanism. Similar to the stability analysis, a two-level implementation will be used to simplify the analytical description. The three point central GVD-implementation in combination with its second-order term shifted to $E^{u-3,q}$ will be used for that purpose. By solely implementing the first-order approximation, one obtains

$$\frac{E(\Delta f)^u}{E(\Delta f)^{u-3}} = e^{-\frac{3}{2}\alpha\Delta u}\left[1 + j6F \cdot (cos(2\pi\Delta f\Delta t) - 1)\right] \tag{3.54}$$

similar to equation 3.40 but with the compensation of the losses due to the back-shifting process. This leads to

$$\frac{I(\Delta f)^u}{I(\Delta f)^{u-3}} = e^{-3\alpha\Delta u} \cdot \left[1 + \left[6F \cdot (cos(2\pi\Delta f\Delta t) - 1)\right]^2\right] \tag{3.55}$$

with a frequency-dependent term causing the gain peaks at half the sampling frequency. By truncating the development after the second-order term, one obtains

$$\frac{E(\Delta f)^u}{E(\Delta f)^{u-3}} = e^{-\frac{3}{2}\alpha\Delta u}\left[1+j6F\cdot(cos(2\pi\Delta f\Delta t)-1)+\frac{1}{2}\left[j6F\cdot(cos(2\pi\Delta f\Delta t)-1)\right]^2\right] \tag{3.56}$$

leading to

$$\frac{I(\Delta f)^u}{I(\Delta f)^{u-3}} = e^{-3\alpha\Delta u} \cdot \left[1 - \left[6F(cos(2\pi\Delta f\Delta t) - 1)\right]^2 + \frac{1}{4}\left[6F(cos(2\pi\Delta f\Delta t) - 1)\right]^4 + \left[6F \cdot (cos(2\pi\Delta f\Delta t) - 1)\right]^2\right] \tag{3.57}$$

where the terms marked in red cancel each other out. This leads to a far flatter gain profile as depicted previously. A similar analysis can be carried out for the phase of the equation leading to the result that the additional term influences the phase slightly.

The explained stabilization method was also applied to higher-order one-sided methods. One-sided methods would eliminate the back-shifting process and would partially simplify the overall complexity of the implementation. However, the stabilizing effect did not take place as tested. Due to their higher-order of accuracy and the stabilizing method found, one-sided formulas were not further investigated.

3.5 Higher-order dispersion

Similar to the GVD-implementation, the analysis starts in the frequency domain. By truncating the development of Δk, introduced in section 3.4.1, after the fourth-order, one obtains

$$\Delta k \approx \frac{\partial k}{\partial \omega}\Delta\omega + \frac{1}{2}D_\omega\Delta\omega^2 + \frac{1}{3!}\cdot TOD\cdot\Delta\omega^3 + \frac{1}{4!}\cdot FOD\cdot\Delta\omega^4 \tag{3.58}$$

where the third and fourth-order dispersion coefficients are denoted as

$$TOD = \frac{\partial^3 k}{\partial\omega^3} \qquad FOD = \frac{\partial^4 k}{\partial\omega^4}. \tag{3.59}$$

In the u-t coordinate system, this yields

$$E(u_0,\Delta\omega) = E(u_0-\Delta u,\Delta\omega)e^{-\frac{\alpha}{2}\Delta u}\cdot e^{-j\frac{1}{2}D_\omega(\Delta\omega)^2\Delta u}\cdot e^{-j\frac{1}{3!}TOD(\Delta\omega)^3\Delta u}\cdot e^{-j\frac{1}{4!}FOD(\Delta\omega)^4\Delta u} \tag{3.60}$$

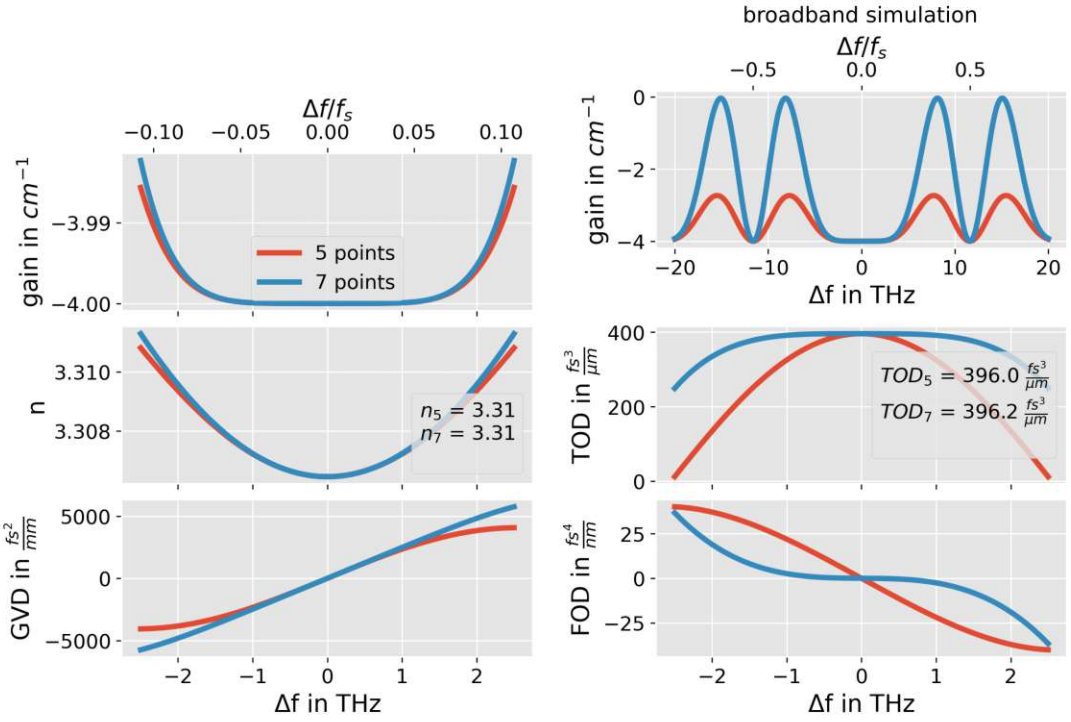

Figure 3.16: *Five and seven point TOD implementation at the central point* $(u-4,q)$*. The first three spatial steps only include losses. Simulation parameters:* $L = 1mm$*,* $N = 257$*, and* $TOD = 400\frac{fs^3}{\mu m}$*.*

which corresponds to the PDE

$$\frac{n}{c_0}\frac{\partial E}{\partial t} + \frac{\partial E}{\partial z} = -\frac{\alpha}{2}E + j\frac{1}{2}D_\omega\frac{\partial^2 E}{\partial t^2} + \frac{1}{3!}TOD\frac{\partial^3 E}{\partial t^3} - j\frac{1}{4!}FOD\frac{\partial^4 E}{\partial t^4}. \tag{3.61}$$

Similar to the implementation of the GVD, equation 3.60 will be used to implement the third (TOD) and the fourth-order dispersion (FOD) in the following subsections. First, each term will be implemented individually by setting the other two terms to zero. Finally, section 3.5.3 deals with the stability of a combination of the dispersion coefficients.

3.5.1 Third-order dispersion (TOD)

Similar to the GVD implementation, the central finite difference formula will be shifted along the minus u-axis. Figure 3.16 shows a comparison between a five and seven point TOD implementation at the central point $(u-4,q)$. The used finite difference formulas are given by

$$\frac{\partial^3 E}{\partial t^3} \Leftrightarrow E(z)\cdot\begin{cases}\frac{z^2-2z+2z^{-1}-z^{-2}}{2(\Delta t)^3} & \text{, 5 points implementation}\\ \frac{-z^3+8z^2-13z+13z^{-1}-8z^{-2}+z^{-3}}{8(\Delta t)^3} & \text{, 7 points implementation.}\end{cases} \tag{3.62}$$

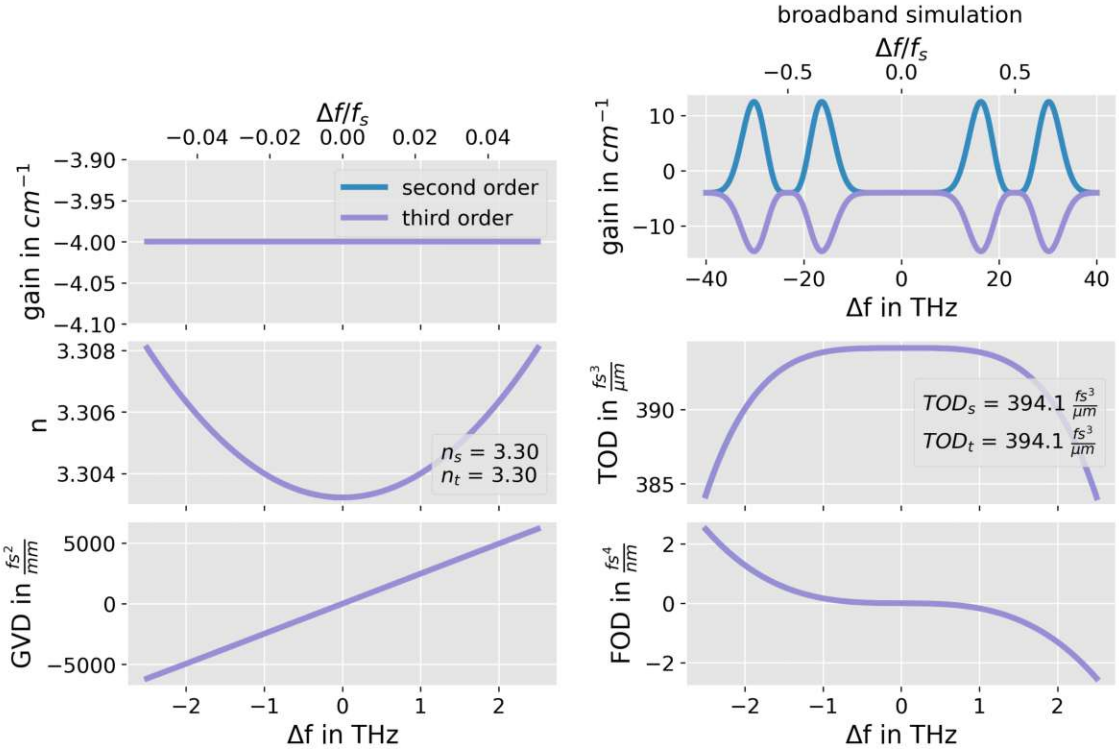

Figure 3.17: *Simulation results of truncating the TOD Taylor-expansion after the second and third-order term. The first 9 spatial steps only include losses. Simulation parameters:* $L = 1mm$, $N = 513$, $\alpha = 4cm^{-1}$, $GVD = 0\frac{fs^2}{mm}$, *and* $TOD = 400\frac{fs^3}{\mu m}$.

Since the five-point implementation deviates significantly from the expected constant TOD profile, the seven-point version will be analyzed further. Similar to the GVD, the gain profile exhibits peaks aside from the central frequency. However, in comparison to the GVD, the peaks are not located at $\Delta f = \pm f_s/2$.

To compensate the gain peaks, the Taylor-expansion of the TOD-term of equation 3.60 is used where $s = j\Delta\omega$. This yields

$$\begin{aligned} E(u_0, s) = &\underbrace{E(u_0 - \Delta u, s) \cdot a}_{\text{losses}} + \underbrace{a^4 \cdot cs^3 \cdot E(u_0 - 4 \cdot \Delta u, s)}_{\text{first-order term}} \\ &+ \underbrace{a^7 \left[\frac{7}{2}(cs^3)^2\right] E(u_0 - 7 \cdot \Delta u, s)}_{\text{second-order term}} + \underbrace{a^{10}\left[\frac{50}{3}(cs^3)^3\right] E(u_0 - 10 \cdot \Delta u, s)}_{\text{third-order term}} + \dots . \end{aligned} \tag{3.63}$$

Here $c = \frac{1}{3!} \cdot TOD \cdot \Delta u$.
To implement the above equation, the relation

$$s^3 E \Leftrightarrow \frac{\partial^3 E}{\partial t^3} \Leftrightarrow \frac{-z^3 + 8z^2 - 13z + 13z^{-1} - 8z^{-2} + z^{-3}}{8(\Delta t)^3} \cdot E(z) \tag{3.64}$$

was used, and the higher powers of the term marked in gray, similar to the implementation of the GVD. Figure 3.17 shows the simulation result of truncating the development after the second and third-order term for $N = 513$. Similar to the GVD-implementation, the second-order approximation is not sufficient for a stable implementation as depicted in Figure 3.17. The broadband gain profile is not influenced by the sign of TOD. Hence, the implementation is stable.

3.5.2 Fourth-order dispersion (FOD)

Similar to the TOD, a seven point implementation will be used for the implementation. Based on the Taylor-expansion of the FOD-term in equation 3.61, one obtains

$$\begin{aligned} E(u_0, s) = &\underbrace{E(u_0 - \Delta u, s) \cdot a}_{\text{losses}} + \underbrace{a^4 \cdot ds^4 \cdot E(u_0 - 4 \cdot \Delta u, s)}_{\text{first-order term}} \\ &+ \underbrace{a^7 \Big[\frac{7}{2}(ds^4)^2\Big] E(u_0 - 7 \cdot \Delta u, s)}_{\text{second-order term}} + \underbrace{a^{10} \Big[\frac{50}{3}(ds^4)^3\Big] E(u_0 - 10 \cdot \Delta u, s)}_{\text{third-order term}} + \dots, \end{aligned} \tag{3.65}$$

where $d = -\frac{1}{4!} \cdot FOD \cdot \Delta u$.
The above equation was implemented by means of the relation

$$s^4 E \Leftrightarrow \frac{\partial^4 E}{\partial t^4} \Leftrightarrow \frac{-z^3 + 12z^2 - 39z + 56 - 39z^{-1} + 12z^{-2} - z^{-3}}{6(\Delta t)^4} \cdot E(z). \tag{3.66}$$

Similar to the implementations of GVD and TOD, the second and third-order terms were calculated by the higher power of the term marked in gray. Figure 3.18 shows the simulation result with 257 points. While the second-order realization exhibits a gain peak at $|\Delta f| = f_s/2$, the third-order implementation shows elevated losses at these frequencies. Therefore, the third-order version is considered as stable for the set of parameters.

However, by increasing the number of points to 513, the implementation becomes unstable. A possible reason for this is found in equation 3.57. The magnitude of the remaining frequency-dependent part of the equation is proportional to $1/\Delta z$. Thus, by decreasing the grid spacing, the impact of the remaining frequency-dependent term increases. This can be readily seen by comparing the broadband simulation depicted in Figure 3.15 with the positive dispersion simulation shown in Figure 3.14. The large number of temporal points used for the implementation and the decreasing spatial grid increasing the error term may lead to a numerical problem. Due to rounding errors, for instance, the solution is not perfectly compensated which could lead to an unstable behavior. This problem can be potentially avoided for narrow-band calculations by using fewer temporal points for the FOD-implementation or by increasing the number of decimal points.

3.5.3 Multi-parameter stability

In the implementations of the GVD, TOD, and FOD, only one dispersion coefficient was considered while the others were set to zero. This development stabilizes the case where

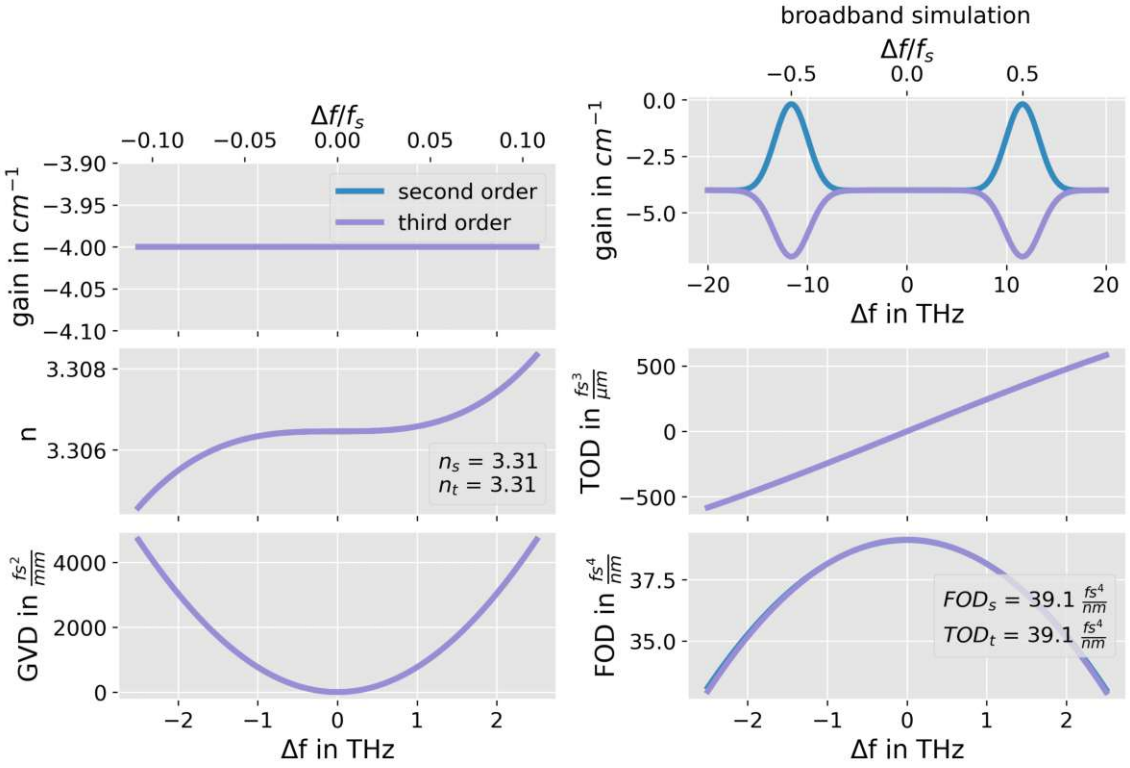

Figure 3.18: *Simulation results of the FOD implementation by truncating the development after the second and third-order term. Simulation parameters:* $L = 1mm$, $N = 257$, $\alpha = 4cm^{-1}$, $GVD = 0\frac{fs^2}{mm}$, $TOD = 0\frac{fs^3}{\mu m}$, *and* $FOD = 40\frac{fs^4}{nm}$.

only one coefficient is set but not their combined use. This section addresses this problem and describes a strategy to stabilize the joint use of the GVD and the TOD. The described principle can be readily extended to allow a combined use of all three dispersion parameters.

Similar to the previous implementation, 3.60 is approximated. By considering GVD and TOD, the Taylor-expansion of

$$E(u_0, s) = E(u_0 - s, \Delta\omega) \cdot e^{-\frac{\alpha}{2}\cdot\Delta u} \cdot e^{j\frac{1}{2}D_\omega \Delta u \cdot s^2} \cdot e^{\frac{1}{3!}TOD\Delta u \cdot s^3}. \tag{3.67}$$

yields

$$\begin{aligned} E(u_0, \Delta\omega) = {} & E(u_0 - \Delta\omega, \Delta\omega) \cdot a \\ & + E(u_0 - \Delta\omega, \Delta\omega) \cdot a \Big[(cs^3 + \frac{(cs^3)^2}{2} \dots) + (bs^2 + \frac{(bs^2)^2}{2} \dots) \\ & + (bs^2 + \frac{(bs^2)^2}{2} \dots) \cdot (cs^3 + \frac{(cs^3)^2}{2} \dots) \Big] \end{aligned} \tag{3.68}$$

with the additional cross-terms marked in gray.

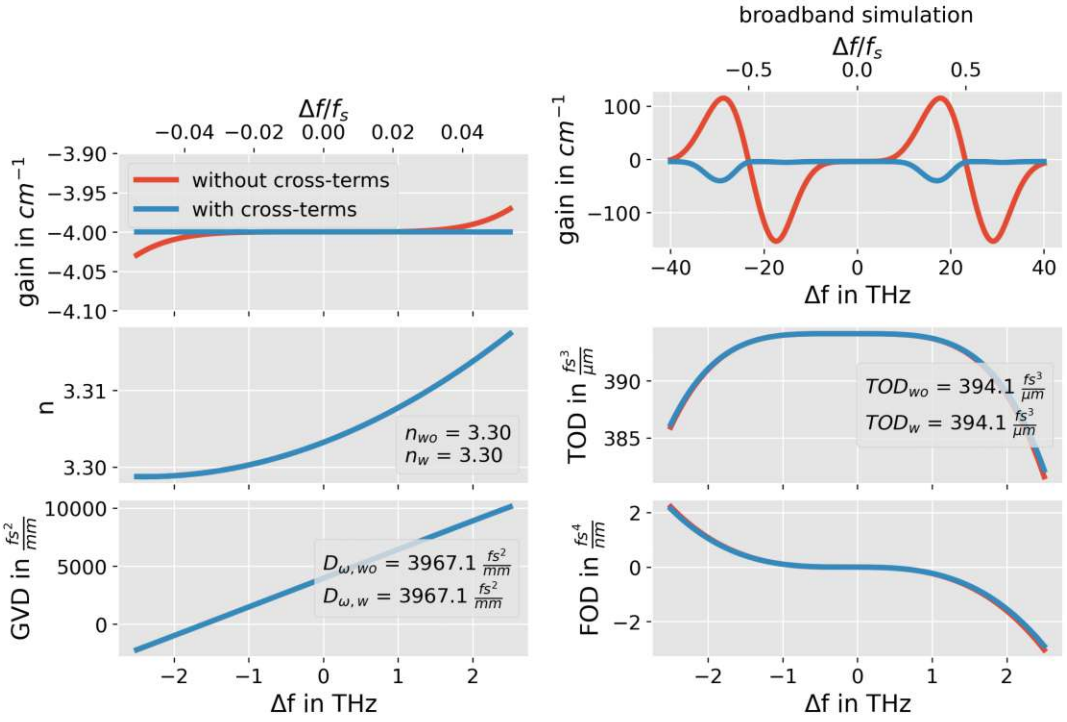

Figure 3.19: *Simulation results when setting GVD and TOD with and without additional cross terms. Simulation parameters:* $L = 1mm$, $N = 513$, $D_\omega = 4000\frac{fs^2}{mm}$, *and* $TOD = 400\frac{fs^3}{\mu m}$.

In the exact same way as before, the equation is used to shift the dispersion terms towards the minus u-axis to enable a central implementation. This yields the following approximation

$$E(u_0,s) = E(u_0,s)_{\text{losses}} + E(u_0,s)_{\text{GVD}} + E(u_0,s)_{\text{TOD}} + \underbrace{6a^6 \cdot bs^2 \cdot cs^3 \cdot E(u_0 - 6\cdot\Delta u, s)}_{\text{first cross-term}} + \underbrace{a^8\left[32(bs^2)^2 cs^3\right]E(u_0 - 8\cdot\Delta u, s)}_{\text{second cross-term}} + \underbrace{a^9\left[\frac{81}{2}(cs^3)^2 bs^2\right]E(u_0 - 9\cdot\Delta u, s)}_{\text{third cross term}}. \tag{3.69}$$

By including the cross terms into the simulation, the implementation is stable as shown in Figure 3.19. Without the cross terms, the broadband gain simulation exhibits a large gain peak. By including the additional terms, the GVD and TOD only generate losses. The implementation was tested for all sign combinations of TOD and D_ω, whereby no combination led to additional gain.

Group velocity dispersion effects are considered as phase filters and should not impact the intensity spectrum. By including these effects into the model by means of finite difference, it was shown that the discretized equation becomes inherently unstable. Three techniques were analyzed to circumvent this problem: (1) splitting the equation into phase and amplitude, (2) utilizing the split-step technique, and (3) implementing the equation in the Laplace domain by conducting a Taylor approximation and by utilizing the relations between the Laplace-transformation and the time domain. While the splitting process imposes further numerical complications, the split-step technique induces long computation times, the realization in the Fourier-domain leads to a stabilizing effect by including higher-order terms. However, the stabilizing effect only takes place by using central finite difference coefficients as tested. Hence, the implementation had to be shifted towards the minus u-axis to avoid a coupling of the equations. This is essential, as otherwise the performance of the implementation would decrease significantly since parallel computing would not be possible.

3.6 Gain

Similar to the previous section, the wave-equation is expanded once more to include the gain of the laser medium. However, in comparison to the previous extensions, the additional term is coupled with an additional equation: *the polarization equation*. This is necessary since the gain of the master-equation for fast gain media induces losses above and below the center frequency as introduced. The wave-equation including losses, GVD, TOD, FOD, and the gain (marked in gray) reads

$$\frac{\partial E_+}{\partial u} = \underbrace{-\frac{\alpha}{2}E_+}_{\text{losses}} + \underbrace{j\frac{D_\omega}{2}\frac{\partial^2 E_+}{\partial t^2} + \frac{TOD}{3!}\frac{\partial^3 E_+}{\partial t^3} - j\frac{FOD}{4!}\frac{\partial^4 E_+}{\partial t^4}}_{\text{dispersion effects}} \underbrace{- j\frac{\Gamma\mu\omega_0}{n\epsilon_0 c L_p}\sigma_+}_{\text{gain}}, \tag{3.70}$$

where Γ is the confinement factor, μ is the dipole matrix element, $\omega_0 = 2\pi f_0$, L_p is the period length, ϵ_0 is the permittivity of vacuum. σ_+ is the right propagating envelope of the off-diagonal element of the density matrix referred to as polarization. The polarization equation is given by

$$\frac{\partial \sigma_+}{\partial t} = -\frac{\sigma_+}{T_2} + j\frac{\mu}{2\hbar}\cdot\left[E_+ n_0 + E_- n_2^{(*)}\right], \tag{3.71}$$

where T_2 is the dephasing time and E_- is the left propagating envelope of the electric field. As the equation also contains the counter-propagating parts (e.g. E_-), the simplified notation $E = E_+$ used up to now is no longer applicable.
The equation for the polarization σ_+ is coupled to the equation for spatially constant n_0 and the spatially varying upper level population n_2, given by

$$\frac{\partial n_0}{\partial t} = J - \frac{n_0}{T_1} + \frac{\mu}{\hbar}\cdot\Im\{E_+\sigma_+^* + E_-\sigma_-^*\} \tag{3.72}$$

and

$$\frac{\partial n_2}{\partial t} = -\frac{n_2}{T_g} + j\frac{\mu}{2\hbar}\cdot\left(E_+\sigma_-^* - E_-^*\sigma_+\right). \tag{3.73}$$

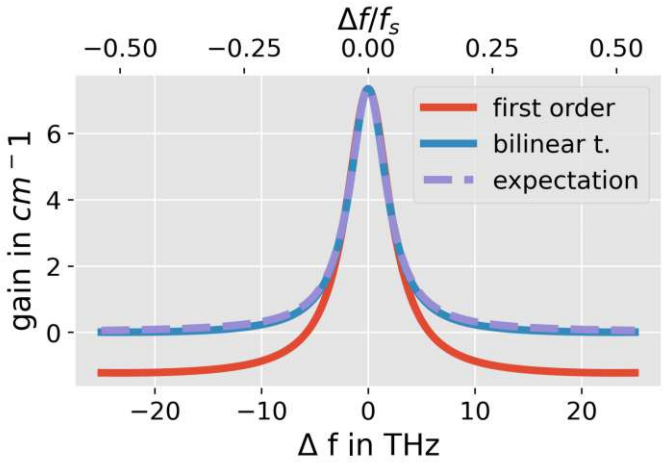

Figure 3.20: *Simulation results by implementing the polarization equation by a first-order approach (red, previously used) and by utilizing the bilinear transformation (blue). The expected behavior (purple) was calculated by the Fourier-transformation of the polarization equation and by adjusting its peak size to the simulation results. Simulation parameters:* $L = 1mm$, $N = 513$, *dispersion coefficients, and losses were set to zero.*

with the lifetimes T_1 and T_g for n_0 and n_2 respectively. In other words, T_g represents the lifetime of the spatially varying population due to SHB and is thus lowered by the carrier diffusion and T_1 can be seen as the gain recovery time. The shown equations for the gain of the right propagating envelope of the electric field E_+ can be readily derived from the Maxwell-Bloch equations, given in [24, eq. 3.55 - 3.62], by assuming that the lower lasing level is empty. In a similar way, the equation for E_- can be derived as shown in [24, Ch. 3].

3.6.1 Implementation of the gain

In the previous work from N. Opačak, a discretized model, which implements the upper equations has already been implemented. The content of this section analyzes the accuracy of this implementation and increases its order for the simulation of broadband laser sources. In the work conducted by N. Opačak, the equations for the polarization σ_+, and the equations for the population n_0 and n_2 were implemented by using an explicit scheme implemented by first-order finite difference formulas.

For the polarization equation, this first-order implementation results in

$$\sigma_+^{q+1} = \sigma_+^q \cdot \left[1 - \frac{\Delta t}{T_2}\right] + Q \cdot \Delta t \tag{3.74}$$

where $Q = j\frac{\mu}{2\hbar} \cdot \left[E_+^q n_{u0}^{q+1}\right]$ by setting E_- to zero[7].

[7] The current waveguide operates as optical amplifier where the reflectivity of the facets was set to zero. Within the variable Q, N. Opačak used n_{u0}^{q+1}. n_{u0}^q would be correct since the scheme is developed around the temporal point q.

By implementing the upper equation into the simulation and adding the additional term to the discretized version of the wave-equation, one obtains the simulation result shown in Figure 3.20. One can see clearly that the first-order version, displayed in red, deviates clearly from the expected profile calculated by a Fourier-transformation of the polarization equation 3.71 (dashed in purple). The first-order implementation induces losses above and below the center frequency. Hence, the implementation does not reflect the physical meaning correctly.

To analyze this mismatch, the Z-transformation is applied to 3.74, yielding to

$$\sigma_+(z) = \frac{Q \cdot \Delta t}{z - 1 + \frac{\Delta t}{T_2}}. \tag{3.75}$$

The upper equation has a pole at $z = 1 - \frac{\Delta t}{T_2}$ and a zero at $z \to \pm\inf$.
By taking the relation between the Z-transformation and the time discrete Fourier- transformation into account[8], $z = e^{j2\pi\Delta f \Delta t}$, it becomes apparent that a zero at $z = -1$ (the point where $|\Delta f| = f_s/2$) is necessary to reduce the amount of numerical gain or losses above and below the center frequency.

A possible solution is presented by applying the *bilinear Z-transformation* connecting the z-space and the s-space (Laplace-space). This transformation is given by

$$s = \frac{2}{\Delta t}\frac{z-1}{z+1} \tag{3.76}$$

as defined in [45, eq. 6.57]. By applying this formula to the Laplace-transformed version of 3.71, one yields

$$\sigma_+^{q+1} - \sigma_+^q = -\frac{\Delta t}{2T_2}\left(\sigma_+^{q+1} + \sigma_+^q\right) + \frac{\Delta t}{2}\left(Q^{q+1} + Q^q\right). \tag{3.77}$$

We note that this transformation leads to an implicit scheme that is developed around the point in the center between the new and the old time step.
By applying the Z-transformation to the upper equation, one gets

$$\sigma(z) = \frac{Q(z)\frac{\Delta t}{2}(z+1)}{z - 1 + \frac{\Delta t}{2T_2}(z+1)} \tag{3.78}$$

which contains a zero at $z = -1$ (maximum frequency). Hence, the implementation should neither impose gain nor losses at this point.

To implement the scheme derived by the bilinear transformation, one requires Q^{q+1}. As Q^{q+1} contains E^{q+1}, the term couples the discrete wave-equation and the polarization equation. By rewriting the discrete wave-equation as

$$E_+^{q+1} = \sigma_+^{q+1} + \zeta \tag{3.79}$$

[8] This becomes clear by comparing the definitions of both transformations and the time continuous Fourier-transformation given in [45, Ch. A]

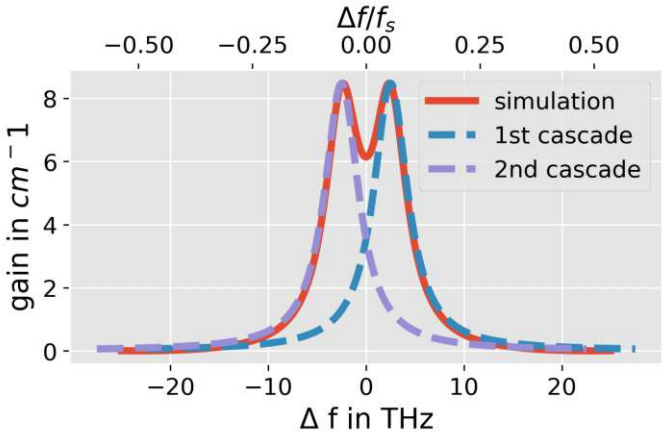

Figure 3.21: *Simulation results by implementing two shifted versions of the polarization equation. The gain peak was shifted by $\pm 2.5THz$ about the center frequency. The gain peaks of the different cascades (blue and purple) were calculated by the Fourier-transformation of the polarization equation and by adjusting their peak size to the simulation result and by shifting their center frequencies in accordance with the simulation.*

where ζ represents the other contributions like losses, GVD, TOD, or FOD [9]. By solving 3.79 in combination with 3.77, one obtains

$$\sigma_+^{q+1} = \frac{\sigma_+^q \left[2 - \frac{\Delta t}{T_2}\right] + j\Delta t \frac{\mu}{2\hbar} \zeta n_{u0}^{q+1} + Q^q \Delta t}{2 + \frac{\Delta t}{T_2} - j\Delta t \frac{\mu}{2\hbar} n_{u0}^{q+1}}. \tag{3.80}$$

By implementing the upper equation, one yields the simulation result shown in Figure 3.20, which approximates the expected behavior nearly perfectly. In comparison to the first-order approach, the version derived by the bilinear-transformation features a zero at $z = -1$, which induces a transparent behavior of the gain medium at $|\Delta f| = f_s/2$. The derived implementation can be readily expanded to include E_- to simulate the behavior of a laser.

3.6.2 Multiple gain peaks

To enable the simulation of a heterogeneous QCL, as presented in [20–22], consisting of different cascades leading to multiple gain peaks, the polarization is implemented a second time. By conducting a Laplace-transformation of the polarization equation 3.71, one obtains

$$s_1 \sigma_+(s_1) = \sigma_+ \frac{\sigma_+(s_1)}{T_2} + Q(s_1). \tag{3.81}$$

The upper equation can be readily shifted in the frequency domain by setting $s_1 = s + s_0$ where $s_0 = j2\pi f_d$. f_d is the deviation of the center frequency of the gain peak to the center frequency of the simulation. By applying the bilinear transformation to the above

[9] The additional propagation index u of the wave-equation was omitted to simplify the expressions,

equation and by solving the equation in combination with the discrete wave-equation, one yields the implementation for the shifted version

$$\sigma_+^{q+1} = \frac{\sigma_+^q \left[2 - \frac{\Delta t}{T_2} + \Delta t s_0\right] + j\Delta t \frac{\mu}{2\hbar} \zeta n_{u0}^{q+1} + Q^q \Delta t}{2 + \frac{\Delta t}{T_2} - j\Delta t \frac{\mu}{2\hbar} n_{u0}^{q+1} - s_0 \Delta t}. \tag{3.82}$$

By assuming that the different cascade designs do not significantly change the parameters of the equations of the upper-level population n_0 and n_2, multiple gain peaks can be readily implemented by the summation of multiple polarizations shifted spectrally.

Figure 3.21 shows such a simulation for two different cascade structures which are shifted from the center frequency by $\pm 2.5THz$. One can clearly see that both gain peaks overlap close to the central frequency expanding the overall bandwidth of the gain.

The gain of the laser medium was implemented by means of a simplified version of the Maxwell-Bloch equations. The equations for the spatially static n_0 and spatially varying population n_2 were implemented by using a first-order explicit scheme. The polarization equation can not be implemented by a first-order formalism, even if the equations have a similar structure. A first-order implementation would impose losses at frequencies above and below the center frequency. To overcome this issue, a scheme is required where the Z-transformed implementation exhibits a zero at $z = -1$. Such an implementation is found by using the bilinear-transformation connecting the Laplace-transformation with the Z-transformation of the implementation of the equation. The description can be further expanded to simulate multiple different cascades amplifying light at different frequencies. This is achieved by implementing multiple polarization equations shifted in the frequency domain.

CHAPTER 4

CHIRP ENGINEERING IN OPTICAL FREQUENCY COMBS

Quantum cascade lasers (QCLs) are semiconductor lasers emitting light in the infrared and terahertz spectral region. Under certain conditions, these QCLs generate optical frequency combs (OFCs), which are the topic of this chapter. OFCs are devices emitting a spectrum with equidistantly spaced modes, similar to a ruler in the frequency domain, with defined phase relations [31].

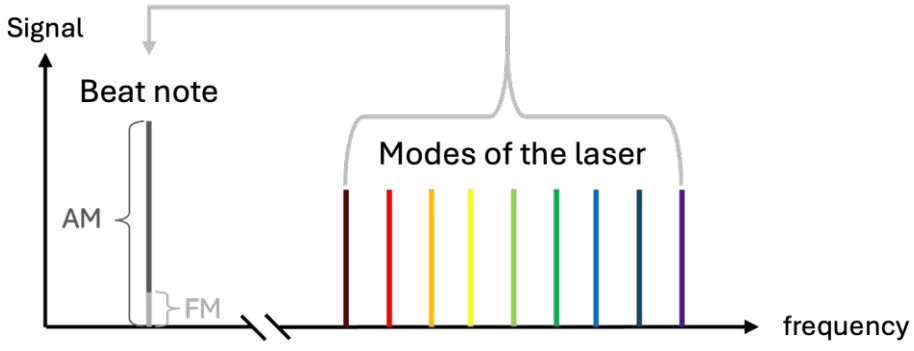

Figure 4.1: *Schematic drawing of the laser modes and resulting beat note for FM-type and AM-type OFCs.*

In general, most OFCs can be categorized into two different groups: *frequency-modulated (FM-type)* and *amplitude-modulated (AM-type)* OFCs [51]. Both types can be distinguished by the magnitude of the laser beat note formed by the superposition of all intermodal beating signals. After the formation of the OFC, the laser beat note features a narrow bandwidth indicating equidistant laser modes. The magnitude of this beat note is determined by the phase relation of the modes. In the case of equal phases (in-phase synchronized state, AM-type), the intermodal beatings interfere constructively, resulting in a strong beat note. This is in sharp contrast to the phases of FM-comb modes, which are, for instance, uniformly distributed around the unit circle (anti-phase synchronized state, FM-type) leading to a suppressed beat note. This contrast is illustrated in Figure 4.1.

Both types of combs emit a periodic intensity signal in the temporal domain. However, the shape of the signal is defined by the phase relation of the modes. While AM-combs emit pulses, frequency-modulated combs generate a signal with almost constant intensity [51]. Another distinction can be found in their condition of formation. AM-type mode-locked lasers require active or passive means to trigger the mode-locking process and the formation of pulses [5, Ch. 16.4],[51]. FM-combs, formed with QCLs, are self-starting and require no additional means to trigger the locking process [31].

Since most FM-combs are based on semiconductor materials, the discussion is limited to this type of OFC [51]. Their self-starting probability and the linearly chirped output signal were investigated in [31]. Section 4.1 describes important properties of FM-comb. After discussing their main characteristics and their working principle, the topic of chirp engineering is introduced by means of the reduced model (section 4.2). This simplified model reveals much information regarding the tunability of the locked state by changing the spatial intensity profile of the laser. These shaping mechanisms are discussed in section 4.3 and the possible applications are outlined in section 4.4.
The basis of this chapter is laid out by "Frequency comb spectral engineering in semiconductor lasers by intracavity spatial intensity profile shaping" [52]. Unless otherwise specified, all the simulations shown in this chapter were calculated by using the master equation for fast gain media given in [31]. The used simulation parameters are listed in chapter A.

4.1 FM-combs in fast gain media resonators

The laser modes of a Fabry-Pérot resonator are ideally equidistantly spaced in the frequency domain. Depending on the length L and the refractive index n, the cold cavity resonance frequencies ω_i ($i \in \mathbb{N}$), are given by

$$\omega_i = i\pi \frac{c_0}{nL} \tag{4.1}$$

as defined in [24, Ch. 5].
Since the refractive index in dispersive media is a function of frequency, the spacing of

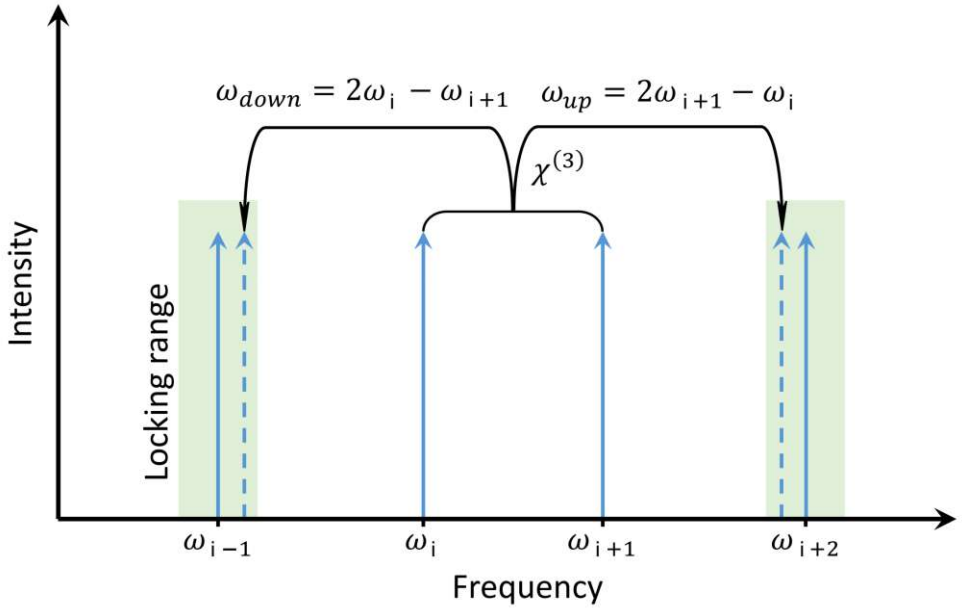

Figure 4.2: *The degenerate FWM process of two cavity modes ω_i and ω_{i+1} generates two additional frequency components (ω_{up} and ω_{down}), which are close to the cold-cavity frequencies ω_{i-1} and ω_{i-2}. Since this effect is present at all modes, the combination of degenerate FWM and frequency pulling forms an equidistant grid in the frequency domain due to energy conservation. Source: adapted from [24, Fig. 5.3]*

the modes, referred to as the *free spectral range (FSR)*[1], is not perfectly equidistant. As a result, the spectral width of the beat-note is increased, as introduced previously. The formation of amplitude-modulated OFCs in QCLs is hard to accomplish, as outlined in [24, Ch. 5]. One of the main reasons is their fast gain medium. In conventional interband lasers, the medium is capable of storing the energy in the inversion. This inversion can build up between pulses, where the intensity is zero and is dismantled abruptly when the next pulse arrives. It should be noted that normally also an interband laser favors a constant temporal intensity profile. The reason for this lies in the gain saturation of the medium and the principle of maximum emission. To produce pulses, the effect of gain saturation has to be reversed in order that the medium favors pulses [31]. In fast gain media, this is made difficult since the gain recovery time is much shorter than the round trip time [24, Ch. 5].

FM-combs based on QCLs overcome the limitations of AM-Type OFC for spectroscopy applications. They do not require any additional parts to trigger the locking process, feature many perfectly equidistant modes, and do not require that the upper state lifetime is larger than the round trip time. The reason for this perfect spacing is found in the fast gain properties of QCLs, triggering a giant third-order non-linearity [53]. This

[1] as defined in [5, p. 438].

giant non-linearity leads to an effect called *four-wave mixing (FWM)*. Since this effect is coherent, not all combinations of frequencies are equally probable. The degenerate FWM process of two adjacent modes is displayed in Figure 4.2 which generates two additional frequency components (ω_{up} and ω_{down}). The cold-cavity frequencies are pulled towards an equidistant grid due to the cascading FWM effect and the energy conservation. It should be noted that the effect of cavity pulling works only if the mode remains within its locking range as described in [24, Ch. 5]. The process of FWM explains the formation of a frequency comb in fast gain media; however, does not explain the required phase locking process.

This was brought to light in [31], where the group-velocity dispersion and the Kerr-nonlinearity are considered as the main reasons. It was shown that both effects have a similar analytical impact. A minimum GVD or Kerr-nonlinearity is required in order for the intermodal phases to span the whole unit circle. A further increase of one of the parameters will narrow the emitted laser spectrum.
To round off this section, the most important mechanisms forming an FM-comb in QCLs should be highlighted. First of all, the effect of spatial hole burning is essential to trigger multi-mode operation in fast gain media. This creates an initial grid in the frequency domain, required for the formation of an OFC. Second, the effect of gain saturation suppresses the formation of pulses. Third, a finite GVD or Kerr-nonlinearity splashes the intermodal phases around the unit circle [31].

4.2 Reduced model

In this section, the master equation, presented in [31], will be simplified to obtain a comprehensive model explaining the impact of different parameters on the locking state of the FM-comb. The locking process is dominated by GVD and the Kerr-nonlinearity is set to zero in this chapter. To simplify the model, the governing equation is split into two coupled equations for the power P and phase Φ by utilizing the relation $E = \sqrt{P} \cdot \exp(j\Phi)$ in the first step. The cross-section area A was normalized to one for this step. Since this approach does not simplify the model, terms with minor contributions are being neglected in the second step as shown in [31]. This leads to

$$\left(\frac{n}{c_0}\partial_t \pm \partial_z\right) P_\pm = g(P)P_\pm - \underbrace{g(P)\frac{T_2}{2}\partial_t P_\pm}_{(1)} - \underbrace{g(P)T_2^2 P_\pm(\partial_t\phi_\pm)^2}_{(2)} - \alpha P_\pm \tag{4.2}$$

$$\left(\frac{n}{c_0}\partial_t \pm \partial_z\right) \phi_\pm = \underbrace{-\frac{g(P)}{2}T_2\partial_t\phi_\pm}_{POD} - \underbrace{\frac{g(P)}{2}\frac{T_g^2}{T_1}\frac{P_\pm}{P_{sat}}\partial_t\phi_\mp}_{SHB} - \underbrace{\frac{D_\omega}{2}(\partial_t\phi_\pm)^2}_{GVD}. \tag{4.3}$$

where $P_\pm$ and $\phi_\pm$ are the power and the phases of the left and right propagating waves respectively, P_{sat} is the saturation power, and $g(P)$ represents the saturated gain coefficient.

Since the Kerr-nonlinearity contribution was neglected, it is possible to omit the gray-marked term (2) in the upper equation. This enables to solve the power distribution independently from the phase equation [54]. Equation 4.2 can be further simplified by neglecting the gray marked term (1). The phase equation of the reduced model includes gain saturation, SHB, and GVD; all the prerequisites for the formation of FM-combs. In addition, it also comprises a term called phase oscillation damping (POD), which would cause single-mode operation [31].

4.3 Chirp shaping mechanisms

In the previous section, the analytical description of an FM-comb was minimized to simplify the analytical formulas. Since the power equation can be solved separately and one can potentially use any power distribution for the calculation of the phases, the qualitative description of the FM-comb can be performed by using only the phase equation 4.3. By analyzing this governing equation, three spatially varying variables can be identified influencing the locking state of the FM-comb:

1. the power of the counter-propagating waves $P_{\pm}$
2. the saturation power P_{sat}
3. the group velocity dispersion D_{ω}

The first parameter ($P_{\pm}$) can be readily influenced by changing the gain spatially. This is achieved by splitting the cavity into sections, which are biased differently. An example of a two-section device can be found in [25]. Another important factor impacting $P_{\pm}$ is the *reflectivity of the facets*. By, for instance, applying a high reflectivity (HR) or low reflectivity (LR) coating to one of the facets, the spatial power distribution can be impacted. An example of such a coating applied to a QCL can be found in [55].

Second, the saturation power of the laser gain medium can be influenced by spatially changing the width of the device. This can be readily implemented by applying a taper to the waveguide. Some examples of the application of tapers are the reduction of lateral divergence of the laser beam [56] or the efficient waveguide to fiber coupling [57]. Recently, tapered structures were also used in OFCs to enhance the effect of gain saturation dynamics and nonentities which led to a flatter intensity spectrum and a clearer linear chirp [58].

Finally, the group velocity dispersion can be spatially varied by changing the material composition along the laser length leading to a different spectral shape of the refractive index n. This approach is similar to heterogeneous QCLs, where some cascades emit at a slightly different frequency to increase the total emission bandwidth [5, Ch. 18.4], [20]. Since the first three approaches, namely the laser bias, the reflectivity of the facets, and the cavity design are far easier to implement and present already three versatile tools to impact the locking state, the impact of a spatially varying GVD was not considered in

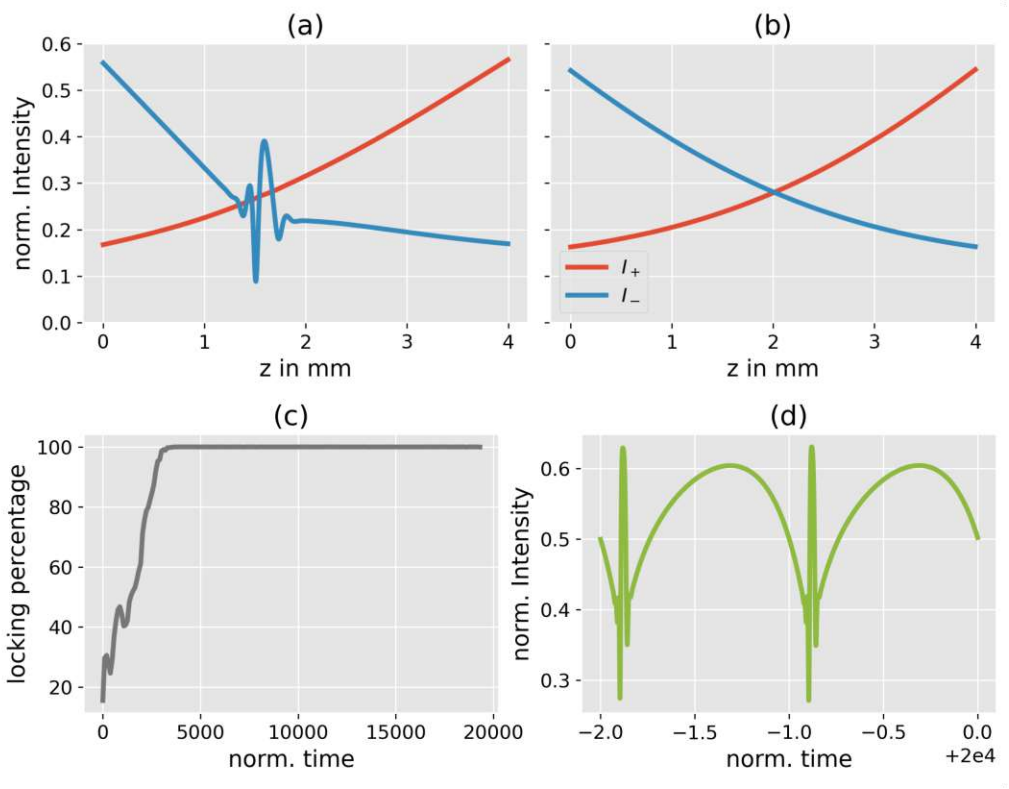

Figure 4.3: *Important information about the simulation of FM-combs: The SHB impacts drastically the spatial intensity profiles as depicted in (a). By averaging the intensity profiles over the past 15000 roundtrips, this effect can be mitigated leading to smooth exponentially growing intensity profiles as shown in (b). Figure (c) depicts the locking percentage of the comb over the simulation time and (d) displays the temporal output intensity of the comb.*

this work. The GVD was set to a constant value (GVD = -2500 fs^2/mm) where the laser emits an FM-type OFC. As shown in [31], the absolute value of the GVD has to exceed $|GVD| > 1000\ fs^2/mm$ at zero Kerr-nonlinearity to obtain a locked FM-comb state for the considered parameters.

Before the impact and their implementation of the laser bias, the reflectivity of the facets, and the cavity design are discussed, it should be mentioned that the intensity profile is distorted by the SHB. This effect is displayed in Figure 4.3 a. In order to identify the effects of the three approaches discussed more clearly, the intensity profiles are being averaged over the last 15000 round trips of the simulation as shown in Figure 4.3 b. This averaging process was conducted for all shown intensity profiles in the following sections. The simulation time was set to 20 000 round trips. In addition, Figure 4.3 shows the locking behavior of the FM-comb. The laser starts to produce a periodic output at about 4000 roundtrips after the simulation was started. Similar to the work of Beiser et al. [32], the locking percentage was calculated by the autocorrelation of the intensity profile of two different round trips separated in time. Figure 4.3 d shows the nearly constant

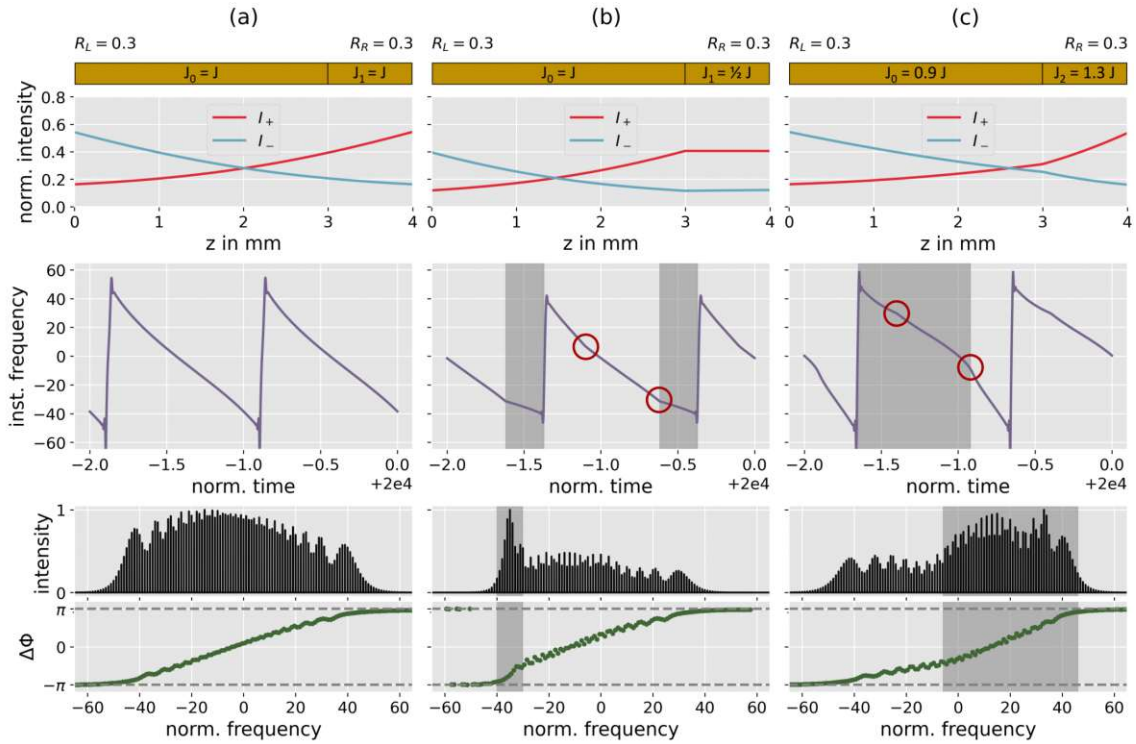

Figure 4.4: *Two-section device showing the influence of a different laser bias of the sections on the FM-comb: a) constant bias on both sections, b) reduced bias on the smaller section, and c) increased bias on the smaller section. Each case shows the impact of the laser bias on the spatial intensity, instantaneous frequency, spectral intensity profile, and intermodal phases $\Delta\Phi$. The kinks caused by the abrupt change of the bias are marked in red.*

and periodic intensity profile which is characteristic for this type of OFC as discussed previously.

The following subsections describe the impact of the laser bias, the reflectivity of the facets, and the design of the cavity on the intensity distribution and, subsequently, on the locking state of the comb. In addition, their implementation into the numerical model is being discussed. The used simulation parameters can be found in chapter A.

4.3.1 Laser bias

The most powerful approach to influence the intensity profile, which is described in this work, is the laser bias. This effect can be readily implemented into the model by changing the current $J = J_{injected} - J_{transparency}$ along the waveguide. To explore its influence, the waveguide with the length L was divided into a longer $(3/4L)$ and a shorter $(1/4L)$ section as shown in Figure 4.4. The bias of the sections where changed to spatially influence the gain. Figure 4.4 b and c show the influence of a smaller and larger current on the small section. Both variations of the laser gain show a direct influence on the spatial intensity. If the current density is higher, the intensity profiles grow stronger and vice versa. This is in accordance with the reduced model given in (4.2). In comparison to Fig. 4.4 a, 4.4 b

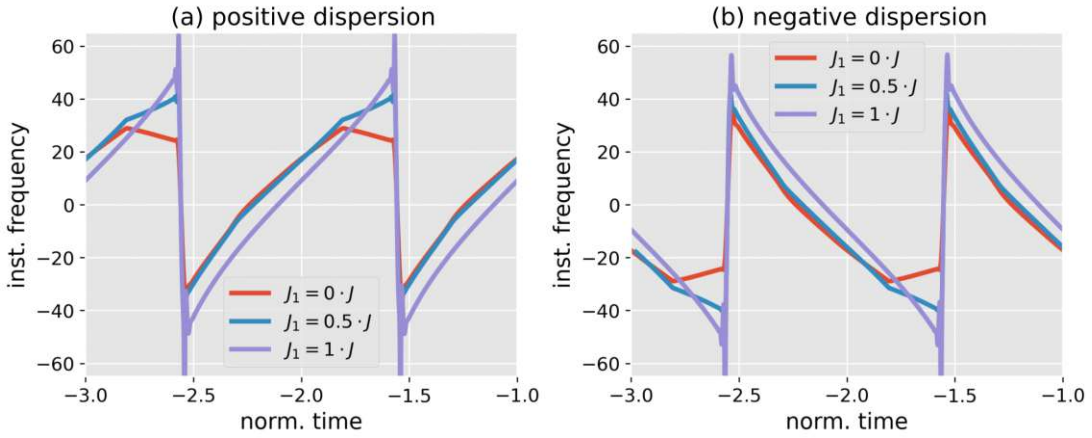

Figure 4.5: *Influence of a lower bias at the short section of a two section device, as displayed in Figure 4.4(b), on the instantaneous frequency for a GVD of (a) 2500* $\frac{fs^2}{mm}$*, and b) -2500* $\frac{fs^2}{mm}$*.*

and 4.4 c exhibit two kinks in the instantaneous frequency (marked in red). These kinks take place at approximately one-quarter and three-quarters of the round trip time and are a direct consequence of the changed bias of the smaller section. The change in the shape of the instantaneous frequency impacts also the intensity spectrum. As marked in gray, the intensity spectrum gets more pronounced at spectral regions, where the instantaneous frequency is flatter. This influence can also be observed in the intermodal phases.

Figure 4.5 displays the influence of a lower bias on the smaller section (Fig. 4.2 b) on the instantaneous frequency with positive and negative sign of the GVD. The normalized time axis for each graph was shifted such that the jumps in the instantaneous frequency overlap. One can clearly identify the two kinks and the influence of the bias of the smaller section on the steepness of the instantaneous frequency on approximately three-quarters of the round trip time (normalized time). The influence on the opposite side, next to the other kink, is far less pronounced. Regardless of whether the small section is located at the right or left end of the resonator, the influence is equal due to the symmetry of the laser. Figure 4.5 shows also that the sign of the dispersion coefficient changes the slope of the instantaneous frequency. By further increasing the dispersion coefficient, the bandwidth gets smaller [31]. Hence, the steepness of the instantaneous frequency would decrease.

4.3.2 Cavity design

The cavity design represents the second approach to tailor the locking state of the FM-comb. Here, the cross-section area of the waveguide and its spatial shape is taken into consideration to shape the instantaneous frequency. This section briefly describes three different implementation versions. The first method was already presented in the introduction of this section by means of the reduced model (equation 4.2 and 4.3). In case of a lossless waveguide, a tapered structure does not impact the power of the traveling waves. The taper only increases the cross-section area A. In other words, the power P is conserved

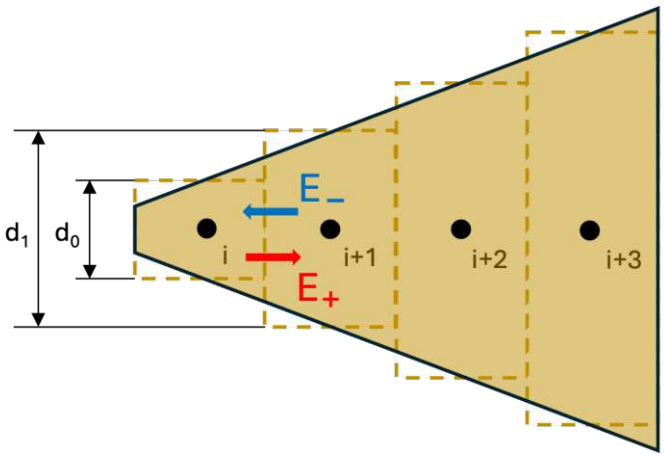

Figure 4.6: *Schematic drawing of a tapered waveguide structure on a discretized grid. The black points are the discretized spatial grid points and the parameter d represents the width of the tapered structure.*

during the propagation. Changing the cross-section does, however, impact the intensity $I = P/A$ profiles. By increasing the cross-section area A, the intensity I decreases, which leads to a less saturated laser gain medium. This means $P_{sat} = I_{sat} \cdot A$ increases leading to an elevated gain factor $g(P)$. That means, the taper can be implemented by rewriting the the master equation for the power and the phase. Its influence can be explored by altering the parameter P_{sat} spatially.

An alternative to this complex rewriting process can be found by considering the impact of the cavity design on E_+ and E_-. This can be readily implemented into the discrete version of the PDE. First, the values of E_+ and E_- of the next point (on the u and v-axis) are calculated by the numerical implementation. Second, the magnitude of the electric field is altered by the taper. This process is displayed in Figure 4.6. By considering the transition from i to $i+1$ for E_+ and vice versa for E_-, following relations can be calculated

$$E^{i+1}_{+,tapered} = \sqrt{\frac{d_0}{d_1}} \cdot E^{i+1}_{+} \qquad\qquad E^{i}_{-,tapered} = \sqrt{\frac{d_1}{d_0}} \cdot E^{i+1}_{-}. \tag{4.4}$$

As indicated in Figure 4.6, the taper does not alter the calculation of the out-coupled or the back-reflected part of the light at the facets.

In a similar way, one could rewrite the master equation for its intensity by simply substituting $I_\pm = P_\pm/A$. In case of the power equation of the reduced model (4.2), this leads to

$$\frac{n}{c_0}\partial_t I_\pm \pm \partial_z I_\pm + \frac{I_\pm}{A}\partial_z A = (g(I) - \alpha)\, I_\pm. \tag{4.5}$$

The additional term, marked in gray, implements the influence of the cavity design.
For the numerical simulation, equation 4.4 was used to implement the cavity design into

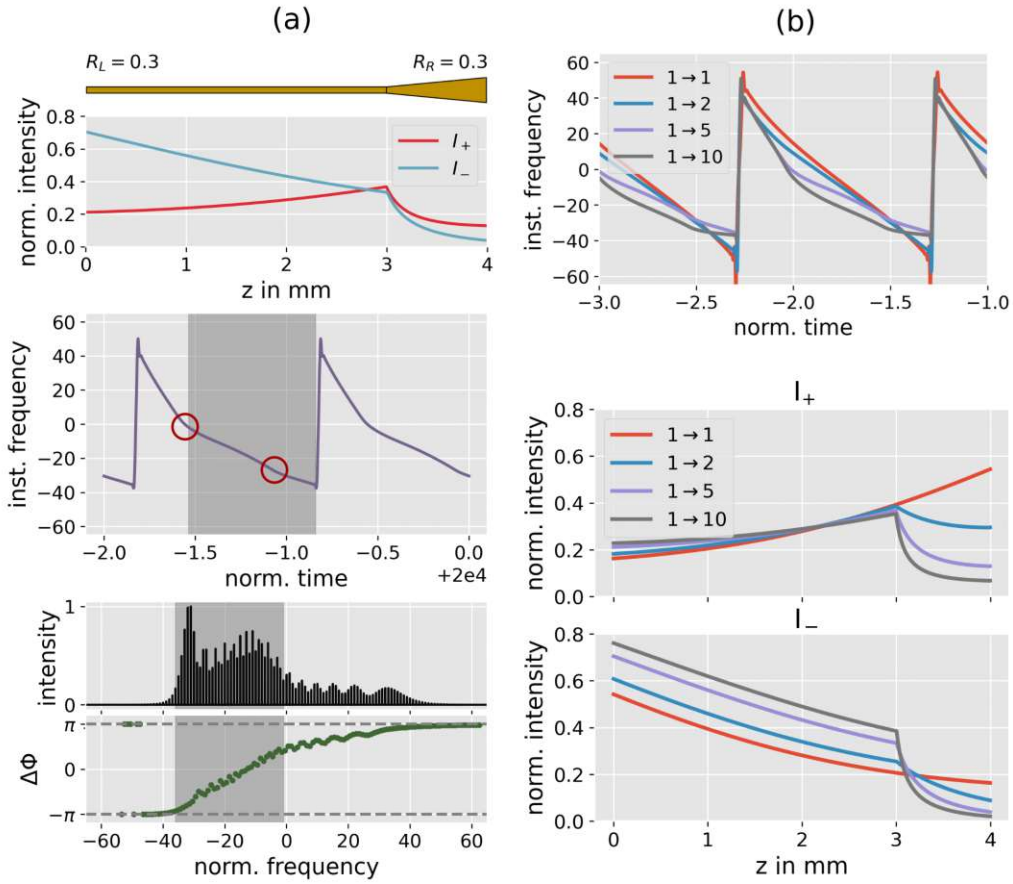

Figure 4.7: *Impact of a $1/4 \cdot L$ long linear tapered structure by a) extending the cross section area to its fivefold at the right facet. b) shows the effect of different taper sizes on the same structure by increasing the cross-sectional area to twice, five times, and ten times the original dimensions on the right facet.*

the master equation. In case of the reduced model, P_{sat} was modified for that purpose. As depicted in Figure 4.7 the applied linear taper causes two kinks (marked in red) in the instantaneous frequency chirp and pronounces a certain region (marked in gray) in the intensity spectrum. To investigate the influence of the taper in more detail, the impact of various taper sizes is displayed in Figure 4.7 b. By comparing the instantaneous frequency profiles shown, it becomes apparent that the spectral range in which the slope of the instantaneous frequency changes significantly is enlarged by increasing in the taper size.

A possible reason for this behavior can be found in the gradual spatial impact of the taper. In general, the taper and the laser bias are different in their influence on E_+ and E_-. The laser gain influences both propagating fields equally by changing the rate of increase in the propagation direction. The taper increases this rate for one direction and decreases the rate of the other one. Both effects impact, as shown, the locking state of the comb.

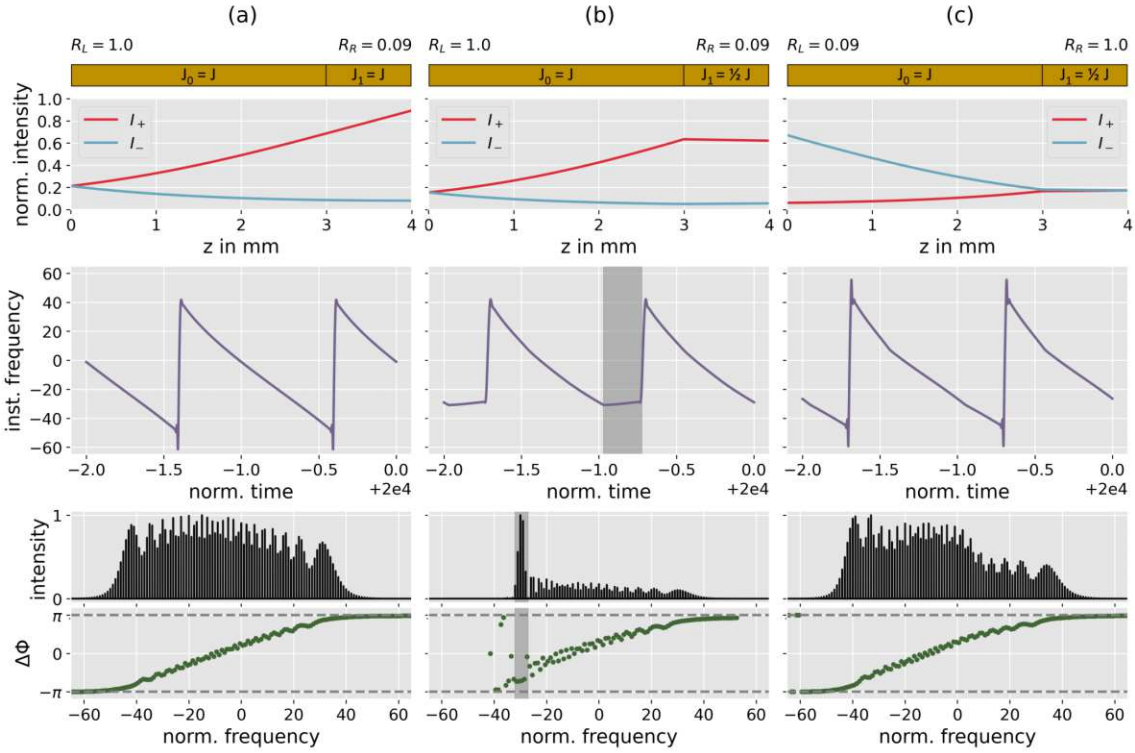

Figure 4.8: *Influence of the reflectivity of the facet on the locking state of the comb: (a) without modulation section and with reduced bias (b) on the low reflectivity side, and (c) on the high reflectivity side.*

In addition, by comparing the size of the taper used in Figure 4.7 a and the factor of the current reduction in Figure 4.4 b, one would assume that the laser bias has a bigger influence on the locking state of the comb. The taper features a lower impact due to its gradually increasing shape and not due to its general influence. In the reduced model (equation 4.2 f), the taper impacts P_{sat} which is contained in $g(P)$ and as a separate term in the spatial hole burning term, whereas the laser bias solely influences $g(P)$. It is worth noting that it was not possible to increase the spatial intensity at the tapered smaller section over a certain amount without losing the locked state of the comb. A similar behavior was observed in case of the laser bias, where the bias of the smaller section was increased.

4.3.3 Facet reflectivity

The reflectivity of the facets influences the intra-cavity intensity profiles and thus the locking state of the comb as shown in Figure 4.8. The reflectivity can be experimentally changed by applying a high-reflective (HR) or an anti-reflection (AR) to the facets of the laser. Fig. 4.8 a shows a laser cavity with an AR-coating on the left facet and an HR-coating on the right facet. However, the characteristics of the comb shown in the Figure have not changed significantly compared to the original FM-comb shown in Figure 4.4 a.

A similar picture, apart from the intensity profile, can be generated by swapping the sides of the coatings.

The impact of the reflectivity of the facet is particularly interesting in combination with the modification of the laser bias along the cavity. By reducing the current density on the smaller section, the above described symmetry is removed as shown in Figure 4.8 b, c. This results in a different locking state of the comb when the coatings of both facets are swapped. By comparing Figure 4.4 b with 4.8 b and c, it becomes apparent that the reflectivity changes the extent of influence of the lower biased section. By applying the AR-coating on the facet of the lower biased section (Figure 4.8 b), its influence increases. This process is reverted by swapping the coatings (Figure 4.8 c).

Before discussing the possible application of chirp engineering, the influence of the reflectivity on the bandwidth should be discussed. This relation was already brought to light in [32]. In that work, three possible parameters were discussed to increase the bandwidth of the FM-comb: Kerr-nonlinearity, GVD, facet reflectivities, and RF-injection. By comparing Figure 4.8 a with 4.4 a, one can clearly see that the reflectivity changes have slightly shifted the spectrum towards lower frequencies. The width of the spectrum has changed marginally. This negligible influence can be explained by the fact that the product $R_L \cdot R_R = 0.09$ has not been changed.

4.4 Possible applications

The combination of the laser bias, the cavity design, and the reflectivity of the facets provide a useful set of tools to tune the locking state of the FM-comb in a wide range. A possible application is the generation of short pulses. As discussed previously, the generation of pulses with QCLs is a difficult task due to the fast gain properties. As outlined in [24, Ch. 5], a QCL can be used to generate pulses by either applying a strong RF-signal on a modulation section or by utilizing an FM-comb in combination with a chirp compressor. An implementation of such a compressor applied on a QCL can be found in [26]. By analyzing the simulation result depicted in Figure 4.4 a, it becomes clear that the shape of the instantaneous frequency is slightly nonlinear. In order to generate transform-limited pulses by a linear chirp compressor, higher-order chirping terms have to be eliminated. In case of the reduced model (equation 4.2 f), this slight nonlinearity can be readily compensated by imposing linear intensity profiles as shown in Figure 4.9 a. This is only possible for the reduced model since the power equation is decoupled from the phase equation. In addition, Figure 4.9 a depicts that the linear intensity profile exhibits a nearly rectangular intensity profile. This is in accordance with the previous simulations, where spectral regions were highlighted depending on the steepness of the instantaneous frequency profile.

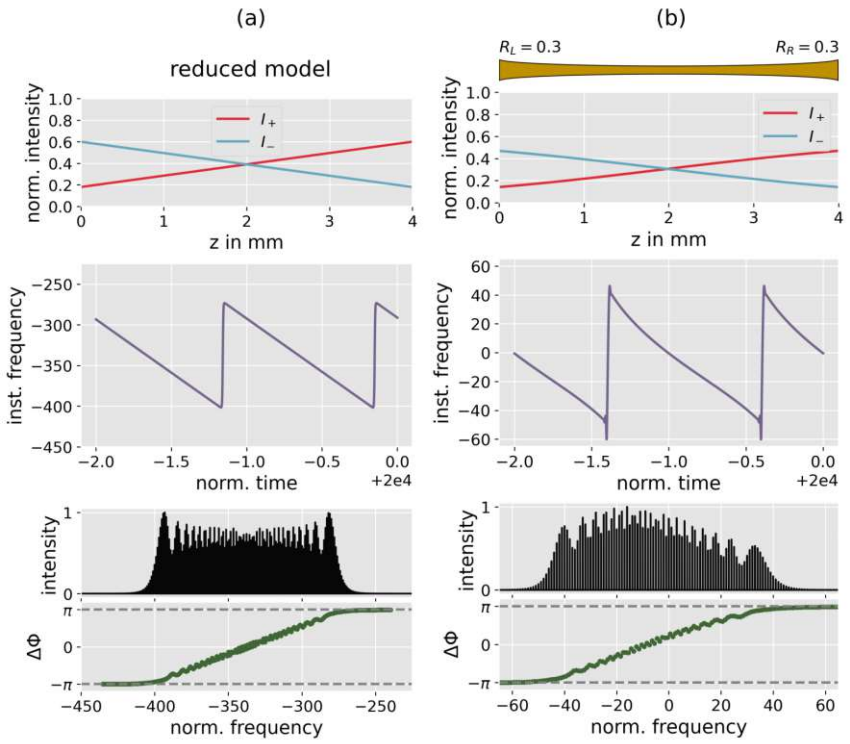

Figure 4.9: *Impact of linear intensity profiles on the characteristics of an FM-comb. (a) depicts the solution of the phase equation (equation 4.3) by imposing linear intensity profiles. (b) shows the solution of the master equation by linearizing the intensity profiles using a cosine hyperbolic cavity design.*

The intensity profile, simulated with the master equation, can be linearized by changing the cavity design. Both intensities (I_+ and I_-) rise nearly exponentially[2] as depicted in 4.4 a. This means that the total intensity is given by

$$I = I_0 \cdot \left[e^{gz} + e^{-gz}\right] = I_0 \cdot 2cosh(gz). \tag{4.6}$$

The coefficient $g \approx 3\ cm^{-1}$ was determined by fitting I_+ by with an exponential function. In order to linearize the intensity profiles, a cosine hyperbolic taper, centered at $L/2$ with a unity value on the facets, was applied to the structure. As shown in Figure 4.9 b, the cavity design clearly linearizes the intensity profiles but does not eliminate all higher-order chirp components. A possible reason for this mismatch is given by the spectral gain shape of the medium, which is neglected in case of the reduced model. By comparing the results depicted in Figure 4.9, one can clearly see that the spectral intensity profile is shaped differently. This leads to the conclusion that the nonlinear shape of the intensity profiles and the spectral gain shape are accounted as the main contributors to higher-order chirp.

[2] The exponential profile can be derived by solving equation 4.2.

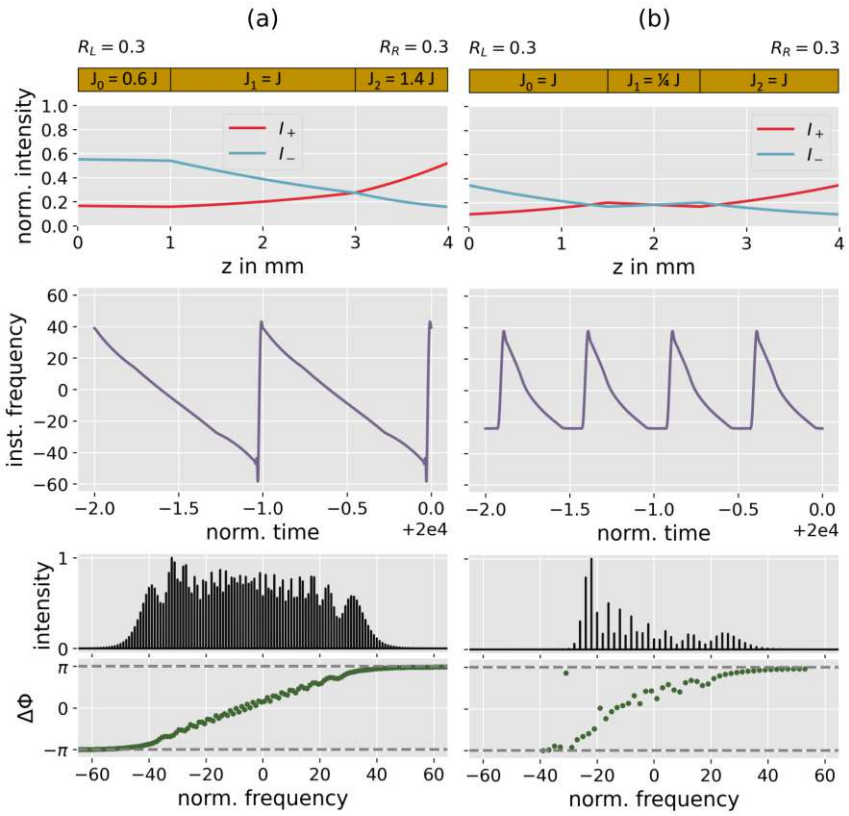

Figure 4.10: *Applications of chirp engineering: (a) compensating the nonlinear shape of the instantaneous frequency for the generation of transform-limited pulses by a linear chirp compensation, (b) the generation of harmonic combs.*

The spectral gain shape is inherently coupled to the underlying physics as presented previously. In order to linearize the chirp, another approach apart from linearizing the intensity profiles has to be considered. By neglecting the nonlinear type of the master equation, the chirp may potentially be compensated with the linear combination of the simulations shown in Figure 4.4 b and c. By comparing both simulations, one can see that the instantaneous frequency is shaped in opposite directions when changing from a higher to a lower biased section. The higher-order chirp can potentially be eliminated by a higher-biased section on one side and a lower-biased section on the other side. As shown in Figure 4.10 a, the described principle clearly straightens the instantaneous frequency profile. However, similar to the kinks in the previous simulations, the overall shape includes some ripples due to the rapid spatial change in laser bias. In a similar way, one could also adopt the instantaneous frequency profile to match a non-perfect linear chirp compressor.

Another application that results from a spatial variance of the laser bias is the generation of harmonic combs. The equidistant lines in the frequency spectrum of OFC are separated by the free spectral range (FSR) of the Fabry-Pérot resonator. In case of harmonic combs, the mode spacing is increased by an integer factor of the FSR [59–61]. Every mode of a

Fabry-Pérot resonator is associated with a standing wave intensity pattern, as discussed previously. Since every uneven mode features an intensity peak in the center of the resonator, the gain of these modes can be decreased by lowering the bias in this area. If this bias is decreased sufficiently, uneven modes will not start to lase, and a harmonic comb is formed. This effect is similar to micro-electromechanical systems used to measure point masses. At the nodal points of the standing wave of the mode, the added mass has a negligible impact on the vibration, whereas in between the nodal points the mass distorts the movement of the resonator [62, Ch. 3.1.1]. Figure 4.10 b shows a Fabry-Pérot laser with reduced bias in the center triggering the formation of a harmonic OFC. Potentially, also higher-order harmonic combs can be generated with this technique by altering the position of the reduced biased section or by a device subdivided into more sections.

CONCLUSION

Quantum cascade lasers (QCLs) are semiconductor lasers emitting light in the infrared and the terahertz range. Since their emission frequency also encompasses the molecular fingerprint region of many molecules, it is of main interest to utilize these lasers for spectroscopic applications. For such applications, it is of great interest to extend the spectral bandwidth of these lasers. This can be accomplished by two main techniques. First, the emission bandwidth can be enriched by changing the layers of the QCL leading to different emission frequencies of the cascades. Second, the bandwidth can be increased by utilizing nonlinear effects.

Since the analytical description of these lasers is of high complexity, modeling has become an indispensable part of understanding these devices and their parameters in more detail. An in-house numerical model for QCLs was analyzed, significantly expanded, and refined to simulate this broadband type of laser, namely the heterogeneous QCL. To test the spectral accuracy of different implementation schemes, a tunable laser source, and a waveguiding structure were utilized. The governing wave-equation was step by step expanded to include losses, group velocity dispersion (GVD) effects, and the gain of the laser medium. First, the losses were implemented analytically by means of the exponential integrator instead of its first-order approximation.
Second, the GVD implementation was analyzed and an implementation was developed that overcomes its inherent stability issue by utilizing the Taylor-expansion of its Laplace-transformed version and the connection to the time domain. This stabilizing technique goes well along with the parallel computation process, which significantly reduces the overall simulation time.

The developed method can be additionally used for a stable implementation of higher-order GVD terms, such as third and fourth-order, and can be utilized for their stable joint usage. The reason for the required stabilized implementation of the GVD lies in the gain implementation. In the previous model, the gain implementation was simplified by utilizing the polarization elimination. This simplification imposes losses above and below the center frequency. In case of a conventional QCL, this simplification does not impact the simulation result and is even beneficial since the induced losses compensate for the gain induced by the unstable implementation of the GVD. In case of broadband heterogeneous QCLs, this simplification cannot be applied since the medium has to be transparent at these spectral regions. This transparency was achieved by changing the implementation of the polarization equation which is coupled to the governing wave-equation. To reflect the physical behavior of a QCL in the model, the gain implementation has to include a zero at its Z-transformed version at minus one. This zero point at the maximum frequency ensures that the gain implementation is transparent at this spectral point. The gain implementation can be readily expanded to simulate a heterogeneous QCL. This was achieved by a multiple implementation of the polarization equation shifted in frequency. The developed model can be readily expanded from the simulation of a waveguide, including gain, group velocity dispersion effects, and losses, to the simulation of a laser.

The bandwidth of a QCL can, in addition to the heterogeneous concept, be enlarged by the utilization of nonlinear effects by means of pulses. However, it is well known that the fast gain medium of a QCL hardens the generation of pulses. A powerful method to overcome this limitation is a combined usage of a QCL emitting an FM-type OFC and a chirp compressor. To enable the generation of transform-limited pulses, both components need to match. That means the chirp induced by the QCL has to be fully reverted by the compressor. In order to enable such an alignment of the components, techniques were developed to tailor the chirp of an OFC generated with a QCL. Based on a reduced model of the master equation for fast gain media, three parameters were identified, and their influence was simulated. First, by changing the laser bias spatially at a device that is subdivided into multiple sections, the instantaneous frequency exhibits kinks, altering its overall shape. Second, a similar effect can be achieved by changing the cavity design. Third, by applying an HR or LR coating to the facets, the extent of the influence of the first two methods can be impacted. With a combined usage of these techniques, the instantaneous frequency can be tailored nearly freely and enables the generation of short pulses by means of a chirp compressor. In addition, the developed model can be used to investigate the occurrence of harmonic combs, which can be triggered by reducing the bias of certain areas of the laser.

The numerical model developed in this work lies the foundation of broadband spectrometers based on QCLs. By conducting further research with the heterogeneous model derived and experiments with QCLs, potentially broadband optical frequency combs may be generated. If this is achieved, both developed broadening techniques can be combined, leading to even more broadband sources, which are essential parts for the detection of multiple hazardous elements. This broadband source, in combination with the integration properties of QCLs, enables pocket-size sensors. They can be potentially integrated into various applications relevant to industry and medicine, impacting the world of tomorrow.

LIST OF FIGURES

LIST OF ABBREVIATIONS

QCL	quantum cascade laser
PDE	partial differential equation
LEF	linewidth enhancement factor
SVEA	slowly varying envelope approximation
GVD	group velocity dispersion
TOD	third order dispersion
FOD	fourth-order dispersion
OFC	optical frequency comb
FWM	four-wave mixing
FSR	free spectral range
norm.	normalized
FM-type	frequency modulated type
AM-type	amplitude modulated type
HR	high-reflective
AR	anti-reflective
RF	radio-frequency

LIST OF SYMBOLS

$\tau_{2,1}$	transition time of stage two to stage one
τ_1	lifetime of stage one
$E(z,t)$	electric field depending on space z and time t
$I(z,t)$	intensity of the field
E_+	to the right propagating envelope of the electric field
E_-	to the left propagating envelope of the electric field
c_0	speed of light in vacuum
c	propagation velocity
n	refractive index
N	group refractive index
Δz	space discretization step size
Δt	time discretization step size
Δu	u-direction discretization step size ($\Delta u = \Delta z = \Delta t \cdot c_0/n$)
k	wave number
k_0	wave number at the center frequency
f	frequency
f_0	center frequency
f_s	sampling frequency
f_d	deviation from the center of the gain peak to f_0
Δf	frequency f minus the center frequency f_0
ω	angular frequency ($2\pi f$)
$\gamma(\Delta f)$	gain coefficient
Γ	confinement factor
μ	dipole matrix element
L	length of the cavity
ϵ_0	permittivity of vacuum

σ_+	right propagating envelope of the off-diagonal element of the density matrix (polarization)
σ_+	left propagating envelope of the off-diagonal element of the density matrix (polarization)
n_0	static upper level population
n_2	spatially varying upper level population
T_1	Lifetime of n_0
T_g	Lifetime of n_2
T_2	dephasing time
L_p	period length
ω_i	cold cavity resonance frequencies

BIBLIOGRAPHY

[1] R. N. Hall, G. E. Fenner, J. D. Kingsley, T. J. Soltys, and R. O. Carlson, "Coherent Light Emission From GaAs Junctions," *Physical Review Letters*, vol. 9, no. 9, pp. 366–368, Nov. 1962. [Online]. Available: https://link.aps.org/doi/10.1103/PhysRevLett.9.366

[2] J.-C. Bouley and G. Destefanis, "Multi-quantum well lasers for telecommunications," *IEEE Communications Magazine*, vol. 32, no. 7, pp. 54–60, Jul. 1994. [Online]. Available: http://ieeexplore.ieee.org/document/295945/

[3] F. Bachmann, "Industrial applications of high power diode lasers in materials processing," *Applied Surface Science*, vol. 208-209, pp. 125–136, Mar. 2003. [Online]. Available: https://linkinghub.elsevier.com/retrieve/pii/S0169433202013491

[4] H. Nasim and Y. Jamil, "Diode lasers: From laboratory to industry," *Optics & Laser Technology*, vol. 56, pp. 211–222, Mar. 2014. [Online]. Available: https://linkinghub.elsevier.com/retrieve/pii/S0030399213003010

[5] B. E. A. Saleh and M. C. Teich, *Fundamentals of photonics*, third edition ed., ser. Wiley series in pure and applied optics. Hoboken, NJ: Wiley, 2019.

[6] Z. I. Alferov, "Nobel Lecture: The double heterostructure concept and its applications in physics, electronics, and technology," *Reviews of Modern Physics*, vol. 73, no. 3, pp. 767–782, Oct. 2001. [Online]. Available: https://link.aps.org/doi/10.1103/RevModPhys.73.767

[7] H. Kroemer, "Nobel Lecture: Quasielectric fields and band offsets: teaching electrons new tricks," *Reviews of Modern Physics*, vol. 73, no. 3, pp. 783–793, Oct. 2001. [Online]. Available: https://link.aps.org/doi/10.1103/RevModPhys.73.783

[8] S. P. Khanna, S. Chakraborty, M. Lachab, N. M. Hinchcliffe, E. H. Linfield,

and A. G. Davies, "The growth and measurement of terahertz quantum cascade lasers," *Physica E: Low-dimensional Systems and Nanostructures*, vol. 40, no. 6, pp. 1859–1861, Apr. 2008. [Online]. Available: https://linkinghub.elsevier.com/retrieve/pii/S1386947707003372

[9] M. Troccoli, L. Diehl, D. P. Bour, S. W. Corzine, N. Yu, C. Y. Wang, M. A. Belkin, G. Hofler, R. Lewicki, G. Wysocki, F. K. Tittel, and F. Capasso, "High-Performance Quantum Cascade Lasers Grown by Metal-Organic Vapor Phase Epitaxy and Their Applications to Trace Gas Sensing," *Journal of Lightwave Technology*, vol. 26, no. 21, pp. 3534–3555, Nov. 2008. [Online]. Available: http://ieeexplore.ieee.org/document/4758642/

[10] J. Faist, F. Capasso, D. L. Sivco, C. Sirtori, A. L. Hutchinson, and A. Y. Cho, "Quantum Cascade Laser," *Science*, vol. 264, no. 5158, pp. 553–556, 1994, publisher: American Association for the Advancement of Science. [Online]. Available: https://www.jstor.org/stable/2883703

[11] R. Kazarinov and R. Suris, "Possible amplification of electromagnetic waves in a semiconductor with a superlattice," *Soviet Physycs. Semiconductors*, vol. 5, pp. 707–709, Oct. 1971.

[12] M. S. Vitiello, G. Scalari, B. Williams, and P. De Natale, "Quantum cascade lasers: 20 years of challenges," *Optics Express*, vol. 23, no. 4, p. 5167, Feb. 2015. [Online]. Available: https://opg.optica.org/abstract.cfm?URI=oe-23-4-5167

[13] A. Kosterev, G. Wysocki, Y. Bakhirkin, S. So, R. Lewicki, M. Fraser, F. Tittel, and R. Curl, "Application of quantum cascade lasers to trace gas analysis," *Applied Physics B*, vol. 90, no. 2, pp. 165–176, Feb. 2008. [Online]. Available: http://link.springer.com/10.1007/s00340-007-2846-9

[14] B. Hinkov, F. Pilat, L. Lux, P. L. Souza, M. David, A. Schwaighofer, D. Ristanić, B. Schwarz, H. Detz, A. M. Andrews, B. Lendl, and G. Strasser, "A mid-infrared lab-on-a-chip for dynamic reaction monitoring," *Nature Communications*, vol. 13, no. 1, p. 4753, Aug. 2022. [Online]. Available: https://www.nature.com/articles/s41467-022-32417-7

[15] P. I. Abramov, A. S. Budarin, E. V. Kuznetsov, and L. A. Skvortsov, "Quantum-Cascade Lasers in Atmospheric Optical Communication Lines: Challenges and Prospects (Review)," *Journal of Applied Spectroscopy*, vol. 87, no. 4, pp. 579–600, Sep. 2020. [Online]. Available: https://link.springer.com/10.1007/s10812-020-01041-y

[16] D. Popa and F. Udrea, "Towards Integrated Mid-Infrared Gas Sensors," *Sensors*, vol. 19, no. 9, p. 2076, May 2019. [Online]. Available: https://www.mdpi.com/1424-8220/19/9/2076

[17] I. Coddington, N. Newbury, and W. Swann, "Dual-comb spectroscopy," *Optica*, vol. 3, no. 4, p. 414, Apr. 2016. [Online]. Available: https://opg.optica.org/abstract.cfm?URI=optica-3-4-414

[18] T. W. Hänsch, "Nobel Lecture: Passion for precision," *Reviews of Modern Physics*, vol. 78, no. 4, pp. 1297–1309, Nov. 2006. [Online]. Available: https://link.aps.org/doi/10.1103/RevModPhys.78.1297

[19] J. L. Hall, "Nobel Lecture: Defining and measuring optical frequencies," *Reviews of Modern Physics*, vol. 78, no. 4, pp. 1279–1295, Nov. 2006. [Online]. Available: https://link.aps.org/doi/10.1103/RevModPhys.78.1279

[20] M. Jaidl, M. Beiser, M. Giparakis, M. A. Kainz, D. Theiner, B. Limbacher, M. C. Ertl, A. M. Andrews, G. Strasser, J. Darmo, and K. Unterrainer, "Ultrabroadband Heterogeneous THz Quantum Cascade Laser," *ACS Photonics*, vol. 10, no. 1, pp. 111–115, Jan. 2023, publisher: American Chemical Society. [Online]. Available: https://doi.org/10.1021/acsphotonics.2c01202

[21] D. Turčinková, G. Scalari, F. Castellano, M. I. Amanti, M. Beck, and J. Faist, "Ultra-broadband heterogeneous quantum cascade laser emitting from 2.2 to 3.2 THz," *Applied Physics Letters*, vol. 99, no. 19, p. 191104, Nov. 2011. [Online]. Available: https://pubs.aip.org/apl/article/99/19/191104/341304/Ultra-broadband-heterogeneous-quantum-cascade

[22] C. Gmachl, D. L. Sivco, R. Colombelli, F. Capasso, and A. Y. Cho, "Ultra-broadband semiconductor laser," *Nature*, vol. 415, no. 6874, pp. 883–887, Feb. 2002. [Online]. Available: https://doi.org/10.1038/415883a

[23] P. Munsaka, P. Baricholo, E. G. Rohwer, and G. W. Bosman, "Mid Infrared supercontinuum generation in a silicon germanium photonic waveguide," *Optics Continuum*, vol. 2, no. 1, p. 9, Jan. 2023. [Online]. Available: https://opg.optica.org/abstract.cfm?URI=optcon-2-1-9

[24] N. Opačak, "The origin of frequency combs in free-running quantum cascade lasers," Thesis, Wien, 2022, accepted: 2022-08-04T13:42:38Z Journal Abbreviation: Der Ursprung von Frequenzkämmen in Quantenkaskadenlasern. [Online]. Available: https://repositum.tuwien.at/handle/20.500.12708/55339

[25] J. Hillbrand, N. Opačak, M. Piccardo, H. Schneider, G. Strasser, F. Capasso, and B. Schwarz, "Mode-locked short pulses from an 8 µm wavelength semiconductor laser," *Nature Communications*, vol. 11, no. 1, p. 5788, Nov. 2020. [Online]. Available: https://www.nature.com/articles/s41467-020-19592-1

[26] M. Singleton, M. Beck, and J. Faist, "Pulses from a mid-infrared quantum cascade laser frequency comb using an external compressor," *Journal of the Optical Society of America B*, vol. 36, no. 6, p. 1676, Jun. 2019. [Online]. Available: https://opg.optica.org/abstract.cfm?URI=josab-36-6-1676

[27] C. Silvestri, X. Qi, T. Taimre, K. Bertling, and A. D. Rakić, "Frequency combs in quantum cascade lasers: An overview of modeling and experiments," *APL Photonics*, vol. 8, no. 2, p. 020902, Feb. 2023. [Online]. Available: https://pubs.aip.org/app/article/8/2/020902/2870761/Frequency-combs-in-quantum-cascade-lasers-An

[28] G. A. Reider, *Photonik: Eine Einführung in die Grundlagen.* Vienna: Springer Vienna, 2012. [Online]. Available: https://link.springer.com/10.1007/978-3-7091-1521-3

[29] J. Faist, *Quantum Cascade Lasers.* Oxford University Press, Mar. 2013. [Online]. Available: https://doi.org/10.1093/acprof:oso/9780198528241.001.0001

[30] B. Schwarz, "Monolithic integtation of mid-infrared photonics," Dissertation, TU Wien, 2015.

[31] N. Opačak and B. Schwarz, "Theory of Frequency-Modulated Combs in Lasers with Spatial Hole Burning, Dispersion, and Kerr Nonlinearity," *Physical Review Letters*, vol. 123, no. 24, p. 243902, Dec. 2019. [Online]. Available: https://link.aps.org/doi/10.1103/PhysRevLett.123.243902

[32] M. Beiser, N. Opačak, J. Hillbrand, G. Strasser, and B. Schwarz, "Engineering the spectral bandwidth of quantum cascade laser frequency combs," *Optics Letters*, vol. 46, no. 14, p. 3416, Jul. 2021. [Online]. Available: https://opg.optica.org/abstract.cfm?URI=ol-46-14-3416

[33] N. Opačak, B. Schneider, J. Faist, and B. Schwarz, "Impact of higher-order dispersion on frequency-modulated combs," *Optics Letters*, vol. 49, no. 4, p. 794, Feb. 2024. [Online]. Available: https://opg.optica.org/abstract.cfm?URI=ol-49-4-794

[34] N. Opačak, D. Kazakov, L. L. Columbo, M. Beiser, T. P. Letsou, F. Pilat, M. Brambilla, F. Prati, M. Piccardo, F. Capasso, and B. Schwarz, "Nozaki–Bekki solitons in semiconductor lasers," *Nature*, vol. 625, no. 7996, pp. 685–690, Jan. 2024. [Online]. Available: https://www.nature.com/articles/s41586-023-06915-7

[35] Y. Pinchover and J. Rubinstein, *AN INTRODUCTION TO PARTIAL DIFFERENTIAL EQUATIONS.* Cambridge University Press, 2005.

[36] J. W. Thomas, *Numerical Partial Differential Equations: Finite Difference Methods*, ser. Texts in Applied Mathematics, J. E. Marsden, L. Sirovich, M. Golubitsky, and W. Jäger, Eds. New York, NY: Springer New York, 1995, vol. 22. [Online]. Available: http://link.springer.com/10.1007/978-1-4899-7278-1

[37] T. Bodnár, P. Fraunié, and K. Kozel, "MODIFIED EQUATION FOR A CLASS OF EXPLICIT AND IMPLICIT SCHEMES SOLVING ONE-DIMENSIONAL ADVECTION PROBLEM," *Acta Polytechnica*, vol. 61, no. SI, pp. 49–58, 2021, publisher: Czech Technical University in Prague. [Online]. Available: https://hal.science/hal-03140280

[38] R. F. Warming and B. J. Hyett, "The modified equation approach to the stability and accuracy analysis of finite-difference methods," *Journal of Computational Physics*, vol. 14, no. 2, pp. 159–179, Feb. 1974. [Online]. Available: https://www.sciencedirect.com/science/article/pii/0021999174900114

[39] R. Carpentier, A. De La Bourdonnaye, and B. Larrouturou, "On the derivation

of the modified equation for the analysis of linear numerical methods," *ESAIM: Mathematical Modelling and Numerical Analysis*, vol. 31, no. 4, pp. 459–470, 1997. [Online]. Available: http://www.esaim-m2an.org/10.1051/m2an/1997310404591

[40] J. C. Strikwerda, *Finite difference schemes and partial differential equations*, 2nd ed. Philadelphia: Society for Industrial and Applied Mathematics, 2004.

[41] C. R. Taylor, "Finite difference coefficients calculator," https://web.media.mit.edu/~crtaylor/calculator.html, 2016.

[42] H. Brandén, "Numerical boundary conditions for ODE," Uppsala University, Numerical Analysis, Tech. Rep. 2000-026, 2000, iSSN: 1404-3203 Series: Technical report / Department of Information Technology, Uppsala University.

[43] R. J. LeVeque, *Numerical methods for conservation laws*, 2nd ed., ser. Lectures in mathematics ETH Zürich. Basel ; Boston: Birkhäuser Verlag, 1992.

[44] E. Sousa, "High-order methods and numerical boundary conditions," *Computer Methods in Applied Mechanics and Engineering*, vol. 196, no. 45-48, pp. 4444–4457, Sep. 2007. [Online]. Available: https://linkinghub.elsevier.com/retrieve/pii/S0045782507002198

[45] G. Doblinger, *Zeitdiskrete Signale und Systeme*, 3rd ed., 2015.

[46] T. Frey and M. Bossert, *Signal- und Systemtheorie: mit 117 Abbildungen, 26 Tabellen, 64 Aufgaben mit Lösungen und 84 Beispielen*, 2nd ed., ser. Studium. Wiesbaden: Vieweg + Teubner, 2008.

[47] W. A. Strauss, *Partial differential equations: an introduction*, 2nd ed. Hoboken, NJ: Wiley, 2008.

[48] W. H. P. Press, A. T. Saul, T. V. William, and P. F. Brian, *Numerical recipes: the art of scientific computing*, 3rd ed. Cambridge: Cambridge University Press, 2007.

[49] N. Crouseilles, L. Einkemmer, and J. Massot, "Exponential methods for solving hyperbolic problems with application to collisionless kinetic equations," *Journal of Computational Physics*, vol. 420, p. 109688, Nov. 2020. [Online]. Available: https://linkinghub.elsevier.com/retrieve/pii/S0021999120304629

[50] M. Hamza and S. Tariq, "Split Step Fourier Method Based Pulse Propagation Model for Nonlinear Fiber Optics," in *2007 International Conference on Electrical Engineering*. Lahore, Pakistan: IEEE, Apr. 2007, pp. 1–5. [Online]. Available: http://ieeexplore.ieee.org/document/4287333/

[51] J. Hillbrand, D. Auth, M. Piccardo, N. Opačak, E. Gornik, G. Strasser, F. Capasso, S. Breuer, and B. Schwarz, "In-Phase and Anti-Phase Synchronization in a Laser Frequency Comb," *Physical Review Letters*, vol. 124, no. 2, p. 023901, Jan. 2020. [Online]. Available: https://link.aps.org/doi/10.1103/PhysRevLett.124.023901

[52] S. D. Cin, R. Strieder, F. Pilat, N. Opačak, G. Strasser, and B. Schwarz, "Frequency comb spectral engineering in semiconductor lasers by intracavity spatial intensity profile shaping," (in preparation).

[53] N. Opačak, S. D. Cin, J. Hillbrand, and B. Schwarz, "Frequency Comb Generation by Bloch Gain Induced Giant Kerr Nonlinearity," *Physical Review Letters*, vol. 127, no. 9, p. 093902, Aug. 2021. [Online]. Available: https://link.aps.org/doi/10.1103/PhysRevLett.127.093902

[54] N. Opačak and B. Schwarz, "Supplementary material: Theory of frequency modulated combs in lasers with spatial hole burning, dispersion and Kerr," *Phys. Rev. Lett.*, vol. 123, p. 243902, Dec 2019. [Online]. Available: https://link.aps.org/doi/10.1103/PhysRevLett.123.243902

[55] Y. Matsuoka, M. P. Semtsiv, S. Peters, and W. Ted Masselink, "Broadband multilayer antireflection coating for quantum cascade laser facets," *Optics Letters*, vol. 43, no. 19, p. 4723, Oct. 2018. [Online]. Available: https://opg.optica.org/abstract.cfm?URI=ol-43-19-4723

[56] D.-B. Wang, N. Zhuo, F.-M. Cheng, Z.-H. Gu, J.-C. Zhang, S.-Q. Zhai, L.-J. Wang, J.-Q. Liu, S.-M. Liu, F.-Q. Liu, and Z.-G. Wang, "High-power, low-lateral divergence InP type-I lasers around 2 µm with tapered waveguide structures," *OSA Continuum*, vol. 2, no. 5, p. 1612, May 2019. [Online]. Available: https://opg.optica.org/abstract.cfm?URI=osac-2-5-1612

[57] T.-H. Chang, X. Zhou, H. Tamura, and C.-L. Hung, "Realization of efficient 3D tapered waveguide-to-fiber couplers on a nanophotonic circuit," *Optics Express*, vol. 30, no. 18, p. 31643, Aug. 2022. [Online]. Available: https://opg.optica.org/abstract.cfm?URI=oe-30-18-31643

[58] U. Senica, A. Dikopoltsev, A. Forrer, S. Cibella, G. Torrioli, M. Beck, J. Faist, and G. Scalari, "Frequency-Modulated Combs via Field-Enhancing Tapered Waveguides," *Laser & Photonics Reviews*, vol. 17, no. 12, p. 2300472, 2023, _eprint: https://onlinelibrary.wiley.com/doi/pdf/10.1002/lpor.202300472. [Online]. Available: https://onlinelibrary.wiley.com/doi/abs/10.1002/lpor.202300472

[59] Y. Wang and A. Belyanin, "Harmonic frequency combs in quantum cascade lasers: Time-domain and frequency-domain theory," *Physical Review A*, vol. 102, no. 1, p. 013519, Jul. 2020. [Online]. Available: https://link.aps.org/doi/10.1103/PhysRevA.102.013519

[60] T. S. Mansuripur, C. Vernet, P. Chevalier, G. Aoust, B. Schwarz, F. Xie, C. Caneau, K. Lascola, C.-e. Zah, D. P. Caffey, T. Day, L. J. Missaggia, M. K. Connors, C. A. Wang, A. Belyanin, and F. Capasso, "Single-mode instability in standing-wave lasers: The quantum cascade laser as a self-pumped parametric oscillator," *Physical Review A*, vol. 94, no. 6, p. 063807, Dec. 2016. [Online]. Available: https://link.aps.org/doi/10.1103/PhysRevA.94.063807

[61] D. Kazakov, M. Piccardo, Y. Wang, P. Chevalier, T. S. Mansuripur, F. Xie, C.-e. Zah, K. Lascola, A. Belyanin, and F. Capasso, "Self-starting harmonic frequency comb generation in a quantum cascade laser," *Nature Photonics*, vol. 11, no. 12, pp. 789–792, Dec. 2017. [Online]. Available: https://www.nature.com/articles/s41566-017-0026-y

[62] S. Schmid, L. G. Villanueva, and M. L. Roukes, *Fundamentals of Nanomechanical Resonators*. Cham: Springer International Publishing, 2016. [Online]. Available: http://link.springer.com/10.1007/978-3-319-28691-4

APPENDIX A

SIMULATION PARAMETERS

Symbol	Description	Value
α	loss coefficient	$4cm^{-1}$
D_ω	group velocity dispersion coefficient	-2500 $\frac{fs^2}{mm}$
TOD	third order dispersion coefficient	0 $\frac{fs^3}{\mu m}$
FOD	fourth order dispersion coefficient	0 $\frac{fs^4}{nm}$
λ_0	central wavelength	$8\mu m$
n	refractive index	3.3
D	diffusion coefficient	$600\frac{cm^2}{s}$
μ	dipole matrix element	1.8nm x e
n_{tot}	sheet density	$6 \cdot 10^{14} cm^{-2}$
T_{lu}	upper-lower level transition lifetime	1ps
T_{gu}	upper-ground level transition lifetime	6ps
T_{gl}	lower-ground level transition lifetime	80fs
T_2	dephasing time	75fs
N_f	number of frequency points	1000
N	number of spatial points	1024
L_p	period length	58nm
Γ	confinement factor	1 (chapter 3)
Γ	confinement factor	0.6 (chapter 4)